JOHANNES GUTENBERG UNIVERSITÄT MAINZ

JG|U

# Fibrin structure and morphology under shear strain

**Diploma Thesis by Miriam Koldevitz**

*Fachbereich Chemie, Pharmazie und Geowissenschaften*

*and*

*Max Planck Institute for Polymer Research*

**Mainz, 2017**

MAX-PLANCK-GESELLSCHAFT

The present work was performed in the period from June 2016 to March 2017 under supervision by Prof. Dr. Mischa Bonn and Dr. Sapun Parekh at the Max Planck Institute for Polymer Research.

Application date: June 30th 2016

Completion date: March 30th 2017

I confirm that the presented diploma thesis is an original work, completed independently without inadmissible help.

Mainz, March 30th 2017

Miriam Koldevitz

# Table of contents

# 1. Overview

When vascular damage occurs, a blood clot is formed at the wound site in order to repair the vessel wall and thus prevent external or internal blood loss. In a blood clot, red blood cells and blood platelets are found in a fibrous matrix consisting of the protein fibrin. Fibrin hydrogels combine unique set of material characteristics being indispensable to form a blood clot. Fibrin gels become stiffer when deformed and thereby resistant to further deformation.[1-6] A fibrin network is among the most resilient biopolymers and outlasts shear and tensile strains up to 300 %.[7, 8] This strain-stiffening property of the material is necessary to form sufficiently strong blood clots that are able to resist the intravascular blood pressure and large strains, while being flexible on positions where only weak loads occur. Therefore properly formed fibrin networks are crucial in wound healing. Failure of clot formation could lead to internal or external bleeding, while failure in fibrin degradation could lead to thrombosis.[9, 10] Because of this dynamic blood clot environment, it is important to understand the mechanical properties of fibrin. Under both shear and tensile deformation, a fibrin network shows linear elastic behavior at low strains, and non-linear elastic behavior at high strains.[1-8, 11-13]

Different quantitative approaches have been used as microscopic imaging techniques in biology. One particular technique that is relevant to fibrin is confocal microscopy wherein the location of a fluorescent dye molecule (fluorophore) can be identified with high spatial resolution (~ 500 nm) in three dimensional space. The possibility of combining confocal microscopy with rheology to image the fibrin network during deformation has been a very helpful to understand the role of single fibrin fibers within the macroscopic network.

Coherent anti-Stokes Raman scattering (CARS) microscopy is one variant of vibrational microscopy, which, as a group of techniques, generally provides information on chemical features – such as molecular structure of proteins or lipids - on similar length scales as confocal microscopy. The type of information from vibrational microscopy is complementary to that from other light microscopy methods. The development of CARS techniques began in the second half of the 20th century. CARS was first observed in 1965 by Maker and Terhune at the scientific

laboratories of Ford Motor Company.[14] The research of the Xie group at Harvard University was instrumental to transform CARS from a nonlinear spectroscopy tool into a useful vibrational (label-free) microscopy tool.[15]

Recently, broadband CARS (BCARS) microscopy, which is the nonlinear analog to Raman microscopy, measurements have been used to quantify mechanically induced secondary structural changes in fibrin gels under tensile strain. It was shown that the amount of α-helical structure decreased with increasing deformation and increasing contribution from β-sheet structure. The contribution of random coil structure remained constant for all strains.
Furthermore, it was shown by structural mapping of relaxed and deformed fibrin gels that the local composition of secondary structure becomes inhomogeneous with increasing tensile load, which indicates a non-uniform force distribution.[16]

The goal of this thesis is to give a physical-chemical description of fibrin at the molecular (from spectroscopy) and microscopic (confocal microscopy) scale in response to shear strain. Since most studies on fibrin rheology discuss shear deformation and blood flow in vessels exert shear forces on fibrin clots *in vivo*, the identification of molecular changes under high shear strains and further quantification is necessary. On the molecular level, vibrational spectroscopy of fibrin gels under shear strain would allow to quantify shear-induced changes in secondary structure and give new insights about the fundamental mechanisms of elasticity of fibrin gels. Specifically, such measurements will provide critical information about when (and if) molecular unfolding truly begins to dominate the mechanical response of fibrin under shear deformation. Therefore the development of a method that makes secondary structure imaging by BCARS microscopy of fibrin gels under shear strain is well justified.

# 2. Introduction

In this chapter, I will introduce the biomaterial fibrin, that is the subject of this thesis, and describe the experimental techniques used in my examination of this material. Furthermore, the sample preparation, the used experimental techniques as well as shear cell design for BCARS measurements are described.

## 2.1. Fibrin

There are two different mechanisms to activate the process of blood coagulation, the intrinsic and extrinsic pathway. The intrinsic pathway is kicked off by registration of a negatively charged surface, like that appearing in damaged endothelium, basal membranes, or platelet lipids, through activation of factor XII molecules. Of greater importance is the extrinsic pathway, which occurs after an injury to endothelial cells and causes the release of the tissue factor thromboplastin. Both pathways result, after multiple enzymatic steps, in the formation of small amounts of the protease thrombin. Positive feedback leads to further activation of factor X which proteolytically cleavages prothrombin to form more thrombin. Finally, thrombin catalyzes the polymerization of the fibrinogen monomers to fibrin, which then forms a blood clot to seal the wound site.[17]

Fibrinogen is a symmetric protein, which consists of three distinct regions: Two sets of three polypeptide chains named Aα, Bβ, and γ (D-region), which are joined together in the N-terminal E-region in the center (figure 1). The two D regions have constitutively open a- and b-holes located in the γ- and β-modules, respectively.[18, 19]

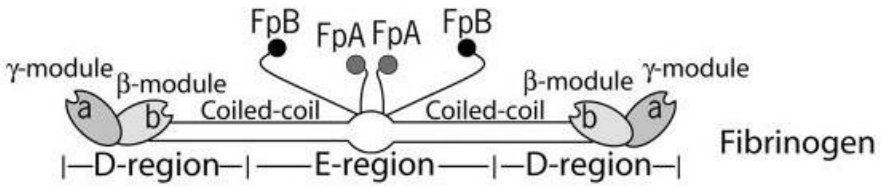


Figure 1 Schematic of Fibrinogen. Fibrinogen consists of an E-region in the center, which is connected to two D-regions with three-stranded coiled-coils made of α, β and γ- chains and constitutively open a- and b-holes located in the γ- and β-modules.[18]

Thrombin, as a serine protease, is an enzyme that cleaves peptide bonds in proteins. In Fibrinogen, it leads to the cleavage of the small fibrinopetides A and B (FpA and FpB) in the central N-terminal part of fibrinogen, the E-region. This reveals the A- and B- knobs on the E region to form an active Fibrin monomer (figure 2).

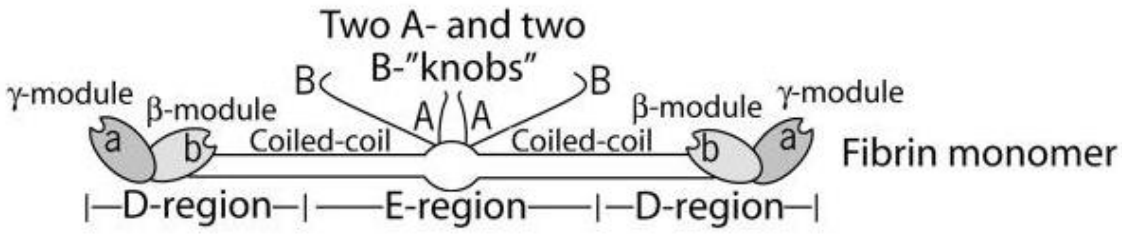


Figure 2 Schematic of the Fibrin monomer. After cleavage of the fibrinopeptides A and B (FpA and FpB) in the E-region two A- and B-knobs are revealed.[18]

The fibrin monomer then self assembles to the fibrin polymer. The A- and B- knobs on the E-region non-covalently bind to the a- and b- holes in the D region of other fibrin monomers (figure 3). The driving force of fibrin polymerization is the complementary binding of the A-knobs and a-holes and B-knobs and b-holes, and through interactions between D regions through γ-γ chain interactions, resulting in formation of a doublestranded protofibril with monomers staggered relative to one another by roughly half a protein length (45 nm).[18-20]

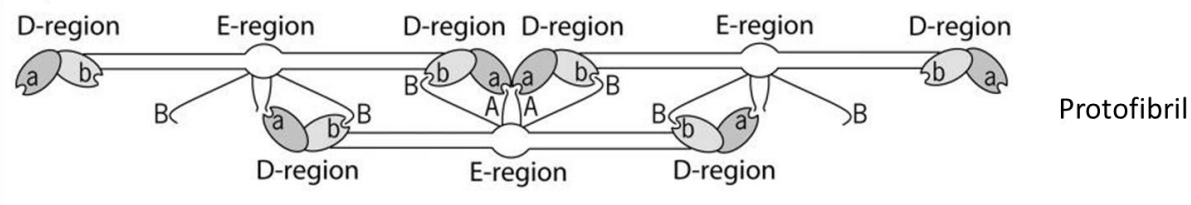


Figure 3 Schematic overview of a half-staggered 2-stand protofibril. The protofibril is formed through the binding of A- and B- knobs in the E-region with a- and b- holes in the D-region and γ-γ chain interactions between the D-regions.[18]

Due to lateral interactions between protofibrils, mediated by B:b knob-hole interactions and by αC-domains (figure 4) in the D-region, which are stabilized by the enzyme Factor XIIIa (FXIIIa), multiple protofibrils further assemble into larger fibers with a final thickness ranging from 50 to 200 nm and fiber length ranging

from 0.3 to 4.8 µm.[11, 15, 21] Figure 4 (taken from ref. 3) gives a detailed overview of the structure of fibrinogen (A) and fibrin (B).

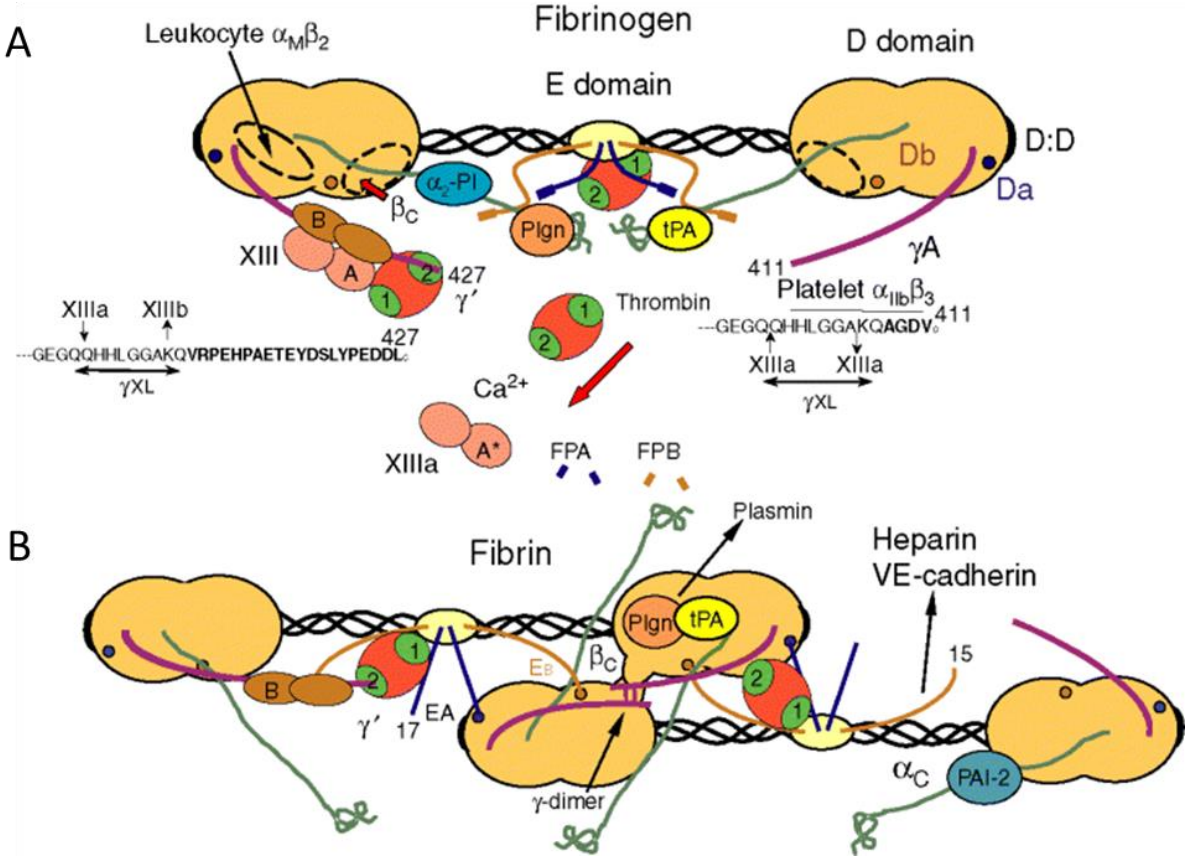


Figure 4 Detailed representation of the fibrinogen polymerization. (A) The protease thrombin cleavages the small fibrinopeptides A and B from the E domain to reveal the A- and B- knobs. The so formed fibrin monomer can now bind with the E region on D regions of another fibrin monomer resulting in protofibrils. (B) Protofibrils enable to cross-link under the influence of FXIIIa, activated by thrombin. The αC-domains (located in the D-region, green) bind with other protofibrils in order to form thicker fibers resulting in a fibrin polymer.[3]

Factor XIII is a transglutaminase that catalyzes the formation of an isopeptide bond between the free amine group of lysine and the acyl group at the end of the side chain of protein- or peptide-bound glutamine. It is found in blood plasma and converted to an activated form FXIIIa by thrombin in the presence of $Ca^{2+}$.[22, 23] FXIIIa cross-links protofibrils into larger fibers and stabilizes an early formed fibrin mesh. FXIIIa allows the formation of branches and entanglements between protofibrils until a three-dimensional network is established with a mesh size on the order of several µm. These fibers are the primary structural unit of the stable network of fibrin hydrogels. In addition, FXIIIa leads to the fixation of the thrombin activatable

fibrinolysis inhibitor (TAFI) and $\alpha_2$-antiplasmin in the blood clot. This is necessary to prevent the blood clot from premature fibrinolysis. [24, 25]

## 2.2. Mechanical properties of fibrin networks

Fibrin gels, like other biopolymer networks, differ from conventional synthetic polymers because they become stiffer when deformed and are thereby resistant to further deformation.[1-6] A fibrin network is among the most resilient biopolymers and withstands shear and tensile strains up to 300 %.[7, 8] Under both shear and tensile deformation, a fibrin network shows linear elastic behavior at low strains, and non-linear elastic behavior at high strains.[1-8, 11-13] This strain-stiffening property of the material is necessary to form sufficiently strong blood clots that are able to resist the intravascular blood pressure and large tensile strains, while being flexible on positions where only weak loads occur.

Depending on the amount of strain, fibrin shows varying mechanical properties. A scheme of these different regimes of fibrin under shear strain is given in figure 5 (reprinted from ref. 11). The elastic behavior at small stresses is caused by the bundle like structure, where fibers behave as loosely cross-linked bundles of protofibrils with a built-in stretch-stiffening response. The initial, linear network stiffness reflects thermal fluctuations of the fibers (regime 1). Strains of a few percent pull out the thermal slack from fiber segments between cross-links, leading to network stiffening (regime 2). Even larger strains cause fiber stretching (regime 3), followed by stretching of flexible regions within the fibers (regime 4). The elasticity at higher stress is dominated by changes at molecular level (regime 5). This results in strain hardening and unfolding of the molecules.[11]

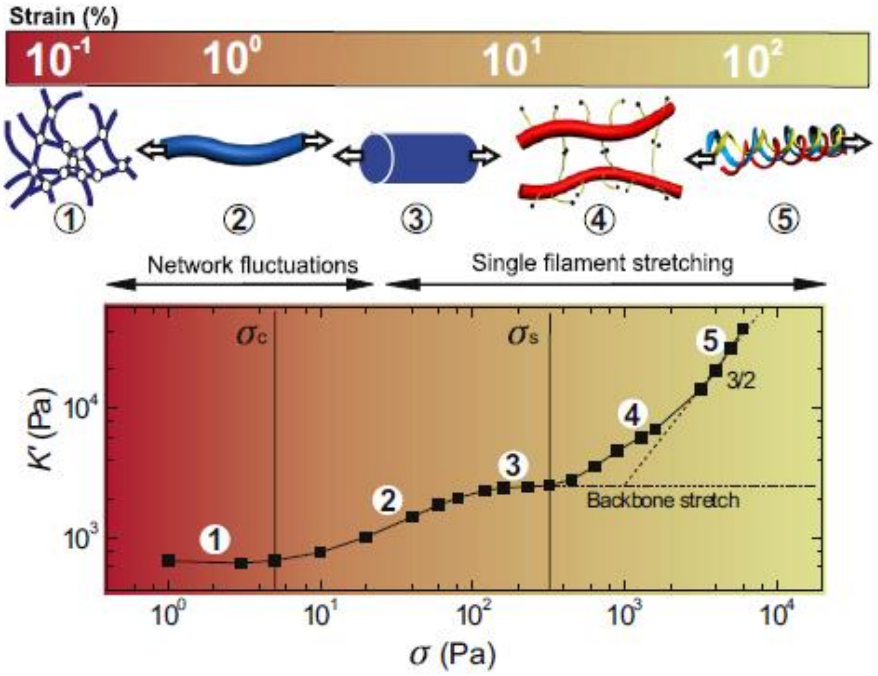


Figure 5 Scheme of different stretching mechanisms of Fibrin under shear strain. The applied stress (Bottom) causes a strain (Top) on the network. At low stress (red) the elasticity is dominated by thermal fluctuations (1). Due elongation of the fibers network stiffening occurs (2). At higher stress (green) the elasticity is presumably dominated by changes at the molecular level. A plateau regime (3) reflects the linear enthalpic stretch modulus of the fibrin fibers, which governs backbone stretching (4). Ultimately, fibrinogen monomers are forced to unfold (5) before the network ruptures.[11]

Thus, the mechanical response in the low stress domain is dominated by the entropic elasticity at the network level (thermal network fluctuations), while the elasticity in the higher stress domain is dominated by unfolding of molecules.[11, 26-28] Therefore the nonlinear elastic response of fibrin is manifested by strain hardening, and on a molecular scale this is caused by unfolding of fibrinogen in response to large deformations. A thoroughly understanding of the mechanical properties of fibrin with their large elastic extensibility can be resolved by identifying flexible linkers between fibrin molecules and protofibrils, or regions on the fibrinogen molecule that could stretch or unfold. Multiple hypothesized unfolding mechanisms of fibrin have been debated over the past few years (figure 6): (A) unfolding of the α-helical coiled coils into β strands[29]; (B) unfolding of the γ-modules[30]; and (C) unfolding of the αC region.[31]

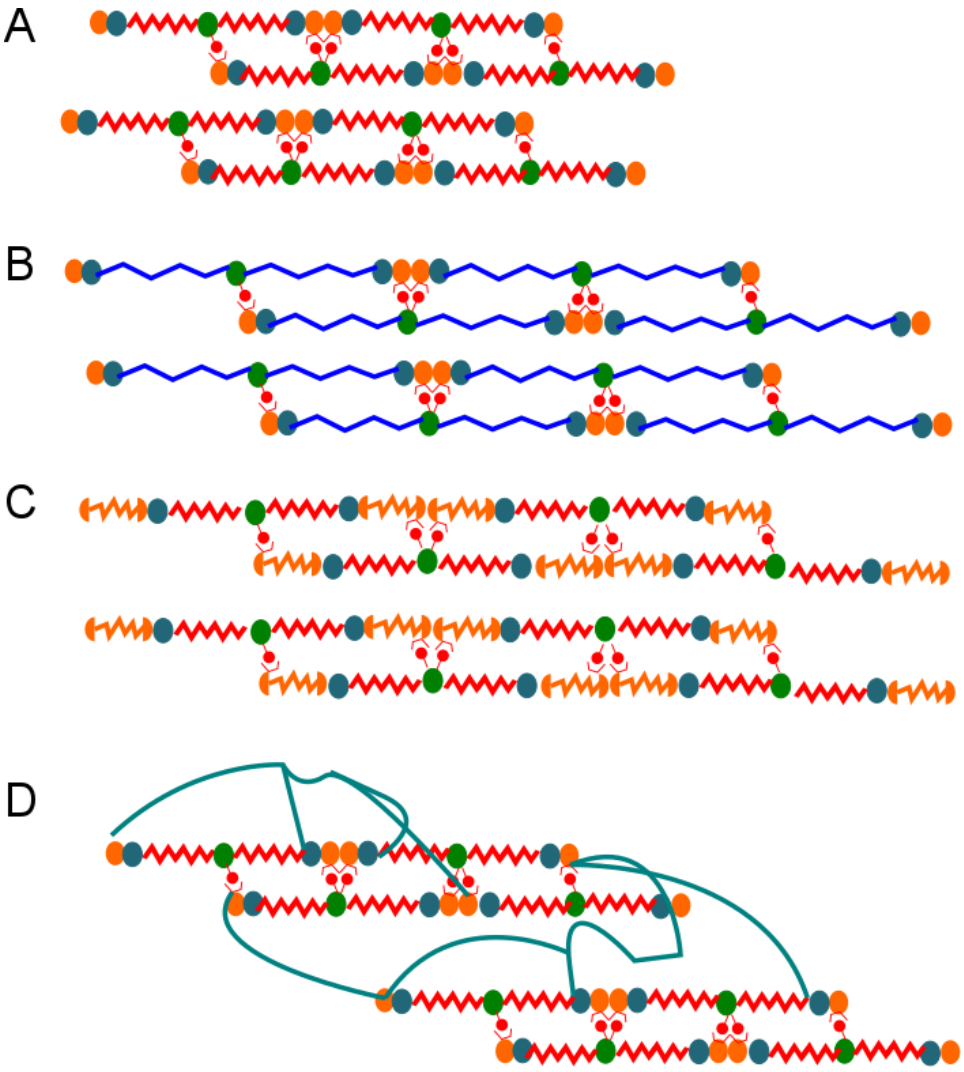


Figure 6 Multiple hypothesized unfolding mechanisms of fibrin. Unstretched fibrin (A) with coiled coils (red) between the D region (light blue and orange circles) and the E region (green circles). In (B), the coiled coils between the D region (light blue and orange circles) and E region (green circles) are unfolding into β-sheets (blue). In (C), the γ-module (orange) in the C region is unfolding. In (D), the αC regions (blue) of the D regions are stretched.[31]

The hierarchical structure and corresponding mechanics of fibrin networks has been characterized at different scales with different techniques. Previous research has been shown that on the molecular level, that fibrin can be unfolded under tensile force in single-molecule experiments using atomic force microscopy (AFM).[32] Further experiments indicate that structural transitions of the coiled-coil α-helices in fibrin monomers must play a role in the elongation of fibrin, starting at 15 % tensile strain.[8] Litvinov and coworkers showed by Fourier transform infrared spectroscopy (ATR-FTIR) that the secondary structure content of fibrin gels was altered under compression and tension.[33, 35] The spectral analysis of the amide I and

amide III vibrational bands exposed that relaxed human fibrin gels contained 31 % α-helix, 37 % β-sheet, and 32 % turns, loops, and random coils, which altered to the amount of 16 % α -helices and 52 % β-sheet structures under large (400 %) extensional strain.[16, 33-34]

Recently, BCARS measurements have been used to quantify the (lack of) uniformity in mechanically induced secondary structural changes of fibrin gels under tensile strain. Consistent with Litvinov et al., it was shown that the amount of β-sheet increases when the samples are stretched to 90 % tensile strain. In partially cross-linked fibrin and cross-linked gels the amount of β-sheet increased to a final amount of 42 % and for cross-linked gels to 52 %, respectively, from a starting value of 37 %. Hydrogels that were only partially cross-linked yielded a lower content of β-sheet over the entire range of strains compared to additionally FXIIIa-cross-linked fibrin. It was shown that the amount of α-helical structure decreased with increasing deformation and increasing contribution from β-sheet structure. While the α-helix content of the cross-linked fibrin gel did not stabilize – even at 110 % strain, the amount of α-helix in the partially cross-linked seemed to stabilize at 25 %. The contribution of random coil structure remained roughly constant for all strains. By structural mapping of relaxed and deformed fibrin gels, the local composition of secondary structure was shown to become inhomogeneous with increasing tensile load, which indicates a non-uniform force distribution.[16]

Combined with previous rheological studies, a physical-chemical description of fibrin at the macroscopic (from rheology and microscopy) and molecular (from spectroscopy and scattering) scale in response to strain gets more and more detailed. The mechanical response for shear strains up to 100 % strain observed by rheological studies can be explained by single fiber mechanics.[11] The possibility of combining confocal microscopy with rheology has been demonstrated to monitor fiber morphology during deformation[35-39] The origin of lengthening of the fibrinogen molecule is still debated[73], and conversion from a α-helical to an extended β strand structure under strain, unfolding of the γ-modules[29]; and unfolding of the αC region[31] may all be part of the molecular mechanism that endows fibrin fibers with their extraordinary elasticity.[32] Previous research on the

molecular level, to quantify the unfolding of the α-helical coiled coils into β strands has only be done under tensile force.[16]

Since the bulk of existing literature about fibrin mechanics is almost exclusively in shear and the information about molecular changes is almost always in tension, the identification of molecular changes under high shear strains and further quantification could lead to thoroughly understand the mechanical properties of fibrin. Specifically, such measurements will provide critical information about when (and if) molecular unfolding truly begins to dominate the mechanical response of fibrin under shear deformation.

## 2.3. Rheology

The mechanical properties of a material can be characterized by rheology, where either a defined tensile or shear deformation is applied to the sample, and its force response is recorded. For soft materials, such as fibrin gels, most studies use shear rheology as it requires less sample volume, allows more straightforward experiments compared to tensile measurements, and samples do not have to support their own weight.

Shear strain is described as deformation of a body parallel to the face of an element. This induces two parallel forces (F) acting in the opposite direction of a body (figure 7). Strain is generally defined as the ratio of deformation to original dimensions. The applied shear stress σ (measured in Pa) is defined as the ratio of the force F (N) to the sample area A ($m^2$) and shear strain γ (%) is defined as the ratio of the displacement Δx and the sample thickness in the orthogonal plane to the deformation l.

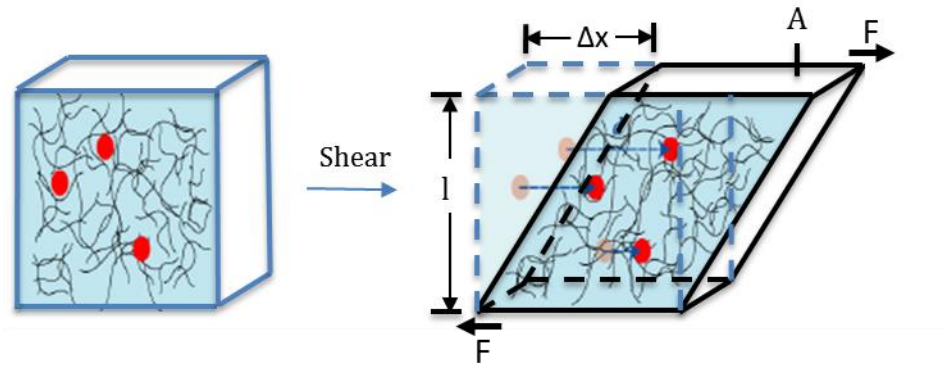


Figure 7 Shear deformation of a fibrin sample with depicted styrene beads (red) used for height determination as described in section 3.4. Where F is the force in N, A the sample area in $m^2$, Δx is the displacement of the material with respect to its initial position and l is the separation height. Light red in the right image mark the original position of the beads.

A shear rheometer probes a sample that is placed between two plates where one is fixed while the other one is coupled to a motor and load sensor device. In order to probe the response of the material, the moveable plate is rotated with varying amplitude and frequency, which then creates a shear strain on the sample.[40,41] The measured torque with respect to the induced deformation is then converted into shear stress. The ratio of the applied shear stress σ (Pa) and strain γ (%) is the shear modulus G (Pa) of the measured sample:

$$G = \frac{\sigma}{\gamma} = \frac{F/A}{\Delta y/l} \quad (1)$$

Besides static deformation, a sinusoidal shear strain can be applied to obtain an in-phase response (associated with elastic behavior) and out-of-phase response (associated with viscous behavior). We therefore define $G = G' + G''$, where $G'$ is the storage modulus originating from the in-phase stress-strain response associated with the elastic behavior, and $G''$ the loss modulus originating from the out-of-phase stress-strain response associated with viscous behavior. Fluids show viscous behavior, hence a fibrinogen solution before polymerization shows a higher value for $G''$ compered to $G'$. The polymerization process leads to the conversion of the fluid monomer solution to the polymer gel state, which can be observed at the point where $G'$ has a higher value then $G''$.[43]

The mechanical properties of fibrin have been studied for many years and it was shown that, unlike simple springs, the material has a complicated force-extension behavior. The linear and non-linear regime of viscoelastic samples can be studied by rheological strain sweep measurement. In this method, the moduli are measured as a function of strain amplitude for a constant frequency.

## 2.4. Microscopy

### 2.4.1. Optical microscopy concepts

Optical microscopy uses the visible range of the electromagnetic spectrum (400 to 700 nm) and a system of lenses to generate a magnified image of a sample. In conventional light microscopy, the magnification is implemented by using refractive optics.

Conventional microscopes are limited in their resolution – their ability to distinguish two close-by separate points. Because of diffraction (bending of light while passing an obstacle or a slit, resulting in a change of the directions and intensities) , a single point will be depicted from any optical system as an Airy pattern where the central maximum has a finite area (figure. 8 (A)). As a consequence, the smallest distance $d$ to be resolved by the microscopy is defined by the Abbe limit as:

$$d = \frac{\lambda}{2n \sin \alpha} \tag{2}$$

Where λ represents the wavelength of the illuminating light, n the refractive index of the medium in front of the lens and α the maximum half-angle range of the lens as depicted in figure 8 (B). In microscopy, a common concept for describing the resolving power of an objective lens is the numerical aperture (NA).[43]

$$NA = n \sin \alpha \tag{3}$$

In modern optics, the NA can reach up to 1.49, which limits the resolution in microscopy using visible light in a range of 400 – 700 nm to ~ 200 nm in principle.

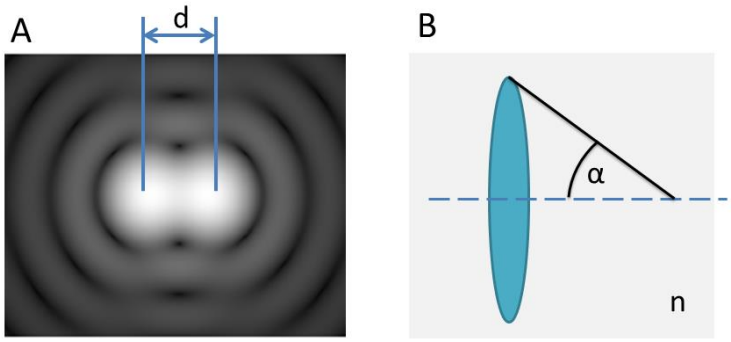


Figure 8 Airy pattern of two point sources at the minimal distance to resolve both points (A). Schematic drawing of the numerical aperture showing the maximum angle α of a lens in a medium of refractive index n (B).

The enlargement of a species through a microscope is called magnification. Magnification is the ratio of the image size to the object size, and thus it is a dimensionless number.[44]

### 2.4.2. Confocal microscopy

Confocal microscopy is an advanced optical microscopy technique routinely used across life sciences to image fluorescently labelled specimens. In contrast to a conventional microscope, which captures the complete two dimensional (2D) frame at one time, the laser scanning confocal microscope (LSCM) uses a pinhole to only detect light from a single point at a time. This pinhole is positioned in an optically conjugate plane in front of the detector and removes out-of-focus signals resulting in better contrast and an improved lateral and axial resolution. This requires that the point illumination must be rastered over the field-of-view to create a 2D image of the sample. However, to obtain the increased resolution, a substantial amount of fluorescence intensity needs to be blocked out by the pinhole. This makes long exposure times and high laser intensities necessary, which renders achieving improved resolution fairly with a confocal microscope fairly impractical.[45, 46]

As described above, in a confocal microscope the specimen is excited by a single point of light from a laser, and the point is scanned in a raster pattern, sequentially building up a 2D image as the emissions are simultaneously collected through a confocal pinhole. The scanning process is slow, with images collected at around one frame per second, so there is a trade-off between image resolution and speed. Even though there are high-speed scanning-systems capable, the rate of image acquisition is limited by the number of photons of fluorescence that can be collected from a diffraction limited area in the sample.[47]

### 2.4.3. Spinning disk confocal microscope (SDCM)

3D imaging over time places the strictest requirements on an imaging system, requiring high lateral and axial resolution, high speed, and sufficient fluorescence intensity to provide usable images with minimal illumination. The spinning disk confocal microscope (SDCM) is a way of rapidly collecting confocal images by decreasing the time required to capture a single 2D image by having parallel illumination points acquired simultaneously. SDCM supports acquisition rates up to 2000 frames per second capable of capturing 3D-imaging of cellular dynamic combined with high signal-to-noise ratio.

Instead of sequentially scanning the sample by a focused laser beam as in LSCM, in SDCM an expanded beam passes the collector disk, which is an array of microlenses that each create a diffraction-limited illumination spot. The confocal image is conducted by simultaneously scanning the array of diffraction-limited points across a sample, and collecting fluorescence emissions through a set of confocal pinholes. Each pinhole associated to a microlens is co-aligned on a pinhole disk. A dichroic mirror between the two disks reflects emission wavelength to separate the laser emission from any reflected or scattered excitation light from the microscope optics. The geometry of the emission path results in a confocal fluorescence signal with extremely low background noise. The disks rotates rapidly enough that the points of fluorescence effectively merge into a 2D image that can be collected with a CCD.[47-49]

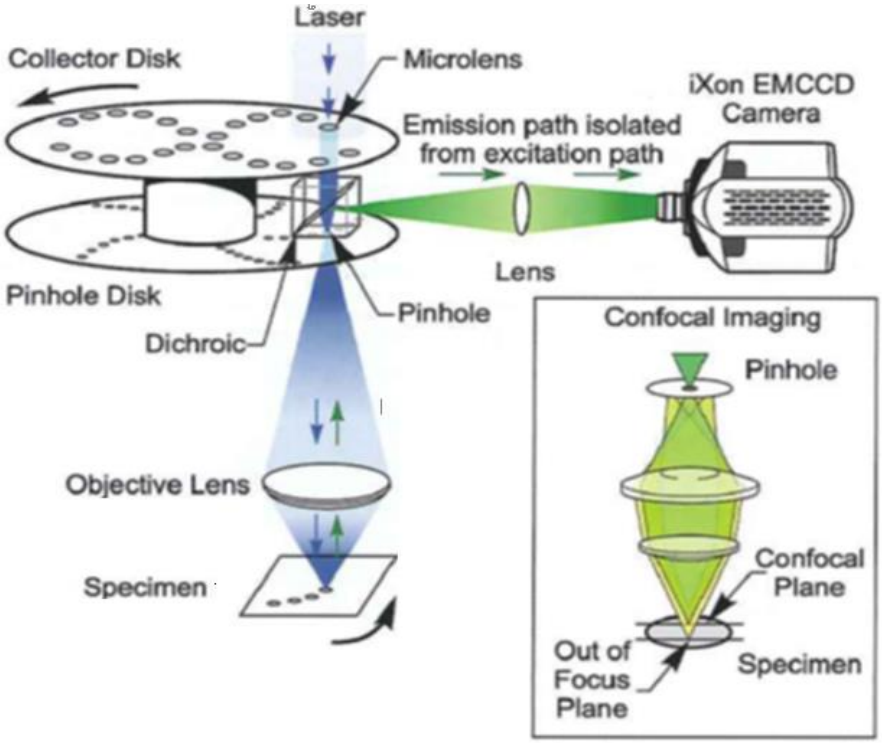


Figure 9 Scheme of a spinning disk confocal microscope. The collector disk contains microlenses that are positioned in a way that each pinhole associated to the microlenses is co-aligned on a second pinhole disk. The disks are fixed to an electric motor shaft where they are separated by a distance equal to the focal length of the microlenses. Spinning the disks causes an array of focused laser beams to be scanned across the specimen. The fraction of the in-focus fluorescence emission light passes to the pinhole array and is reflected into the camera port.[49]

## 2.5. Vibrational Spectroscopy

Vibrational spectroscopy is based on the interaction between electric fields and material. Molecular vibrations can be probed by light as the frequency corresponds to energy transitions of electronic, translational, rotational, and vibrational motions in molecules. The possible modes of vibration of a molecule are determined by its different functional groups, reduced masses and bond strengths. Both infrared-absorption (IR) and Raman-scattering contain specific information on the structure of the molecule and its environment.[49-53] After electronic transitions (often in the ultraviolet part of the spectrum from wavelength of 200nm to 780 nm), vibrational transitions correspond to the largest energy differences that take place in a molecule. Besides molecular vibrations there are always molecular rotations excited. However, these can be neglected as rotational energies are much smaller than vibrational energies and beyond the resolution of conventional vibrational spectroscometers.

### 2.5.1. Degrees of freedom

Atoms in molecules are constrained by molecular bonds. The allowed movement of atoms in a specific way is called degree of freedom. The maximum number of potential transitions is 3*N, when considering a molecule of N atoms in a three-dimensional Cartesian coordinate system. The 3*N degrees of freedom are assigned to the translational, rotational, and vibrational motions of the molecule as shown in figure 10. The center of mass of a molecule can move in three directions (x, y and z), therefore every molecule has three translational degrees. Depending on linearity or non-linearity of the molecule, there are two rotational degrees of freedom for linear and three rotational degrees of freedom for non-linear molecules. The total number of translational and rotational degrees of freedom is 6 for linear and 5 for non-linear molecules. All remaining motions are vibrational degrees of freedom. The numbers of vibrational modes for linear molecules is 3*N-5 and for non-linear molecules 3*N-6.[49]

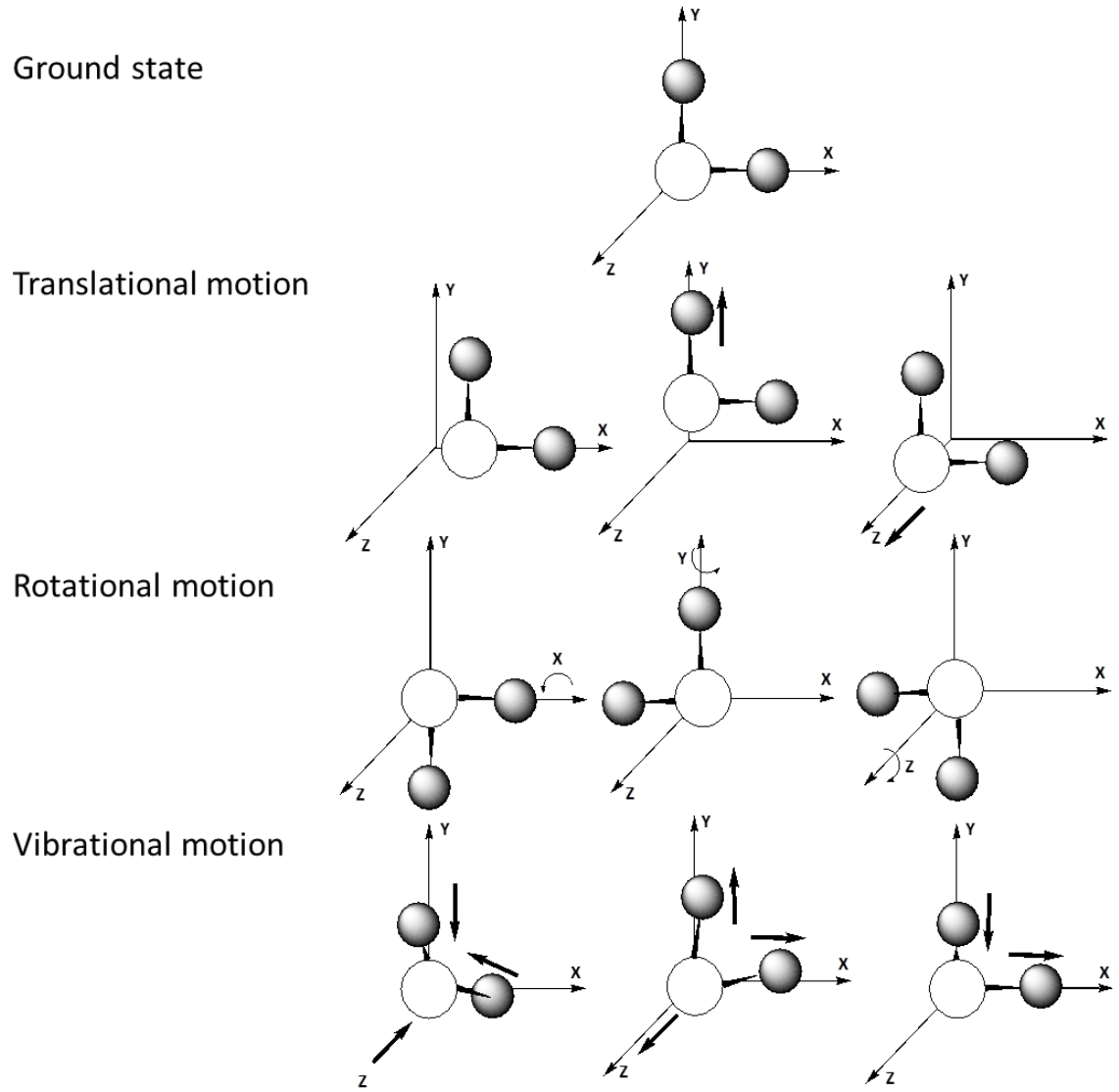


Figure 10 Degrees of molecular motion of an non-linear three-atomic molecule such as $H_2O$. The molecule at rest is shown at the top. The molecule can move in three translational motions(x, y and z) as well as rotate around the three axes. Of the nine total motions allowed by the degree of freedom only three are left for vibrational motions. These are shown as symmetric and anti-symmetric stretching and bending vibrations.

Table 1 Degrees of freedom corresponding to type of motion for any molecule with N atoms. The total number of degrees of freedom for any molecule is 3*N.[49]

| **Motion** | **Degrees of freedom** |
|---|---|
| Translation (position of the molecule) | 3 |
| Rotation (about the centre of the molecule) | 3 (nonlinear) |
| | 2 (linear) |
| Vibration | **3N**-6 (nonlinear) |
| | **3N**-5 (linear) |

According to the rule of mutual exclusion no normal mode, in a molecule with a center of symmetry, can be both IR and Raman active. Vibrations are Raman active

when a change of polarizability occurs. The mode needs to be of *gerade* (g) symmetry with respect to the inversion point (i). IR active modes, involving the change of the dipole moment, must be non-symmetrical (ungerade (u)) with respect to the inversion point (i).If a molecule has no center of symmetry, as for example $H_2O$, some but not necessarily all vibrational modes may be both IR and Raman active.[54, 55]

### 2.5.2. IR Absorption and Raman scattering

Electromagnetic radiation with a wavelength starting at 780 to 1000 nm is defined as near-infrared (near IR), which is larger than typical vibrational energies in biological or biomaterial systems. Mid-IR, corresponds to energies similar to translational, rotational, and vibrational energy transitions. However, the primary transitions in the IR region are vibrational. If the energy of radiation is of suitable wavelength, the incident photon can get absorbed while promoting the transition of two vibrational states, and transiently changing the dipole moment of the bond. These modes of vibration are indicated by absorption bands in an IR spectrum and are called IR-active.[49] As a side note, IR absorption spectroscopy is the vibrational analog to UV-VIS absorption spectroscopy that probes electronic absorptions.

Radiation with greater energy than required for translational modes, such as visible or near IR light, can also provide information about molecular vibrations in molecules via indirect or inelastic scattering. When an incoming photon in not resonant with any transition in a molecule it exchanges energy with the molecule, mediated by the polarizability of the system, and promotes transition to so-called virtual states. From the virtual state, three different relaxation pathways are possible (figure 11B). Rayleigh scattering, which is the most probable process with a cross section of $I_{Rayleigh}/I_{Incoming}\sim10^{-5}$, is the elastic scattering of radiation. The incoming photon is scattered with the same frequency $\nu_0 = \nu_{Rayleigh}$ and the transition starts and finishes at the same vibrational energy level.[50, 51] In addition to Rayleigh scattered light, inelastic Raman scattering can take place. This process is less probable with $I_{Stokes\_Raman}/I_{Incoming}\sim10^{-8}$. First, an incident photon is absorbed by the molecule, which becomes excited into a virtual energy level.

Immediately after the absorption, the molecule spontaneously falls back to a vibrational (not ground) level and emits a photon with the corresponding energy difference. The energy of the incident photon is partly converted into molecular vibrations with a corresponding change in the polarizibility of the system while the remaining energy is transferred to an emitted photon. The resulting, Stokes-scattered photon has a lower energy than the incident one and is therefore red-shifted. With even lower probability of occurrence, anti-Stokes Raman scattering is also possible. Anti-Stokes Raman has a probability $I_{anti-Stokes\_Raman}/I_{Incoming}\sim10^{-11}$, and occurs when an incoming photon interacts with a vibrationally excited molecule. The anti-Stokes Raman scattering process results in a transfer of energy from the molecule to the scattered light. Therefore anti-Stokes Raman photons are of higher energy than the incident photons and blue-shifted in frequency.

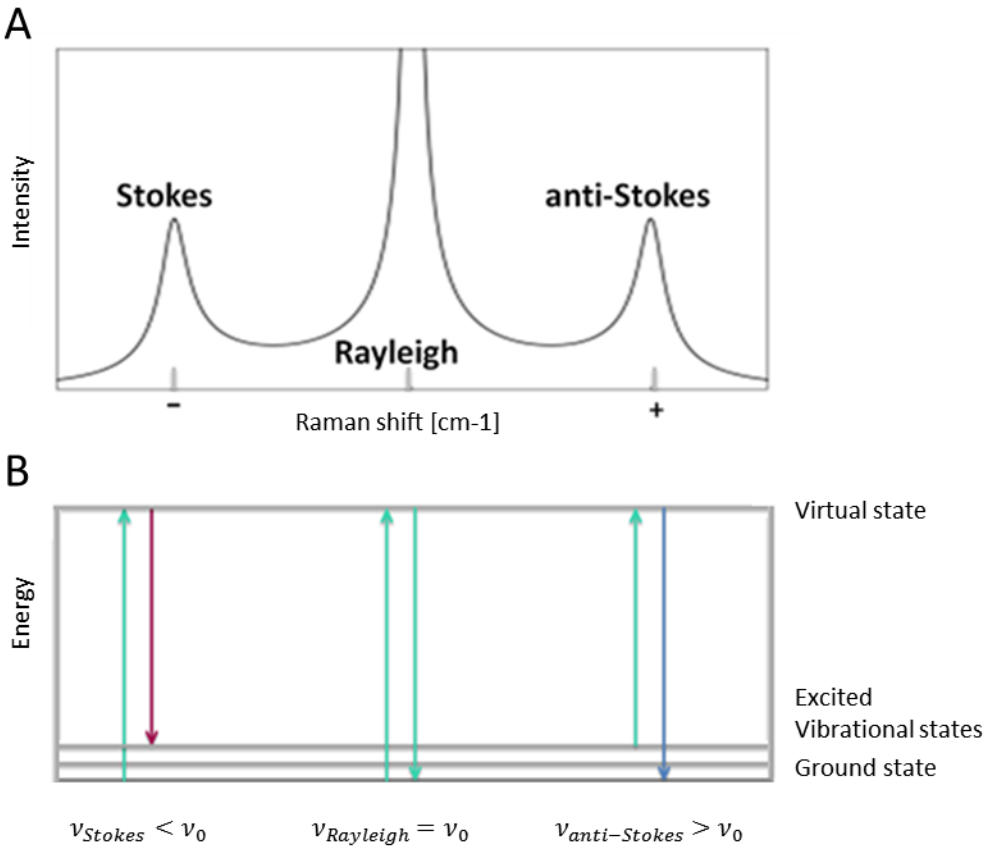


Figure 11 Schematic spectrum from a scattering process (A). The energy shift between the incoming and outgoing light is called Raman-shift with the dimension cm-1. In the Stokes process a phonon is generated and its energy is subtracted to the energy of the incoming photon (left). In the anti-Stokes process a phonon is annihilated and its energy is added to the energy of the incoming photon (right). Rayleigh scattering (middle) defines zero since the frequency of the incoming and outgoing photon stays the same. (B) shows the energy level of Stokes scattering (left) the process starts at the ground state and ends at an excited vibrational level, therefore the frequency of the scattered photon is red-shifted. Rayleigh scattering (middle) starts and ends at the ground state, the frequency of the scattered photon is the same than of the incoming. Anti- Stokes scattering starts at an excited vibrational level and ends at the ground state, the frequency is blue-shifted.

### 2.5.3. Raman spectroscopy of biological samples

A major advantage of Raman spectroscopy compared to infrared spectroscopy for biological samples such as cells, tissues, or protein hydrogels comes from the strong absorbance of water at ~ 1600 $cm^{-1}$ (OH bending mode) for infrared radiation, which shows only weak Raman scattering.

The Raman spectrum of biological samples contains chemical information in the form of peaks that can be assigned to tabulated molecular vibrations.[56] Furthermore, the Raman scattering is quantitative and linear with concentration. Especially the fingerprint region between 800 $cm^{-1}$ to 1800 $cm^{-1}$ is rich in spectral features, from which the amide I band is of particular interest for this study since it is sensitive to protein secondary structure.[57-59] An typical Raman spectrum of the fingerprint region, collected from an biological cell is depicted in figure 12 (reprinted from ref 54).

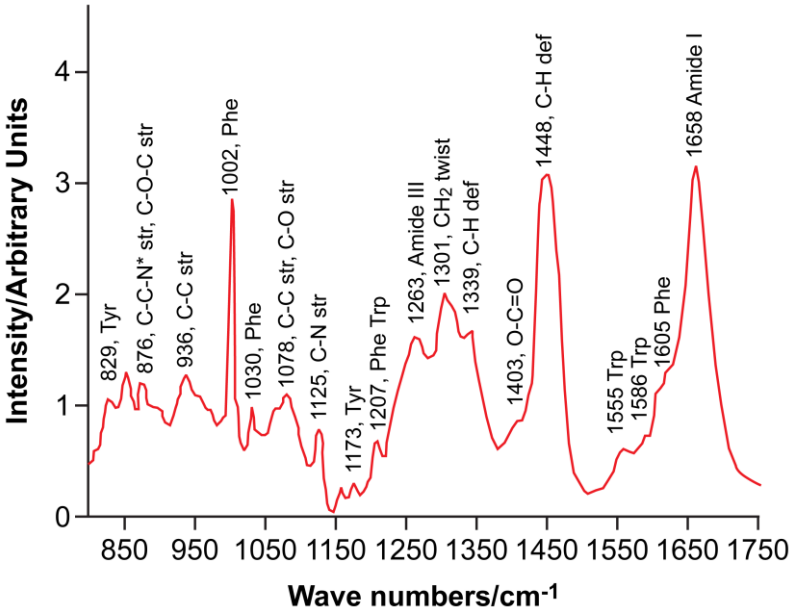


Figure 12 Average Raman spectrum collected from the cytoplasm of a mature oocyte annotated to show the major peaks present in the wavenumber region 800–1760 $cm^{-1}$, which can be attributed to specific proteins or lipids.[60]

The amide I vibration band corresponds to the NH-coupled C=O vibration that is present in every protein. The secondary structure of proteins such as α-helix and β-sheet is stabilized by hydrogen bonds. The C=O group in an α-helix is hydrogen-bonded to the secondary amines of another peptide bond in parallel direction to the

helical axis whereas the hydrogen bonds that stabilize β-sheet are formed orthogonal to each β-strand.[57] Because of the local hydrogen bonding that stabilize α-helix and β-sheet is unique, the vibrational resonance is distinct for each secondary structure with α-helix having a Raman peak located at 1640 $cm^{-1}$and β-sheet at 1667 $cm^{-1}$.[16]

Since Raman scattering has a low cross section, it is necessary to integrate sufficiently long (up to minutes) and employ high laser intensity to reach a useful signal-to-noise level. Unfortunately, this has the drawback of possible sample damage[49], and the additional generation of a fluorescent background signal - as the Stokes-scattered signal is red-shifted like fluorescence – makes Raman scattering challenging in biological systems.

### 2.5.4. Coherent anti-Stokes Raman scattering spectroscopy –CARS

In the middle of the 20th century, a new technique to circumvent the low signal limitation of spontaneous Raman scattering was developed. Coherent anti-Stokes Raman Scattering (CARS) was first observed in 1965 by Maker and Terhune at the scientific laboratories of Ford Motor Company.[56] The development of CARS went hand in hand with the arise of lasers being strong enough to induce multi-photon processes.

CARS is a third-order nonlinear process involving the interaction of four photons with the sample as depicted in figure 13. The pump photon of frequency $\nu_{Pump}$ and the Stokes photon of frequency $\nu_{Stokes}$ resonantly drive a molecular vibration, creating a polarization between the ground and excited vibrational states. The probe photon of frequency $\nu_{Probe}$ upconverts the polarization to a virtual level, from where the system relaxes to the ground state while emitting the anti-Stokes photon at a frequency $\nu_{anti-Stokes}$. The relationship of frequencies for $\nu_{anti-Stokes} = \nu_{Pump} - \nu_{Stokes} + \nu_{Probe}$ can be simplified to $\nu_{anti-Stokes} = 2\nu_{Pump} - \nu_{Stokes}$ by using the same frequency for the pump and the probe photon. The anti-Stokes process is

resonantly enhanced, if the difference $\nu_{Pump} - \nu_{Stokes}$ matches the frequency of a vibrational resonance $\nu_{Res}$ of the molecule.

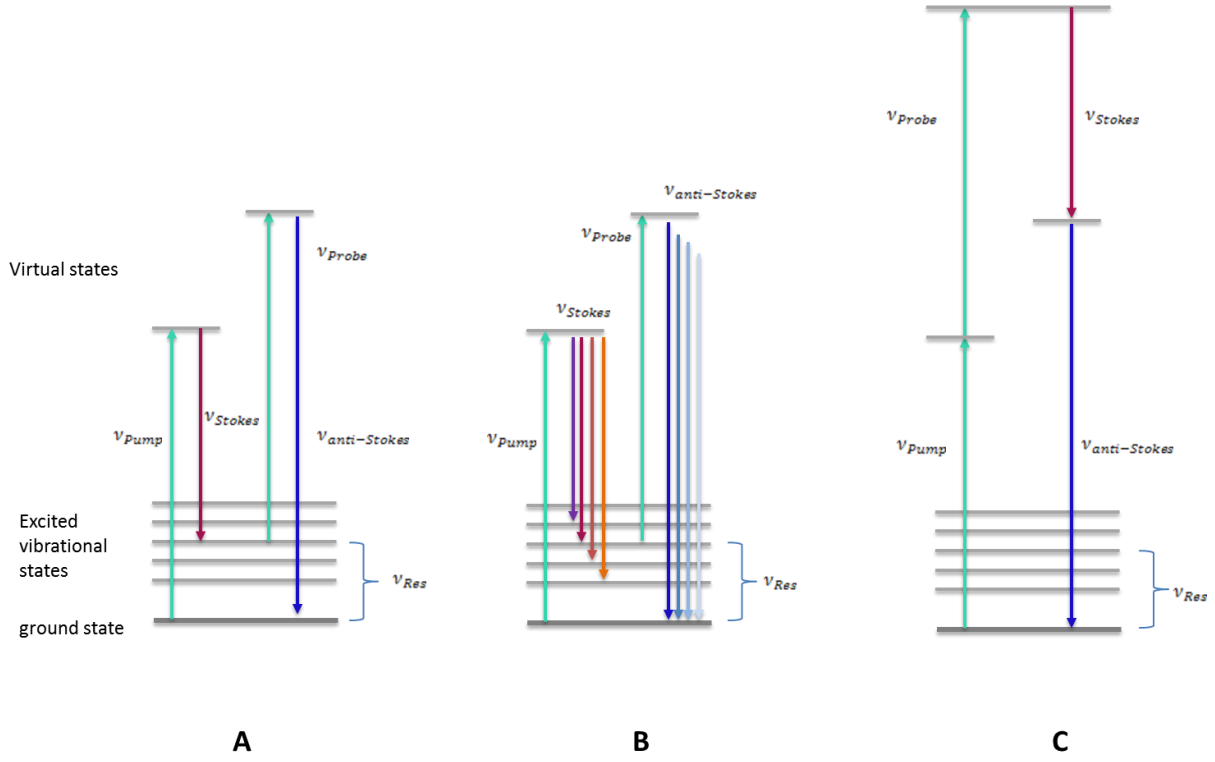


Figure 13 CARS energy level diagrams of (A) vibrationally resonant interaction (B) broadband vibrational excitations. (C) non-resonant interaction.

Due to the resonant driving of a vibrational mode, the signal caused by the CARS process is much stronger than spontaneous Raman scattering. Because of the active pumping of Raman modes, the transitions involved in the CARS process are not spontaneous. The process is coherent since the phase of the CARS light must match that of the driving fields, with highly directional emission of the CARS signal, as a consequence. The blue-shifted detection of the anti-Stokes signal is not affected by the one photon fluorescence background.

The polarization *P* driven in a sample for spontaneous Raman scattering is given in (4) and for CARS in (5). Below, I briefly discuss *P*, to further examine important characteristics of the CARS signal. Linear *P* in a material develops from interaction with an electric field as:

$$P = \epsilon_0(\chi * E) \tag{4}$$

Where $\epsilon_0$for the permittivity of free space, $\chi$ for susceptibility which is a constant of proportionality containing the vibrational information and $E$ for the electric field. Generally speaking, nonlinear polarizations also develop in materials where the field strength is strong enough. Therefore the general polarization takes the form below:

$$P_i = \left[\chi^{(1)} + \chi^{(2)}_{ijk}E_jE_k + \chi^{(3)}_{ijkl}E_jE_kE_l \ldots\right] \tag{5}$$

Where $\chi^{(2)}_{ijk}$ and $\chi^{(3)}_{ijkl}$ are so-called nonlinear susceptibilities. The nonlinear susceptibilities contain resonant (figure 13 (A)) non-resonant terms (figure 13 (C)). This means that spectra obtained from BCARS include a resonant and nonresonant component because $\chi^{(3)}$ contains both a resonant and non-resonant term. The non-resonant component of $\chi^{(3)}$ gives no information about the chemical nature of the sample, is present at the exact same wavelengths as the vibrationally resonant CARS light, and the electric fields add. The non-resonant signal is purely real – electronic distortions linked to virtual transitions – whereas the Raman transition is complex since it involves a transition to an actual vibrational state.

In the work discussed in this thesis, we obtain a broadband vibrational spectrum (800 – 4000 $cm^{-1}$) by using a spectrally broad Stokes beam (λ = 400-2400 nm), which produces a manifold of vibrational excitations (figure 13 (B)). Instead of measuring single intensities (single-line CARS) with spectrally narrow Stokes beams, we obtain whole vibrational spectra of all vibrational modes in a range of 800 – 4000 $cm^{-1}$. We can use a mathematical transformation to extract resonant part of $\chi^{(3)}$, which gives quantitative, linear Raman-like spectrum of the sample of interest via phase retrieval.[61, 62] Of note is that single-line CARS (Figure 13 (A)) is semi-quantitative (at best), but it is substantially faster than spectral CARS due to the spectral focusing of all energy into a signal vibrational transition.

# 3. Experimental procedures

## 3.1. Materials

Human fibrinogen Plasminogen Depleted (FIB-1), human thrombin (HT 1002a), human fibrin stabilization factor (HFXIII) and Alexa 488 labeled fibrinogen were obtained from Enzyme Research Laboratories (UK). Calcium chloride (CaCl2), Sodium chloride (NaCl), Sodium hydroxide (NaOH), (4-(2-hydroxyethyl)-1-piperazineethanesulfonic acid (HEPES) and (3-Aminopropyl)triethoxysilane (APTES) were purchased from Sigma Aldrich (Germany). Glutaraldehyde 25 wt% in $H_2O$ was obtained from Acros organics and Polystyrene 3 μm microspheres from Polyscience. All chemicals have been used without further purification.

## 3.2. Fibrin gel preparation – general procedure

Human fibrinogen was received from Enzyme Research Laboratories at a concentration of 44.44 mg/mL. The Fibrinogen was diluted in a buffer solution made of 20 mM Hepes and 150 mM NaCl dissolved in deionized water and pH was adjusted to 7.4. The solution was placed in an Eppendorf Thermomixer for 30 minutes at 300 rpm to support the dilution. To remove insoluble protein the mixture was filtered through a syringe filter with 0.2 μm pore size. Fibrinogen solutions were aliquoted in single used size of 100 μL and frozen in liquid nitrogen and stored at -80°C.

Human thrombin was received with catalytic activity of 3022.00 NIH U/mg. Thrombin was hydrated in Milli-Q water to the original volume of 97 μL. Aliquots in single used size of 5 μL were frozen in liquid nitrogen and at stored at -20°C. Alexa 488 labeled human fibrinogen was handled as described for unlabeled fibrinogens except preventing the samples from light to avoid photobleaching.
To make the fibrin gel preparation as perspicuous as possible, working solutions of both buffer and thrombin with additional $CaCl_2$ have been prepared.

**Fibrinogen Solution**: 10 mg/ml or 20 mg/ml of protein in buffer (20 mM Hepes and 150 mM NaCl)

**$CaCl_2$-buffer Solution**: $CaCl_2$ (25mM) in buffer (20 mM Hepes and 150 mM NaCl)

**Thrombin-$CaCl_2$ Solution**: Thrombin (21u/mL) + $CaCl_2$ (5mM) in buffer (20 mM Hepes and 150 mM NaCl)

To polymerize a fibrin hydrogel of 100 µL Volume, the working solutions were mixed the following way:

**75 µL Fibrinogen Solution**

**20 µL $CaCl_2$-buffer Solution**

**5 µL Thrombin- $CaCl_2$ Solution**

With Final concentrations of:

| **Fibrinogen** | **$CaCl_2$** | **NaCl** | **Thrombin** |
|---|---|---|---|
| 7.5 $mgmL^{-1}$ | 5 mM | 150 mM | 1.05 $umL^{-1}$ |

All fibrin gels were polymerized for at least for 2h at 37°C in closed containers with a reservoir of buffer solution to create a saturated atmosphere and prevent dehydration. Different materials to polymerize the gel, as for example a Teflon mold, have been used. Details are described in the related sections.

## 3.3. Confocal microscopy – manual shear strain measurements

The fibrin samples for confocal microscopy were prepared as described in 3.2. A Fibrinogen Solution containing 7.5 % Alexa 488 labeled fibrinogen and 92.5 % unlabeled fibrinogen was used to create sufficient fluorescence signal from fibrin fibers. The sample preparation was done in dark ambient to avoid photobleaching of the samples.

The effect of shear strain on the orientation of fibrin fibers was studied with the manual shear cell as shown in figure 14. The same setup was used for BCARS measurements (Section 6.3.)

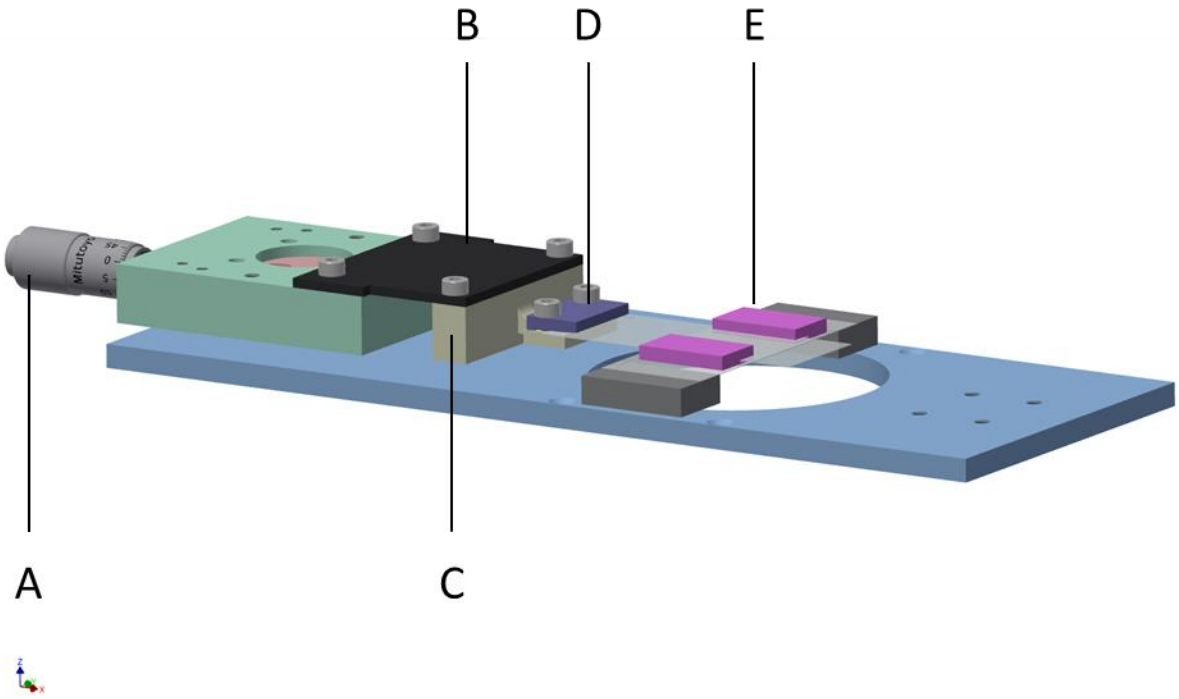


Figure 14 Schematic figure of the manual shear cell setup. (A) Micrometer for the displacement Δx of the top glass plate. (C) Solid connector and adapter plate for micrometer (B). (D) Metal clamp for holding the top glass. (E) Aluminum spacer to define a gap size of 300 µm between the top and the bottom glass plate. Drawing from Marc-Jan van Zadel, MPIP Mainz.

Fibrin was polymerized directly between coverslips (60x30x0.15mm, Menzel-fisher scientific) which were separated by two aluminum spacers to produce fibrin gels with defined height of 300 µm (figure 15).

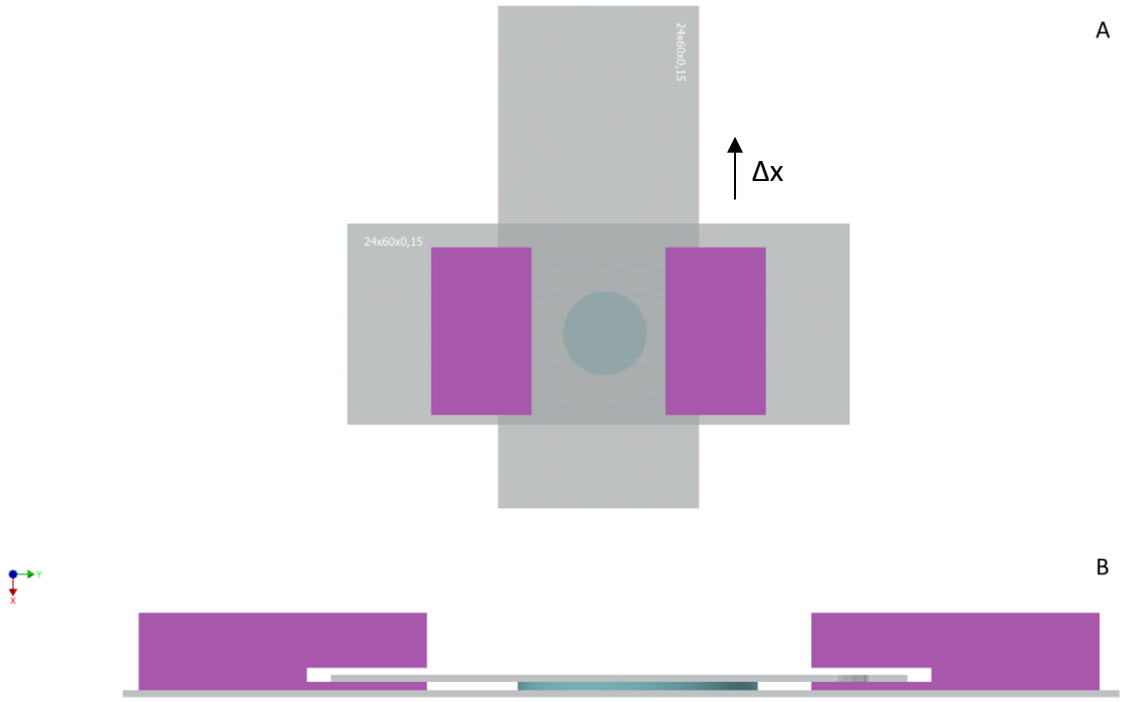


Figure 15 The Fibrin preparation for confocal microscopy to study the effect of shear strain on fiber orientation. To define a specific height, the two cover slips were separated by a spacer (pink). The top coverslip was pinched by the spacer and the fibrinogen solution was added. The bottom coverslip was attached with superglue (LOCTITE, Henkel) immediately after adding the fibrinogen solution. To apply shear strain the top coverslip was moved as indicated by the arrow (Δx). Drawing from Marc-Jan van Zadel, MPIP Mainz.

Images were taken with a TCS SP5 confocal microscope (Leica, Germany) with laser excitation at 488 nm (Alexa488) and a 63x, 1.4 NA oil immersion objective lens. A z-stack of 55 steps with a step size of 0.25 µm was taken from the sample to capture a volume of 13.585µm thickness at every shear strain. Each image in the stack had 1024 pixel x1024 pixels corresponding to a field-of-view of 64.51 µm x 61.51 µm with optical zoom of 2X. Image handling was performed in ImageJ. The z-stack was resliced along the XZ plane to obtain a lateral view of the sample. A maximum intensity XZ projection was saved and used for as input to SOAX (a fiber tracking software) for calculating fiber orientation.[63]

## 3.4. Confocal microscopy – automated shear strain measurements

The shear cell in Prof. Gijsje Koenderink's group at the FOM Institute AMOLF offers the capability to image a biopolymer network while a shear strain is applied in an automated fashion. The morphological response of the network, particularly the fiber orientation, can be studied during dynamic deformation.

Automated shear strain measurements were done at a setup described in detail by Izabela Katarzyna Piechocka.[64] For those experiments, fibrin samples were prepared as described in 3.2 except for a lower amount of only 5 % Alexa 488 labelled fibrinogen in the initial solution. In addition, fluorescent polymer microspheres (Alexa 594 labeled) with a diameter of 0.21 µm were used for the gap size measurements (see below). The gel was polymerized directly in the shear cell shown in figure 16. Therefore, the solution was pipetted on the bottom coverslip (32x24x0.15mm, Menzel) and water was added in the solvent trap (figure 16 A, 2) to prevent dehydration, before the metal core (figure 16 B) was placed on the bottom plate (figure 16 C).

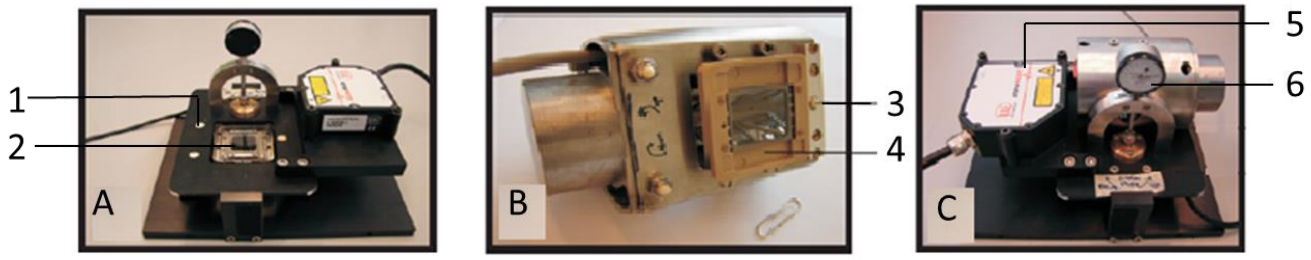


Figure 16 (A) Photograph of the shear cell bottom plate with screw legs for parallel alignment of the two glass coverslips (1) and bottom glass slide holder with solvent trap (2). (B) Bottom view of the hinge-spring system, showing the moveable top glass holder with a glass slide (4) and three screw legs used to align the plates (3). (C) Photograph of the fully assembled shear cell with position sensor (5) and micrometer screw for gap adjustment (6). [64]

The displacement of the top plate was determined by interferometry, while the bottom plate was kept fixed. Shear deformation was applied with offsets from 20µm up to 800 µm in different step sizes. Z-stacks were taken from a representative sample of a thickness of 30 µm imaged with a step size of 0.6 µm for every offset. Images were taken with Leica DM IRB inverted microscope with a 100x, 1.2 NA oil

objective, which was connected to a Yokogawa CSU-22 spinning disk and a Hamamatsu EM-CCD C9100 Digital Camera. For excitation, two lasers at 488 nm (for fibrin) and 561 nm (for microbeads) were used.
Each individuval XY plane (512 x 512 pixel; 81.92 x 81.92 µm$^2$) was resliced to an XZ stack (512 x 512 pixel; 81.92 x 30.6 µm). Maximum intensity projections of the first 128 slices (from 0 - 20.48 µm) out of 512 (81.91 µm) for every shear strain are plotted in figure 36. Maximum intensity projections of the all XZ sections were analyzed in SOAX.[60]

In order to measure the strain ($\gamma$ ) on a network, the displacement $\Delta x$ and height $l$ of the network must be known ($\gamma = \Delta x/l$). Previous experiments showed, that the gap size between the top and the bottom glass plate varied between 456±42 µm.[65] To reduce this experimental variance the gap size was calculated for every measurement.

The gap size was measured using geometric proportions (figure 17) and by assuming affine shear deformation within the sample. Red fluorescent polymer microspheres were added to the fibrin sample before initializing the polymerization. Then, an oscillation with known amplitude was applied to the top coverslip, while the beads inside of the fibrin gel at a known height (set by the microscope) were imaged.

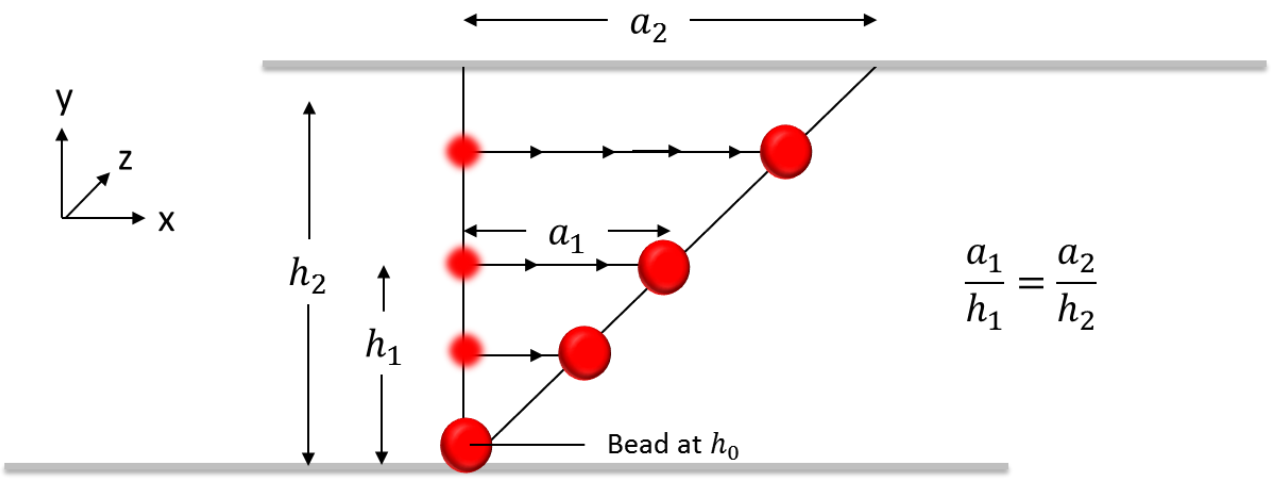


Figure 17 Geometrical proportions of a sample under affine shear deformation. A fluorescent bead will follow the shear by a lateral displacement $a_1$ which is proportional to its normalized distance $h_1$ from the fixed surface. From the known shear amplitude $a_2$ the total gap size $h_2$ can be calculated by the rule of three. The microscope is used set different defined heights in z direction.

The oscillation of the fluorescent labeled beads inside the fibrin gel depends on their height relative to the surface. Both, the distance from the surface of the bottom plate to the beads ($h_1$) and the displacement of the top plate are known ($a_2$). The displacement of the beads ($a_1$) at different known height was obtained by confocal images analyzed via Image J. The gap size was calculated by using the following correlation:

$$h_2 = \frac{h_1 * a_2}{a_1} \tag{6}$$

Were $h_2$ is the gap size, $a_2$ is the known displacement of the top coverslip, $a_1$is the oscillation amplitude of the beads determined by confocal pictures using Image J and $h_1$ is the height of the tracked beads. The absolute heights of the beads were calibrated by establishing h = 0 as the z-position, where the beads showed zero displacement under applied oscillation.

Measurements were performed with an amplitude of 100 µm on the top plate and beads were imaged at depths of 20 µm, 30 µm and 40 µm from the surface of the bottom glass plate (h = 0). The oscillation frequency was 0.2 Hz and 200 images were acquired for every height, each with 512 x 512 pixels (81.9 µm x 81.9 µm) in the XY plane. The image series was analyzed with Image J by tracking five beads for

every depth, and the displacement in the direction of the applied oscillation was determined manually. The correlation was used to calculate the gap size for every measurement according to eq. 6. Note that gap size measurements were not necessary for steady (manual) shear (3.3), since a fixed space was used to control the height in the experiments.

## 3.5. Confocal microscopy – Tensile measurements

Confocal microscopy of tensile strained fibrin was also performed in Prof. Gijsje Koenderink's group at the FOM Institute AMOLF. Tensile measurements required a way to clamp the soft fibrin gels for stretching. This was realized by incorporating Velcro meshes at the two edges as depicted in figure. 18. The fibrin gel used for confocal microscopy was prepared as described in 3.2 but by addition of 5 % Alexa 488 labelled fibrinogen. To prevent photobleaching, all steps of sample preparation were done in the dark. A final volume of 800 µL fibrin gel was polymerized in a Teflon mold with Velcro parts at both ends (figure 18).

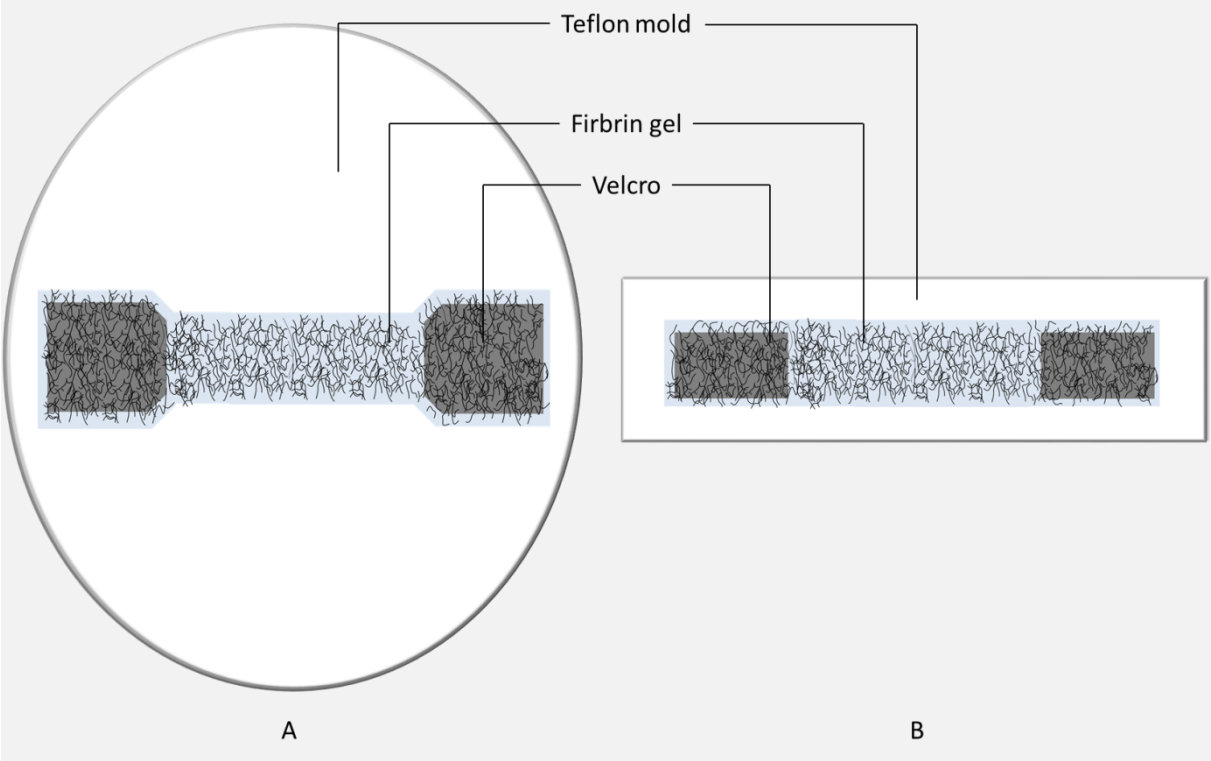


Figure 18 Fibrin gel preparation for tensile confocal measurements. Top view (A) and side view (B). Two Velcro parts placed on the two ends of the Teflon mold. Fibrin solution is covering the mold including the two Velcro part.

After 4h of polymerization the sample was removed from the Teflon mold and placed in the Deben MICROTEST 200N Tensile Stage (figure 18). The stage uses load cells within the range 2N to 200N. The sample was mounted clamped to a pair of jaws with the Velcro parts. A dual threaded leadscrew drives both jaws

symmetrically in opposite directions, keeping the sample centered in the field of view of the microscope.[66]

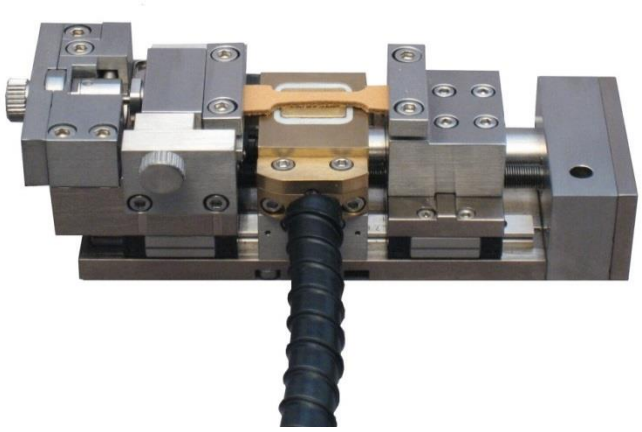

Figure 19 Deben MICROTEST 200N Tensile Stage. Velcro parts of the sample are clamped with the help of two pairs of jaws at each end. A dual threaded leadscrew drives both jaws symmetrically in opposite directions, keeping the sample centered in the field of view of the microscope [66]

The tensile stage was mounted on the Nikon Eclipse-Ti inverted confocal microscope and a 60x water dipping objective (NA = 1.2) and 488 nm excitation for imaging the sample was used. Z-stacks were acquired from the sample covering 20 µm thickness with a step size of 0.5 µm.

The initial length of the sample was measured via a caliper and images were taken of the relaxed sample and tensile strains of 5 %, 20 %, 60 % and 80 %. Z-stacks were acquired for a sample thickness of 151 µm imaged with a step size of 1 µm. The XY plane (512 pixel x 512 pixel; 106.07 µm x 106.07 µm) from one a single z-plane at 50 µm was always used for analysis in SOAX.

## 3.6. BCARS structural imaging

Broadband CARS experiments to analyze fibrin secondary structure were performed on a homebuild setup. The experimental setup is depicted in figure 20. reprinted from and described in detail in ref 16. In short, CARS signal is generated by spatial and temporal overlap of a spectrally narrow pump/probe beam (λ = 1064 nm) and a spectrally broad Stokes beam (λ = 400-2400 nm) in the sample plane. Both beams originate from the same laser source (Leukos-CARS, Leukos) from where half of the intensity is used directly as pump/probe beam and the remaining intensity focused into a photonic crystal fiber to create the supercontinuum Stokes beam. The Stokes beam is clipped by a longpass filter to a spectral range from 1100-1600 nm. The pump and the Stokes beam are transmitted to an inverted microscope (Eclipse Ti-U, Nikon) where they are focused into the fibrin sample via an 100 x air objective (1.2 NA). At the sample the total average laser power is 16 mW. The sample stage to perform manual shear experiments is mounted on a XYZ piezo stage (Nano-PDQ 375 HS, Mad City Labs) to raster-scan with a step size of 0.5 µm. The CARS signal is collected in the forward direction by a second objective (63x IR-VIS, 1.0 NA, water-immersion, Zeiss). The pump and Stokes beam are removed by a notch (NF03-532/1064E-25, Senrock) and a short-pass filter (FES1000, Thorlabs), respectively. The CARS signal is finally dispersed in a spectrometer (Shamrock 303i, Andor) and analyzed by a cooled CCD camera (Newton DU920P-BR-DD, Andor). The grating covered a spectral range from 500 to 4000 $cm^{-1}$. The entire setup is controlled with software written in LabView (National Instruments).[16]

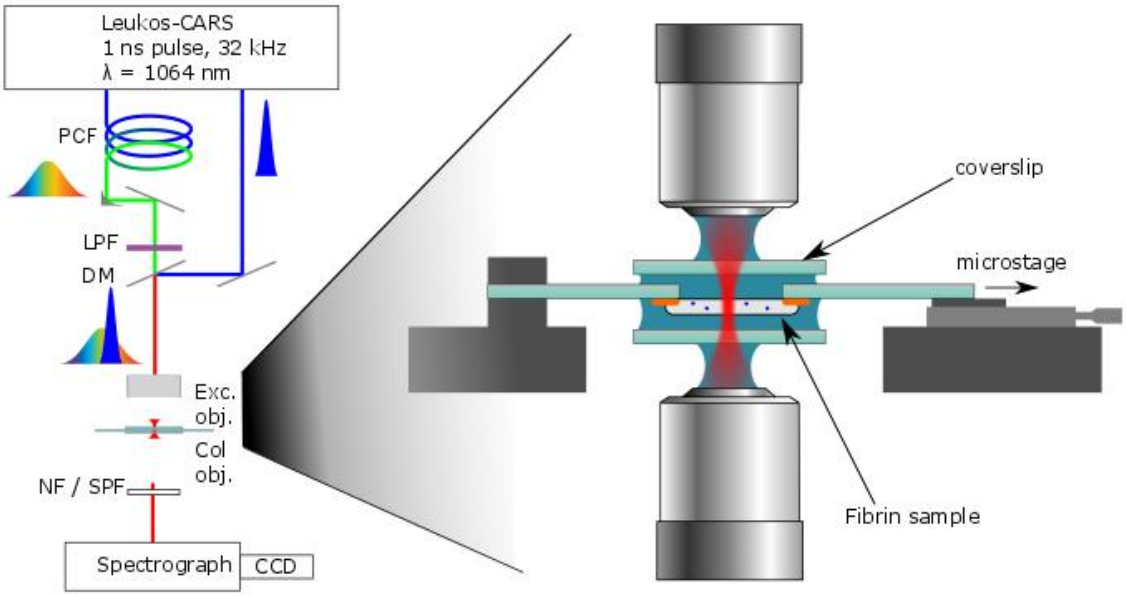


Figure 20 Schematic representation of the BCARS microscope setup on the example of tensile strain measurements. Pump and Probe beam are generated at λ = 1064 nm. The photonic crystal Fiber (PCF) broadens the Stokes beam, which is then spectrally filtered (LPF) to a range of λ = 1100-1600 nm. The beams are combined by a dichroic mirror (DM) and directed to the inverted microscope. Through the excitation objective (Exc. Obj.) the two beams are focused into the sample, and the created forward CARS signal is collected by the collection objective (Col. Obj.). The pump and the probe beam are filtered (NF/SPF) and the CARS signal is analyzed in the spectrograph with an attached CCD camera. Text and Image are taken from ref, 16.

## 3.7. Shear cell for BCARS measurements

Initially, qualitative experiments of fibrin polymerized between two coverslips with a fixed gap made by two aluminum spacers showed a strong contractile (negative) normal force intrinsically present in the network upon polymerization. This is shown in figure 21 where the gel contracts when one of the spacer was removed. The two coverslips (orange and blue) were parallel to each other before removing a spacer.

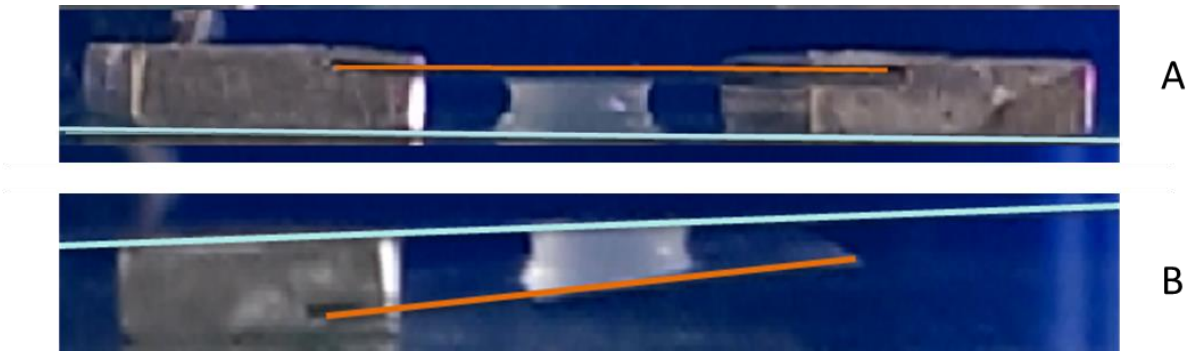


Figure 21 Negative normal force imposed on a fibrin gel polymerized between coverslips separate by two spacer. The top image shows the parallel orientation of the coverslips. Removal of one of the coverslips leads the coverslips moving together imposed by the negative normal force acting on gels polymerized in this geometry (2.1 mm gap size).

It seems as there is excessive normal force acting on the glass plates when the fibrin is fixed into a defined, inflexible geometry during polymerization. It is impossible to measure the normal force when the geometry is constrained as in figure 21A, and the additional normal force – often neglected in shear experiments – may possibly influence unfolding of fibrin secondary structure. Furthermore, as the fibrin gel is not in a relaxed state, it is likely that the protein density is artificially reduced by the imposed geometry. In an attempt to circumvent this issue, a flexible polymerization mold was designed as described below.

### 3.7.1. Minimal loading polymerization mold

To allow the fibrin gel to polymerize under “free” conditions, a minimal loading polymerization mold (figure 22) was designed and built in the MPIP workshop. Here, the activated Fibrinogen solution was pipetted to the bottom part of the minimal loading polymerization mold and a top plate was screwed to the flexible parts of the mold. The gel was allowed to polymerize for at least 2 h at 37 °C and 100 % relative humidity. The primary feature of this apparatus is the flexure design that allows the fibrin gel to contract against a “soft” wall (in the axial dimension) and against hydrophobic teflon in the lateral dimensions. This should, in principle, allow the material to relieve any residual stresses in the material present during polymerization compared to polymerizing between two glass plates at a fixed height.

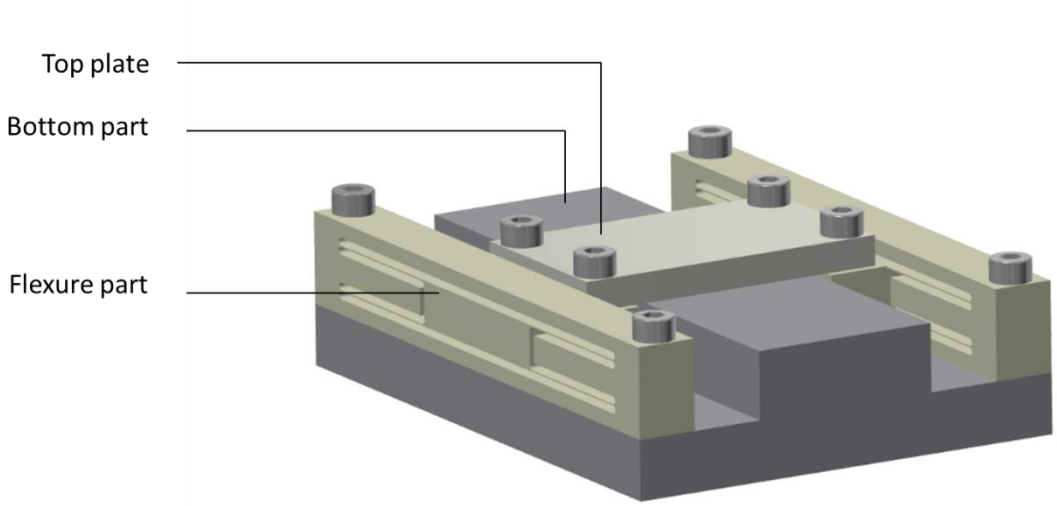


Figure 22 Minimal loading polymerization mold. The top plate and the bottom part of the mold are made of Teflon. The Top plate is fixed by four screws to highly flexible parts of mold. The flexible parts made out of PEEK allow the top plate to move during polymerization. Drawing from Marc-Jan van Zadel, MPIP Mainz.

### 3.7.2. Amino-silanization and glutaraldehyde activation of glass plates

The freely polymerized Fibrin gels had to be transferred and bound to glass plates for further experiments with BCARS. This was achieved by a chemical modification of the glass surface with amino-silanzation and glutaraldehyde activation. Coverslips (Menzel, 60x24x0.15mm) were cleaned in a mixture of Milli-Q water and Micre-90 from Sigma Aldrich (98/2) and sonicated for 30 minutes. After washing the glass plates with Milli-Q water for 10 minutes, the glass plates were dried in an oven for 1 h at 150 °C. The clean and dry glass plates were placed in a desiccator together with 0.5 mL of APTES in acetone (5 wt%) and vacuum was drawn to evaporate the APTES and create a sutured atmosphere. The plates can be stored at this step in a desiccator for 7 days. After silanization, the glass plates were soaked in a solution of Glutaraldehyde in Milli-Q water (5 wt%) for 10 minutes to activate the primary amines on APTES for protein crosslinking. This was followed by a washing step by rinsing several times with Milli-Q water. Afterward, the fibrin gel is sandwiched between two activated glass plates prior to shear loading. The mechanism of the glass plate modification is given in figure 23.

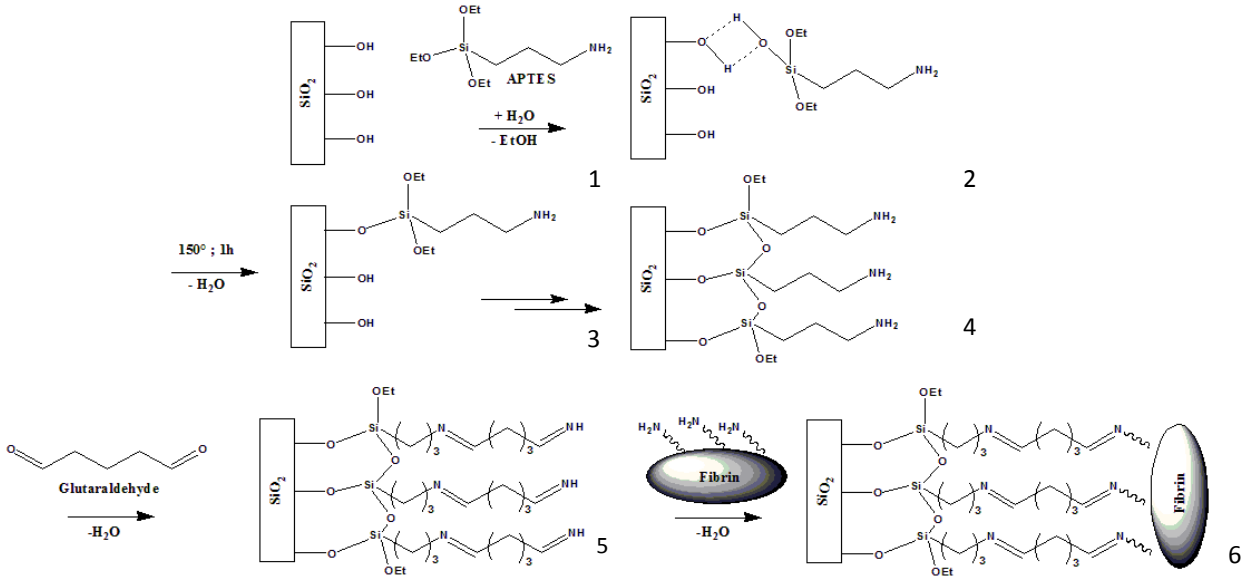


Figure 23 Mechanism of chemical glass plate modification. The exposure of APTES to water leads to hydrolysis of the ethoxy groups (1), yielding in an ethanol leaving group and a silanol (2). The silanol undergoes condensation reactions with alcohol groups and with each other (3). Resulting in amino-functionalized glass (4). The bifunctional glutaraldehyde binds surface amine groups via a hydrolysis reaction (5), thus functionalizing the surface with formyl groups that will bind surface-exposed lysines of any protein (6).

### 3.7.3. Finding the maximum shear strain prior to gel rupture

The minimal strain polymerization, post-fixation method and between-glass polymerization methods of sample preparation described above were tested to determine the strength of adhesion prior to rupture of the gels. The setup described in section 3.3. was used to apply a defined offset $\Delta x$ of the top glass plate. Height determination as described in section 3.7.5. defined the initial height, therefore the offset $\Delta x$ could be converted in shear strain according to ($\gamma = \Delta x / l$).

For all samples, a stepwise offset in a size 20 µm were applied, and the outer borders of the gels were checked via phase-contrast microscopy (Olympus IX-81, objective: 40x, NA = 0.8) to ensure that the gel was still attached to the coverslips. The total offset at the first visible point of detachment, defined as the point where the outer borders of the gel moved relative to the relaxed state, was used to calculate the maximum strain prior to rupture the fibrin gel. For both methods, 10 samples have been analyzed and shear strains were normalized to the initial sample height. The results are summarized in **Error! Not a valid bookmark self-reference.** table 2 and the averages are graphically displayed in figure 24 with error bars representing the standard deviation. The standard deviation is defined as:

$$\sigma = \sqrt{\frac{1}{N}\sum_{i=1}^{N}(x_1 - \bar{x})^2} \tag{7}$$

With sample size N and observed value $x_1$.

Table 2 Summarized results of the maximum shear strain supported by fibrin gels prior to rupture for gels directly polymerized between unmodified coverslips and gels attached post-polymerization to chemical modified coverslips.

| **Method** | **Maximum rupture strain [%]** | **Minimum rupture strain [%]** | **Average rupture strain [%]** | ***σ* [%]** |
|---|---|---|---|---|
| Polymerized between coverslips | 376.67 | 241.66 | 293.33 | 56.52 |
| Attached to chemically modified coverslips | 193.33 | 105.00 | 157.83 | 38.26 |

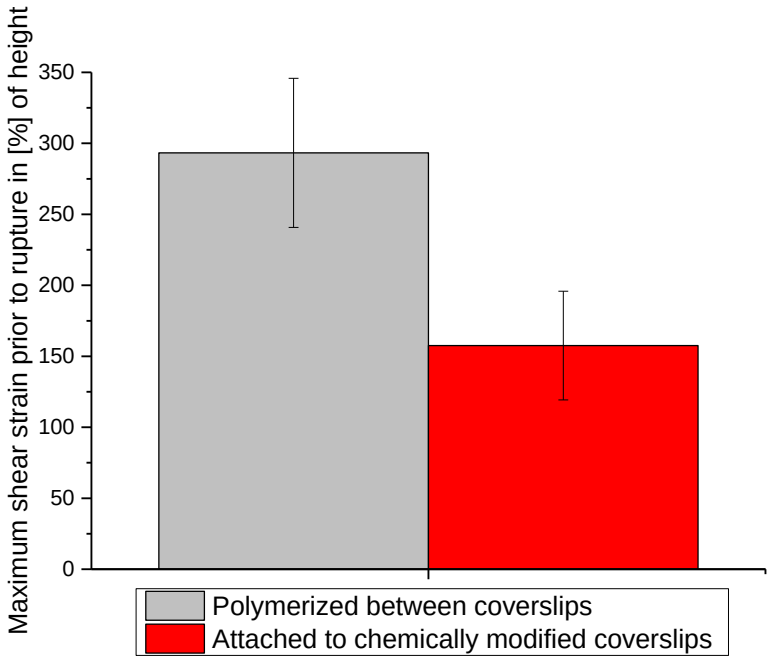


Figure 24 Diagrammatic representation of the maximum shear strain feasible to fibrin gels prior to rupture for directly polymerized between coverslips and subsequently attached to chemical modified coverslips after polymerization. Error bars representing the standard deviation.

The results show that the maximum shear strain that can be applied to a fibrin gel polymerized directly between two glass plates is clearly above the strain applicable to gels that were attached post-polymerization. The average shear strain for gels directly polymerized between coverslip is almost 2-fold greater than the rupture shear strain in post-polymerization attached gels. For both preparation methods, the variation in the attachment is well below the mean, always less than 25 %.

### 3.7.4. Manual shear cell loader with compensating normal force

Fibrin fibers experience forces when a shear strain is applied on the fibrin network. Not only do the fibrin fibers align in the direction of the shear strain, but they also exert forces on the network to resist the applied shear strain. These forces result in a negative normal force, which contracts the fibrin network. [67, 68] The manual shear cell (figure 25) was designed to circumvent the negative normal force resulting from the applied shear strain in order to isolate the contribution from shear alone. Therefore the top coverslip was held by a metal clamp connected to a flexure part (figure 26).

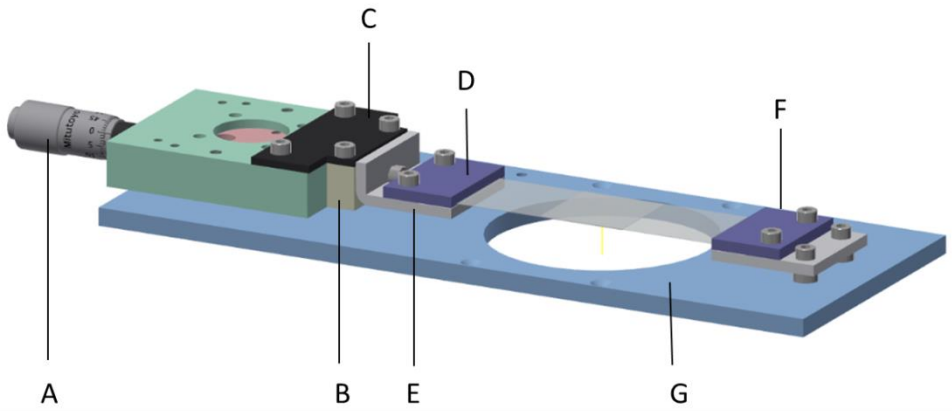


Figure 25 Schematic figure of the manual shear cell setup. (A) Micrometer for the displacement Δx of the top glass plate. (B) Flexible connector part to allow change in sample height when shear strain is applied and adapter plate for micrometer (C). (D) Metal clamp for holding the top glass plate supported by an L-formed plate (E). (F) Two metal plates holding the bottom glass plate on a fixed height. (G) Base plate for mounting on BCARS microscope. Drawing from Marc-Jan van Zadel, MPIP Mainz.

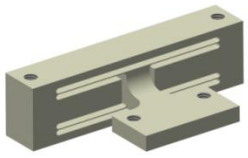

Figure 26 Flexure part made out of PEEK. Drawing from Marc-Jan van Zadel, MPIP Mainz.

Figure 25 shows the schematic design of the manual shear cell. The micrometer covers a range of 25 mm while having a resolution of 20 µm. The flexure part in figure 26 is similar to that used in the minimal loading polymerization mold (figure 22). The material for the flexure part Polyether Ketone (PEEK) was used as it is easy

to cut and has high flexibility, while being strong enough to resist the force of moving glass plates in the lateral dimension.

### 3.7.5. Fibrin height changes during shear loading

For every measurement made with the manual shear cell with the flexure part (figure 25), it was necessary to determine the initial height of the fibrin gel to calculate the applied shear strain. The piezo stage in the BCARS setup only allows a sample positioning in a range of 50 µm along the z direction. As all prepared gels had a larger thickness, online measurements of the height were not possible. Instead, samples' heights were determined before in the phase contrast imaging. The top and bottom glass plates were marked on the inner surfaces with a pen, and the absolute distance between the two surfaces i.e. the height of the gel, was determined by imaging. Every measurement at each spot was repeated five times, and an average height was calculated. If the two glass plates were sufficiently parallel, as judged by the height determination at the two different spots the sample was retained; otherwise, the sample was excluded from further characterization.

Since the flexure part allowed the fibrin gel to contract during shear deformation, it was important to quantify the height changes. Five fibrin samples of varying initial heights (631.93 µm – 991.98 µm) were tested. The lateral displacements $\Delta x$ were applied in 100 µm steps, and the gel height was measured after each deformation. Normalized data from the five gels were binned in 10 % strain steps and the average was plotted in figure 27.

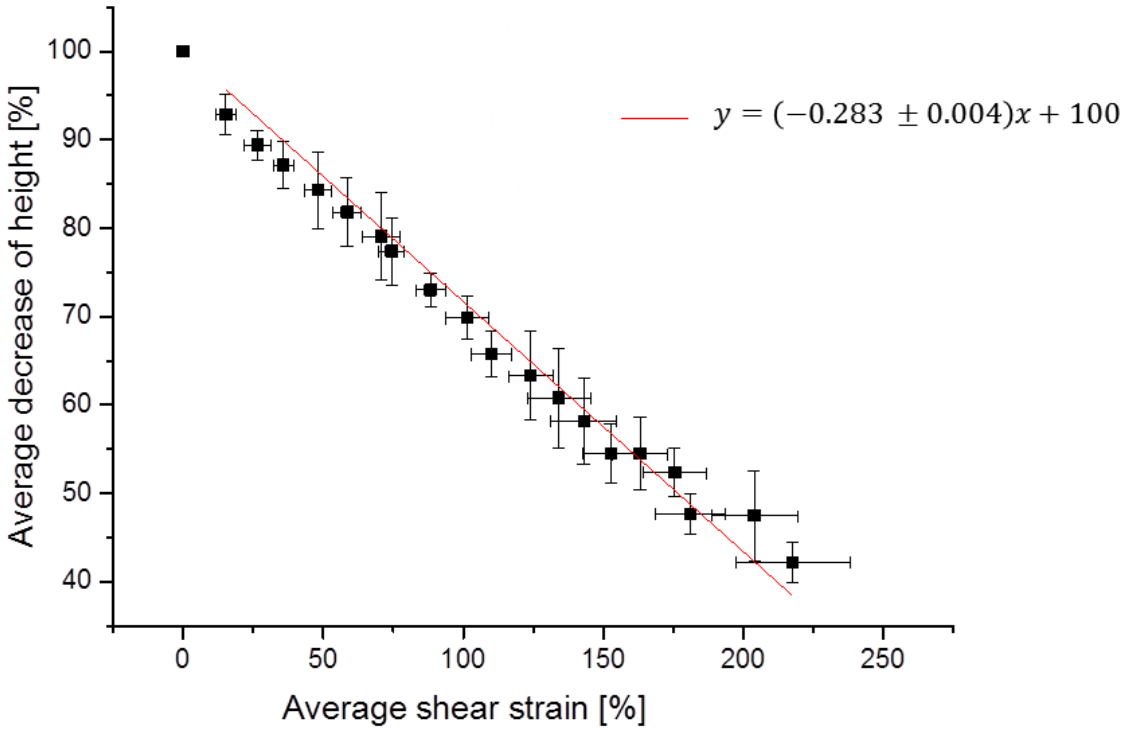


Figure 27 Height changes of fibrin gels as a function of applied shear strain. The normalized data points are binned in 10 % shear strain steps (as determined by the initial gel height), and the plot shows the average with error bars representing the standard deviation. The red plot indicates the resulting linear fit of the data.

The average normalized height from five gels followed a negative linear trend with increasing shear strains. Linear regression with a fixed y axis intersection at 100 % results in a slope of −0.283 ± 0.004 which can be used to calculate the height of fibrin gels under shear deformation.

# 4. Determining fiber orientation in strained fibrin gels by confocal microscopy

## 4.1. Fiber alignment under manual shear strain

The effect of manual shear strain on the orientation of fibrin fibers was studied by confocal microscopy as explained in 3.3. In these experiments, the gap size, or thickness of the gel was fixed for all deformations. Different shear strains were applied to a fluorescently labelled fibrin network and images of have been analyzed to determine fiber orientation.

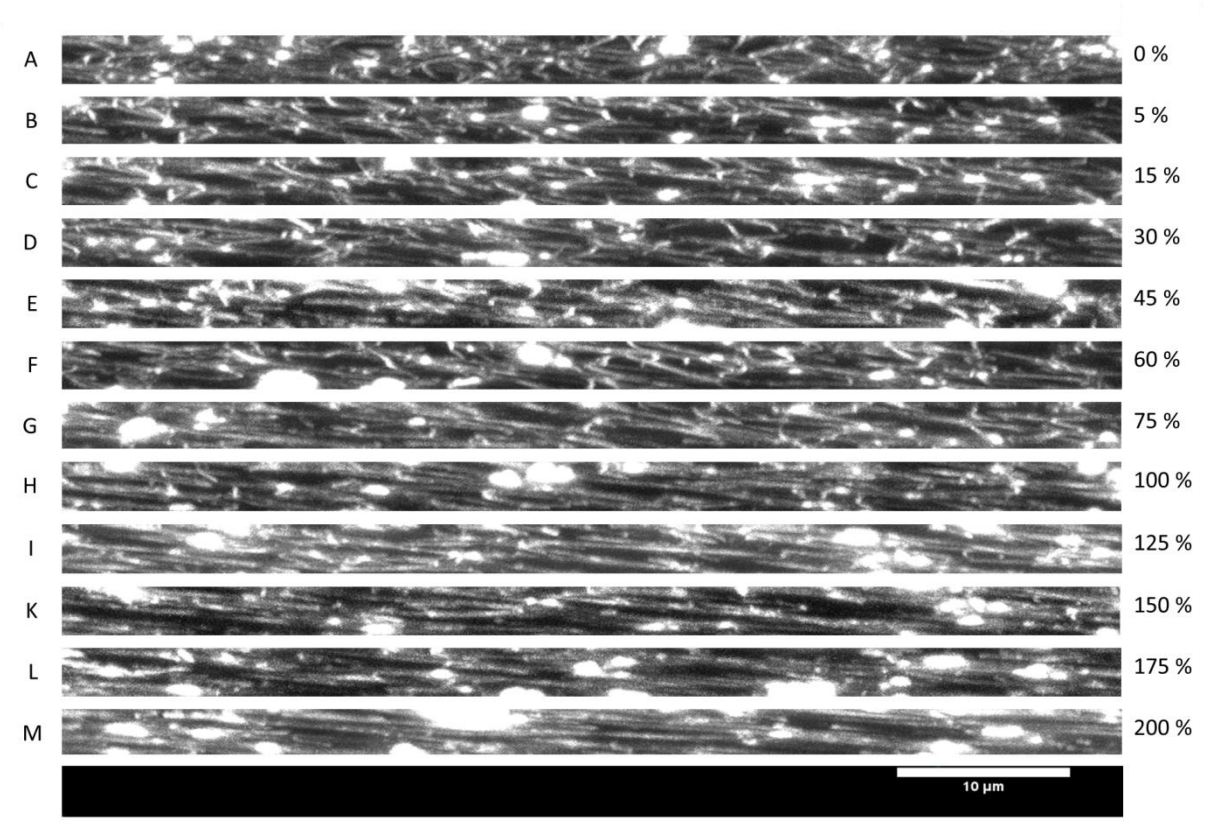


Figure 28 Maximum intensity projection in the XZ plane of a fibrin network. Every panel indicates another additional shear strain. Increasing shear strain from the top to the bottom panel shows increasing orientation of the fibrin fibers in the direction of applied shear strain.

The maximum intensity projections of the XZ planes depicted in figure 28 indicate that the fibers at 0 % strain (figure 28(A)) have an almost isotropic fiber orientation. As expected, the network gets more and more oriented along the shear axis with increasing shear strain (B-G). At 200 % additional shear strain (M) all fibers look fully aligned in an almost parallel orientation related to the coverslips.

To quantify this observation, the software tool SOAX was used to track the fibers in the maximum intensity projections of the XZ plane. SOAX is able to trace the fiber length and orientation out of image data of polymer networks. The images for different additional shear strains were analyzed according their distribution of azimuthal orientations of the fibers in the network. The resulting angles were binned in 5° steps and plotted as a histogram as shown in figures 29 – 31 for relaxed, 0 % "additional" shear strain, and 175 % additional shear strain, respectively. We use "additional" shear strain when discussing the shear amount because it is likely that an unknown amount of shear was imparted to the gel during sample preparation. Evidence for this conclusion is shown below in figure 29 and 30. Figure 29 shows the fiber orientation from SOAX for a relaxed fibrin network – polymerized between two glass slides and not mounted in the shear cell. The fibers are almost isotropically oriented, and no preferential orientation is found (figure 29). Figure 30 shows the fiber orientation for a 0 % additional strain sample, which clearly shows a preferential orientation near 0°. Figure 31 shows fiber orientation at 175 % additional strain, which shows a much more pronounced fiber orientation for reference.

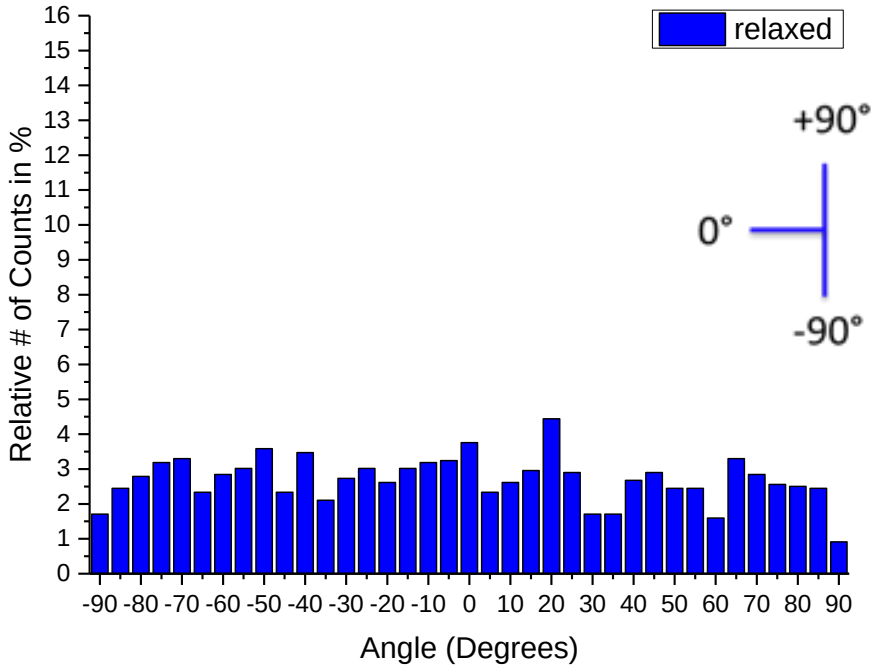


Figure 29 Histogram of azimuthal fiber orientation in a relaxed fibrin network with no shear strain applied determined by SOAX fiber tracking software. No preferential orientation is observable. Definition of angels (degrees) is given on the upper right of the image.

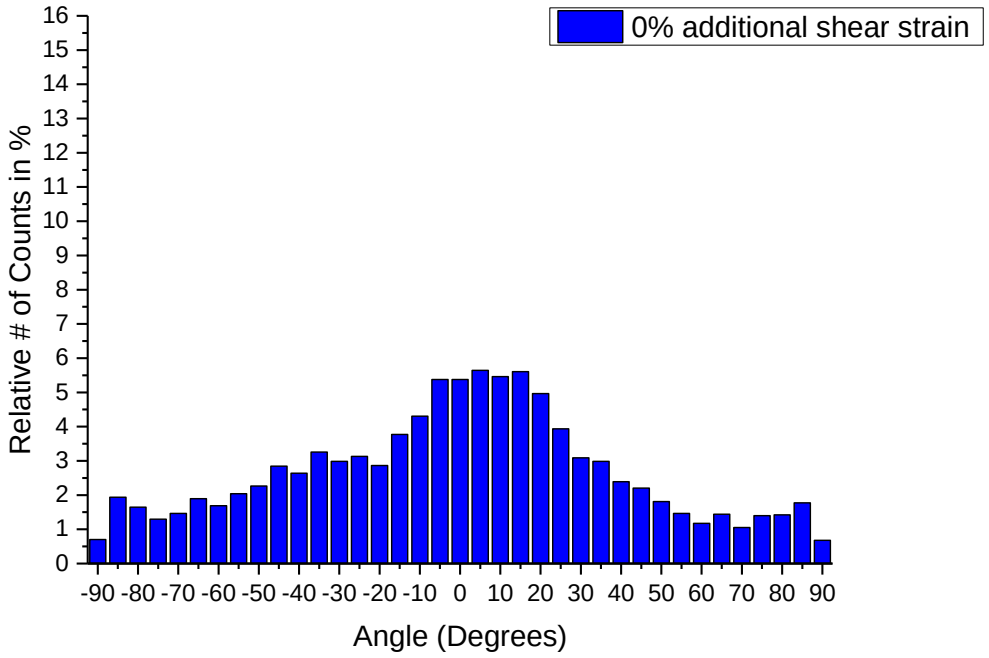


Figure 30 Histogram of azimuthal fiber orientation in fibrin with 0 % additional strain. An onset of fiber alignment parallel to the glass plates (0°) is observable.

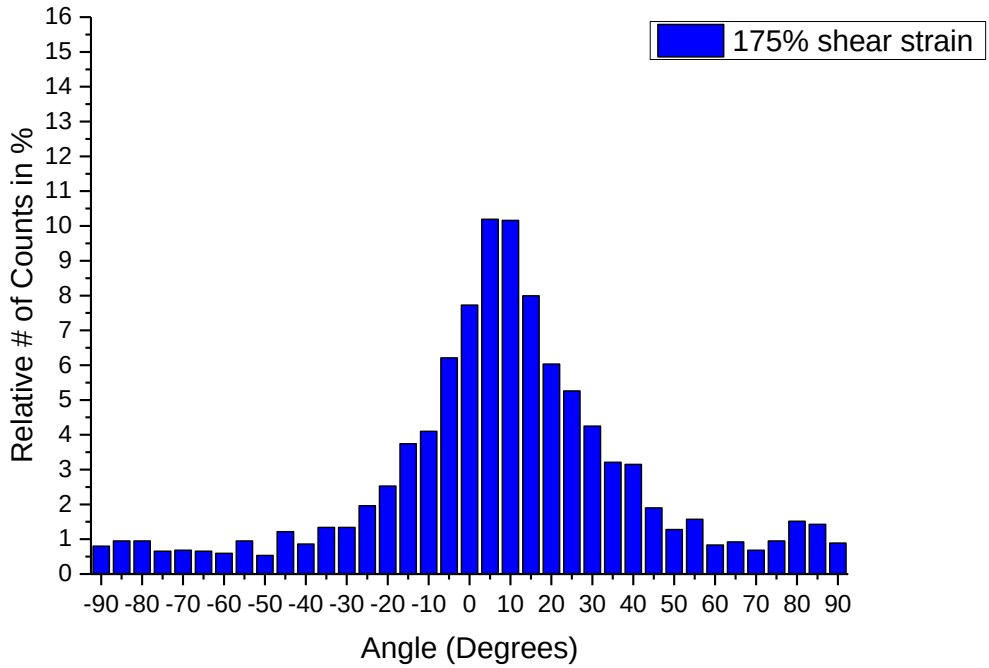


Figure 31 Histogram of polar fiber orientation in fibrin with 175 % additional strain. Most fibers are oriented along the shear axis, and the distribution is clearly narrower.

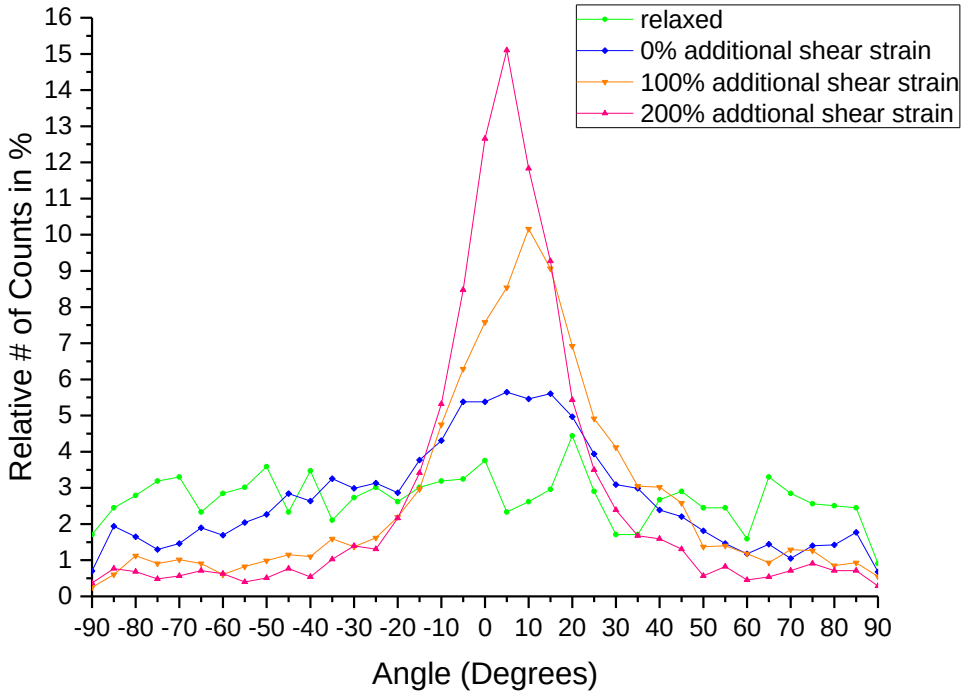


Figure 32 Diagram of polar fiber orientation of the XZ plane in a fibrin network with different shear strains applied. The relaxed network (green) shows no preferential orientation. The trend goes from 0 % additional shear strain (blue) where minimal fiber alignment is visible to 100 % additional shear strain (orange) with clearly visible preferable orientation and to 200 % additional shear strain (pink) with very strong orientation around the angles close to horizontal orientation.

Figure 32 shows the relative number of counts in % for the fiber orientation binned in 5° steps for relaxed, 0 %, 100 % and 200 % additional strain. Increasing fiber alignment starting from angles at ±20° to ±30°, with peak near 0° is seen with increasing strain. The relaxed fibrin gel (green) shows no obvious preferred orientation of the fibers in the network. After sample preparation and mounting (0 % additional strain), we observed an initial fiber alignment with preferable angles from -20° to 30° (figure 32, blue). Additional shear strains of 100 % (orange) show that the orientation of the fibers is getting more pronounced and narrow around the horizontal orientation of 0°. Doubling the shear strain up to 200 % (pink) enhance the effect of narrow orientation of fibers close to horizontal orientation additionally the maximum in relative number of count is found at 5° to 10°.

For a more quantitative analysis of the data, the angular distributions were fitted with a Gaussian function as shown in figure 33. The full width half maximum

(FWHM) is defined as the width of a curve at the point where the amplitude has half of the value compared to the maximum of the amplitude. The FWHM quantifies the degree of alignment of fibers within a sample. The maximum peak intensity indicates the amount of fibers being affected by the alignment as well as the alignment direction. Gaussian fits of all data sets were performed, and the FWHM and maximum peak amplitude are plotted in figure 34.

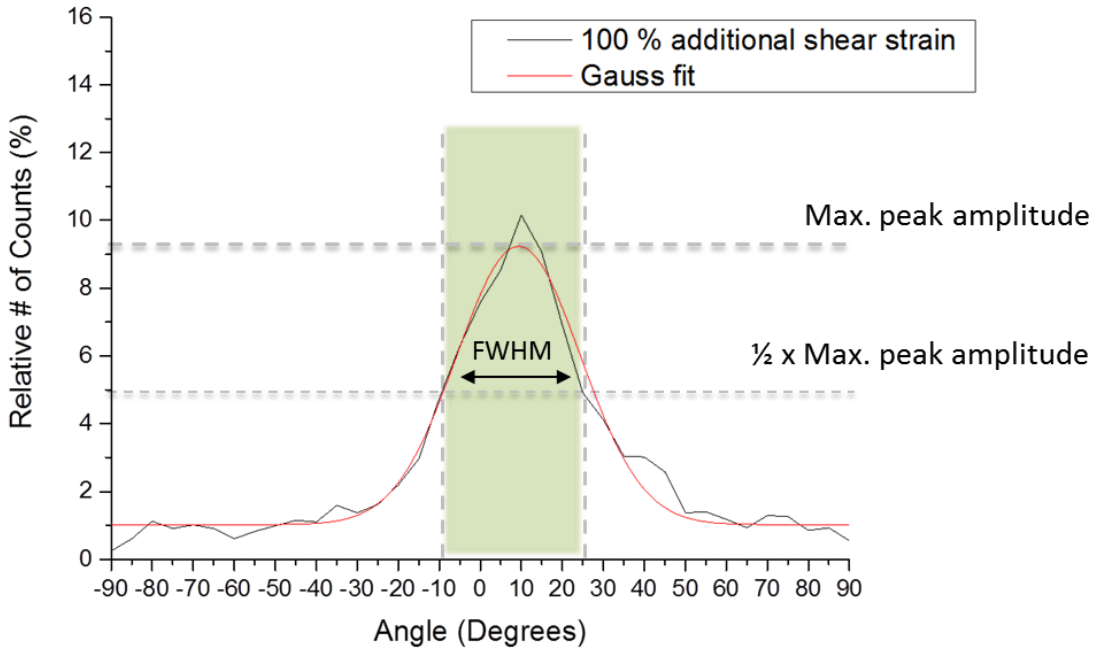


Figure 33 Gauss fit (red) delineated on the plot of the fiber orientation at 100 % additional shear strain (black).

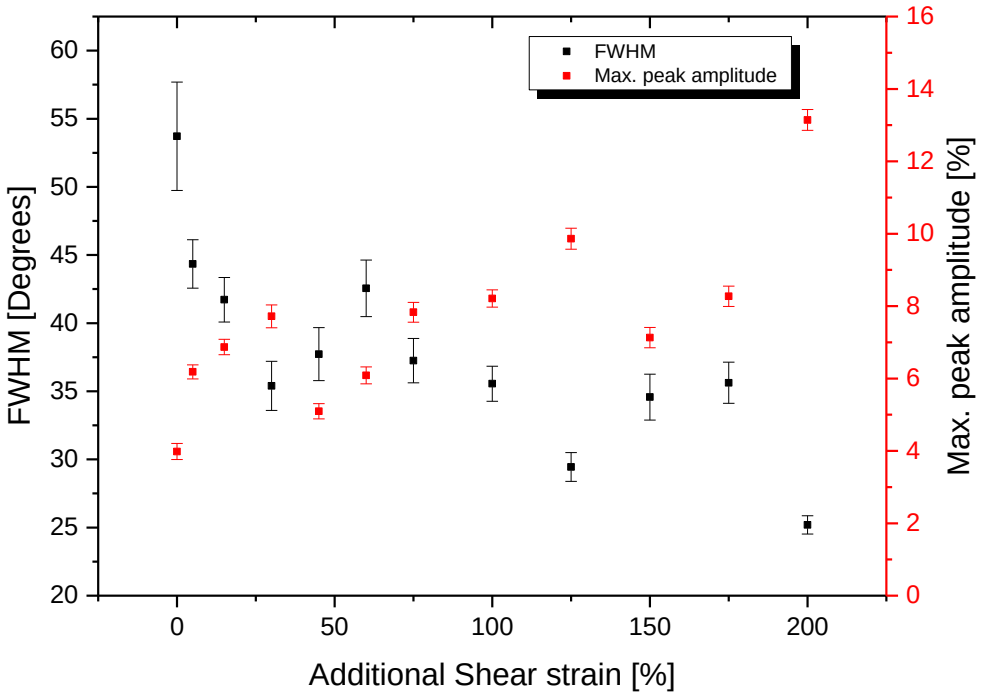


Figure 34 FWHM and the maximum peak amplitude of confocal shear strain measurements. FWHM represented by the black data points and the left y axis is showing an descending trend, contary to the increasing trend of the maximum peak amplitude represented by the red data points and the right y axis.With error bars representing the standard error of the mean.

With its maximum at 0 % strain, the FWHM followed a descending trend with some exceptions. From 0 % to 30 % shear strain, the FWHM decreased, however for 40 % and 60 % of shear stain the FWHM is rising up to a level which is above the FWHM of 5 % strain. At 75 % of strain the descending trend appeared again until shear strains of 125 %. The values for 150 % and 175 % of shear strain were similar in a level approximately at the FWHM for 100 % shear. The minimum for the FWHM was found for the maximum deformation of 200 % strain.

The trend for the maximum peak amplitude is shown in figure 34 by the red squares with its y axis at the right side, is contrasting the trend of the FWHM. The values ascended with the same expectations of 40 %, 60 %, 150% and 175 % of shear strain. The values for 150 % and 175 % of shear strain commuted in an approximate level to the value for 100 % shear strain once more. The increasing trend, for the

maximum, along with the decreasing FWHM is what is expected for a system undergoing more alignment with strain.

Besides the change in orientation along the XZ plane, the directionality in XY was checked for different degrees of shear deformation. To analyze the fiber orientation in the XY plane, one image from a z-stack (0.25 µm spacing) taken from the sample was used. For 0 %, 100 % and 200 % shear strain, a single z-plane was analyzed for fiber orientation with SOAX. The relative number of counts in % have been binned in 5° step size and plotted in figure 35.

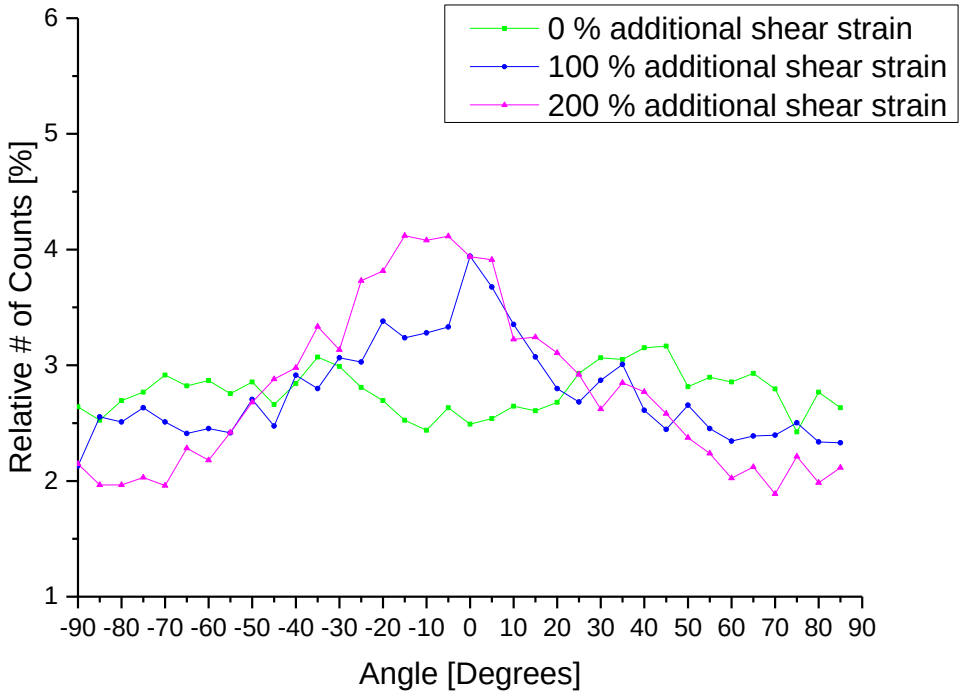


Figure 35 Diagram of azimuthal fiber orientation of the XY plane in a fibrin network for a relaxed gel and for a gel with different shear strains applied. Network with 0 % additional shear strain (green) shows no preferable orientation. Minimal alignment of fibers for 100 % additional strain (blue) for angles between -40 ° to +25 ° can be assigned. For 200 % additional shear strain (pink) distinct preferred orientation with maxima for angels from -25° to +10° is visible.

Figure 35 shows the fiber orientation in the XY plane for representative additional strains of 0 %, 100 % and 200 %. For 0 % additional shear strain (green) no visible fiber alignment is observable; moreover, angles between −25° and +20 ° are slightly underrepresented. Minimal alignment of fibers for 100 % additional strain (blue) for angles between −40 ° and +25 ° can be detected. Distinct preferred orientation is

only visible for 200 % additional shear strain (pink) with maxima for angels from −25° to +10°.

The fiber orientation in the XZ plane seemed to be consistent with the results for the XY plane as it showed the onset of a preferred orientation when a strain was applied. The disconnections for the descending trend of FWHM and the ascent trend for the maximum peak amplitude for additional applied shear strains of 40 %, 60 %, 150 % and 175 % might have been caused by the limited quality of the resliced images although visual inspections did not show any obvious difference in the quality compared to the images following the trend after analysis via SOAX. Moreover, this result could be interpreted that applied strains on the network are not acting homogeneously all over the sample and that some areas experience more strain then others, which is clearly possible based on microscopy data from other studies.[33]

Fiber orientation in XY axis indicates that clear alignment of fibers in this plane only appears at very large additional strains of 200 %. This is in agreement with the predicted behavior of a network under shear strain since there is no force acting directly on the fibers orientated in the XY plane like under tension.

## 4.2. Fiber alignment under automated shear strain

In the following experiments, an automated shear cell was used wherein the gap size (thickness of the gel) was different for every measurement, but it was possible to apply shear to the fibrin gel directly on the microscope. This allowed us to measure the same area throughout the shearing process as opposed to the different areas in the manual shear experiments described above. The effect of shear strain on the orientation of fibrin fibers was studied by confocal microscopy as explained in 3.4.

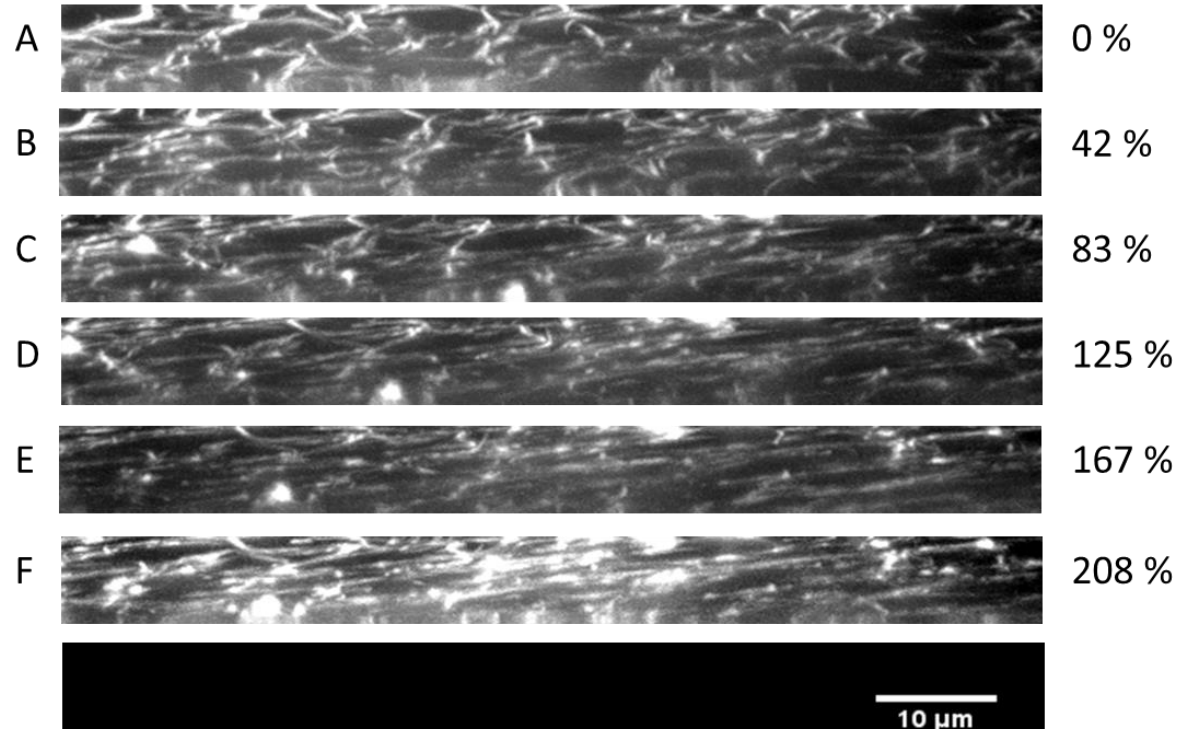


Figure 36 Maximum intensity projections in the XZ plane of a fibrin network for increasing shear strain from top to bottom. Related shear strains are summarized on the right side. The fibers get more oriented along the direction of shear with larger applied strain.

The maximum intensity projections of the XZ planes depicted in figure 36 indicate that the fibers at 0 % shear strain (A) have an equal distribution. From 42 % (B) to 167 % (E) shear strain the images show an increasing orientation of the fibers in the direction of applied strain. The last images for 208 % shear strain (F) does not show any obvious further increase of the fiber alignment compared to image representing 167 % shear strain. Histograms of azimuthal angle binned in 5° steps from SOAX fiber tracking are plotted in figure 37.

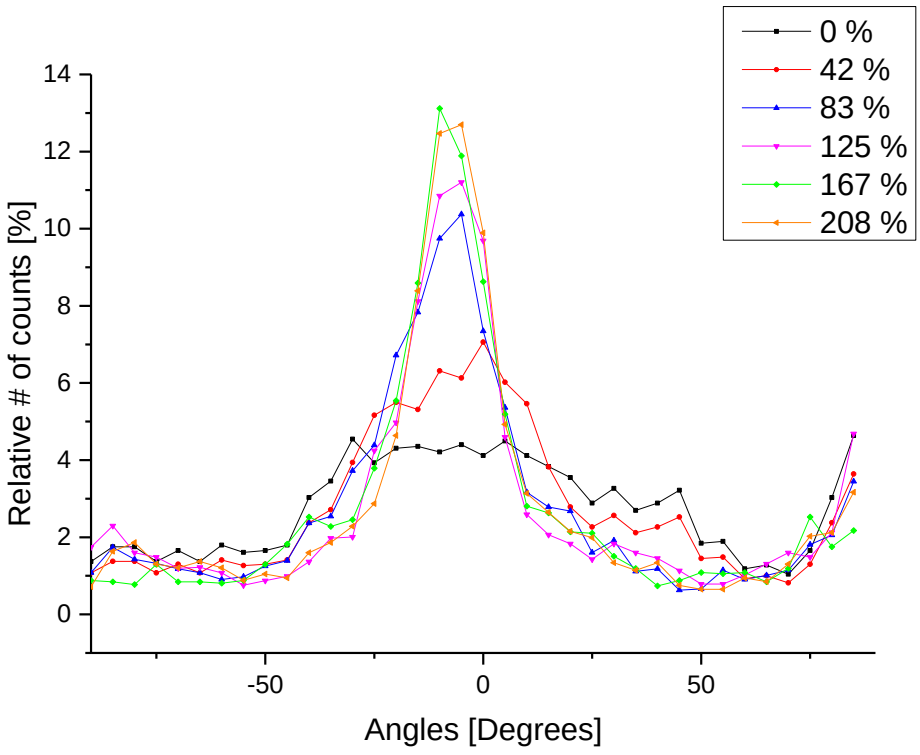


Figure 37 Azimuthal fiber orientations in the XZ plane for relaxed and sheared samples. The relaxed network (black) shows minimal preferable orientation between -30° to + 50°. The trend goes from 42% shear strain (red) where arising fiber alignment is visible to 125 % shear strain (pink) with clearly visible preferable orientation and to 208 % additional shear strain (orange) with very strong orientation around the angles close to horizontal orientation.

Figure 37 shows the relative number of counts in % for the fiber orientation binned in 5° steps. The orientation of a relaxed gel (black) showed some minor fiber alignment for orientations between -30° to +50°. Shear strain of 42 % (red) shows arising orientation for angles −30° to +25°. This trend continuous until a shear strain of 125 % (pink) is reached. For 167 % shear strain (green) the maximum in relative number of counts at −10° to −5° for all measurements is observable, the relative number of counts for 208 % shear strain (orange) is slightly below these number

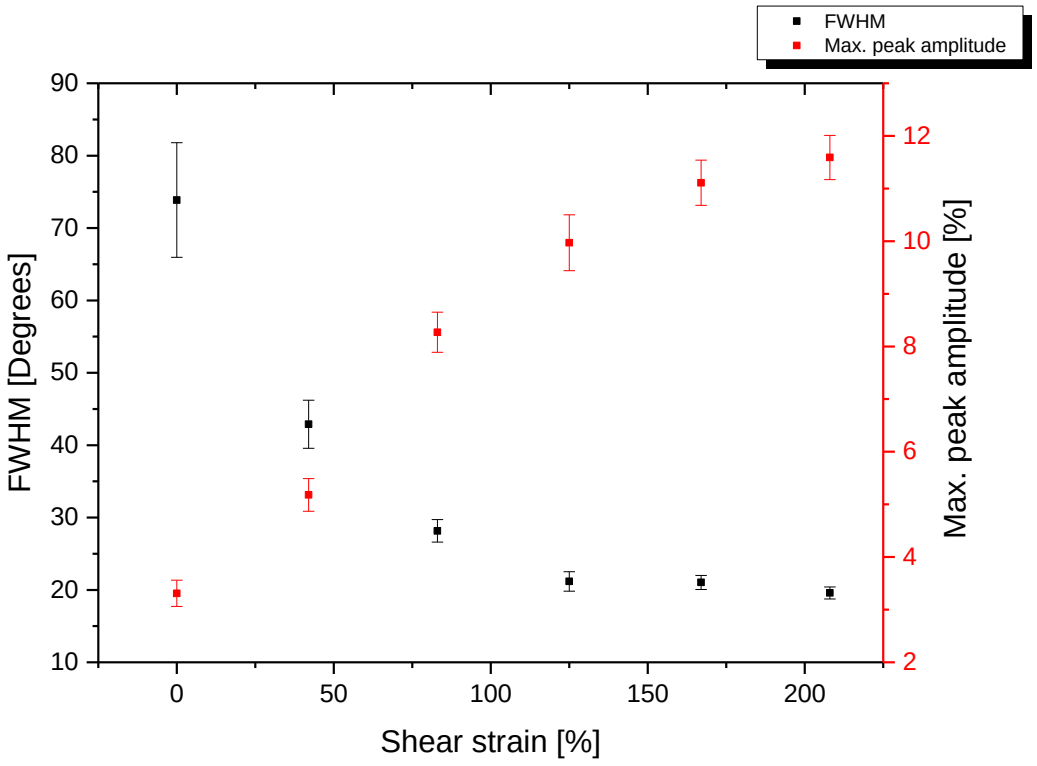


Figure 38 FWHM and the maximum peak amplitude of the automated confocal shear strain measurements. FWHM represented by the black data points and the left y axis show a descending trend, contrary to the increasing trend of the maximum peak amplitude represented by the red data pints and the right y axis. Error bars are the standard error of the mean.

Similar Gaussian fitting of the data in figure 38 was done and the FWHM and amplitude are shown in figure 38. The FWHM in degrees at different addition strains has a maximum at 0 % additional strain it is following a descending trend. The trend for the maximum peak amplitude represented in figure 39 is shown by the red squares with right y axis and is contrasting the trend of the FWHM. Both trends are similar to that seen for the manual shear fiber tracking. The automated shear strain measurement shows that the fiber orientation in the XZ plane is consistent with increasing strain as it shows preferred orientation in the direction of applied strain. Compared to the measurement with the manual shear cell, where all images have been taken in different areas within one sample, the analyzed images in this section are from the same area of the fibrin gel. The FWHM of the automated confocal shear strain measurements and manual confocal shear strain measurements are plotted in figure 39. The maximum peak amplitude of the automated confocal shear strain

measurements and manual confocal shear strain measurements are plotted in figure 40.

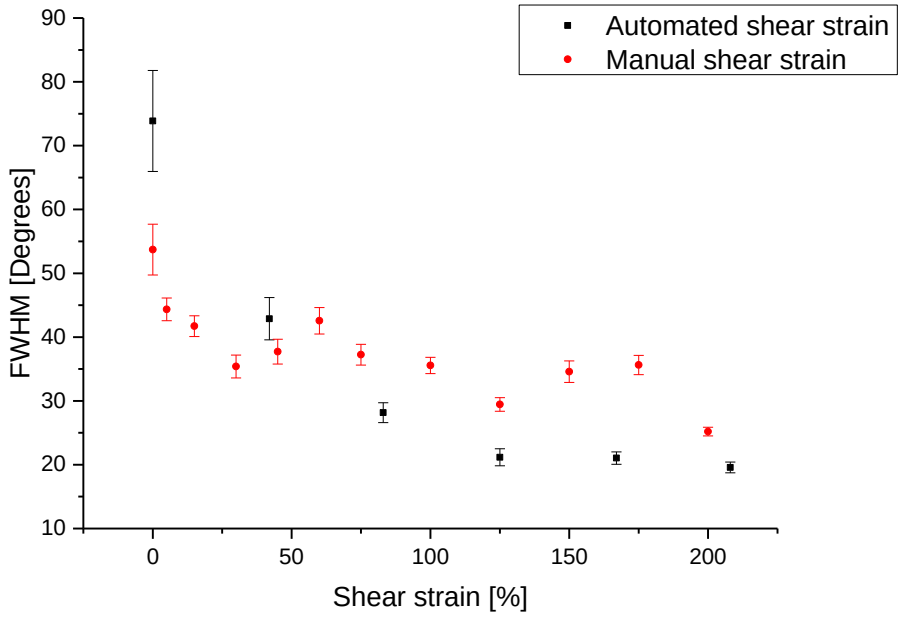


Figure 39 FWHM of the automated confocal shear strain measurements (black) and manual confocal shear strain measurements (red). FWHM show a descending trend for increasing shear strains. Error bars are the standard error of the mean.

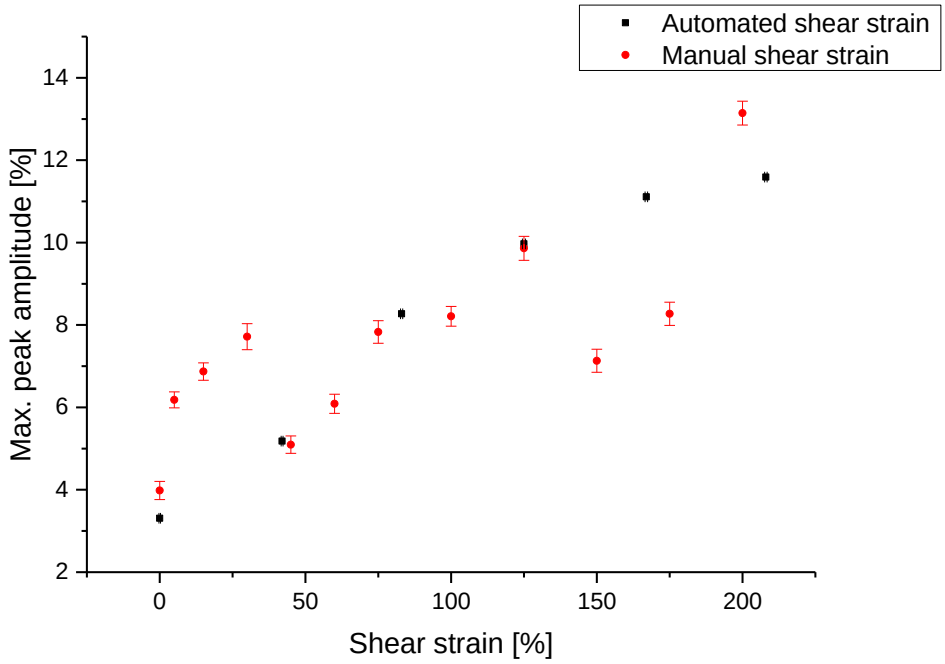


Figure 40 Maximum peak amplitude of the automated confocal shear strain measurements (black) and manual confocal shear strain measurements (red). Maximum peak amplitude shows an increasing trend for increasing shear strains. Error bars are the standard error of the mean.

The comparison of the FWHM and the maximum peak amplitude for both methods show that the followed trend is similar for both methods, even showing reasonable quantitative agreement. The values for the maximum peak amplitude for both methods are comparable for shear strains up to 125 %. The maximum peak amplitudes for the manual measurement at 125 % and for the automated measurement for 167 % are not comparable. For the manual measurement the maximum peak amplitude is on the level of only 83 % shear strain of the automated measurement, indicating that the measured area experienced less strain then for example the area measured for 125 % shear strain. In contrast, the value of the maximum peak amplitude for 200 % shear strain in the manual measurement is higher than for 208 % shear strain measured in the automated fashion. The comparison of the FWHM of both methods does show the same outliers for the manual measurement.

Comprehensively it can be said that the confocal microscopy images of fibrin under shear strain showed fiber alignment with increasing strains as expected. The measurement set with the manual shear cell indicates that applied strains on the network are not acting homogeneously all over the sample. The results observed with the automated shear cell are only followed a distinct trend, which was similar to the manual shear cell, though only for one out of four automated measurement sets. For the other three measurement sets no fiber alignment was observable, suggesting that a heterogeneous distribution of shear strains exists within a fibrin network. The heterogeneity is accentuated in the automated shear cell analysis because only a single field-of-view is investigated per shearing experiment whereas the manual shear experiments randomly sampled different areas in the gel at each shear strain.

## 4.3. Tensile strain measurement

In addition to shear deformation, similar experiments on fiber alignment were performed with tensile strain. To do so, fibrin gels were imaged in confocal microscopy for different tensile strains. The effect of tensile strain on the orientation of fibrin fibers was studied by confocal microscopy as explained in 3.5.

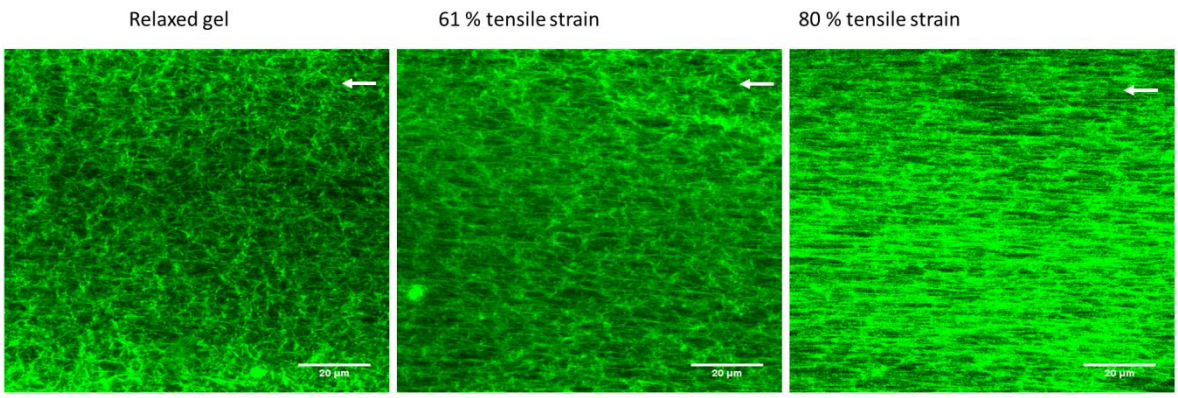


Figure 41Confocal images of a fibrin network in a relaxed gel and tensile strains of 61 % and 80 % applied. The relaxed gel shows no fiber alignment while tensile strains of 61 % and 80 % result in an orientation of the network along the direction of applied strain.

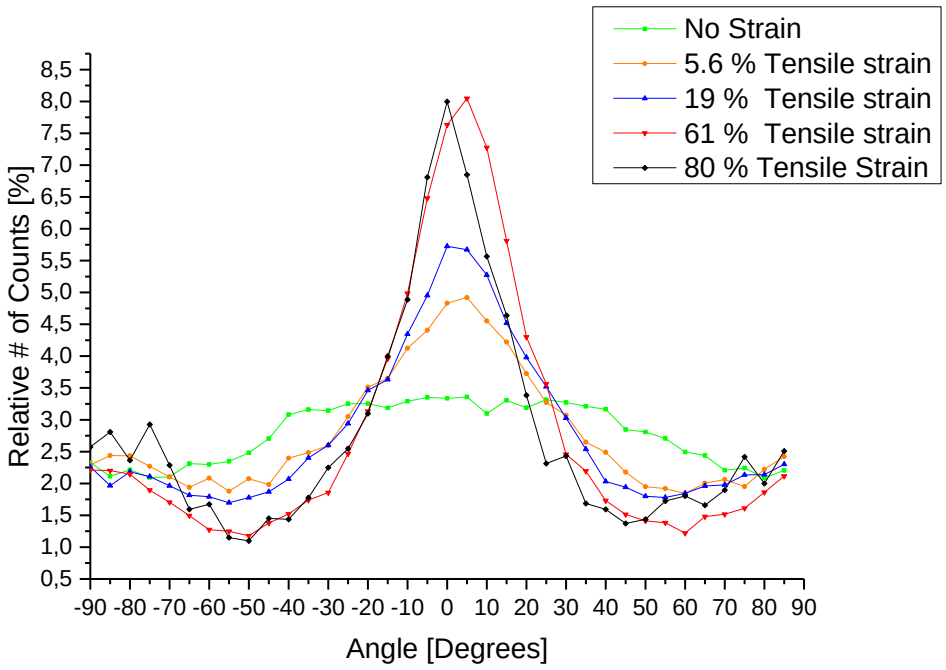


Figure 42 Diagram of azimuthal fiber orientation of the XY plane in a fibrin network for a relaxed gel with no tensile strain applied and for different strains applied on the gel. The relaxed network (green) shows no preferable orientation. The trend goes from 5.6 % tensile strain (orange) where arising fiber alignment is visible to 19 % tensile strain (orange) to with clearly visible increasing alignment. Finding its maximum for tensile strains of 61 % (red) with the maximum peak amplitude at orientations from 5°-10° what is then shifted for tensile strains of 80 % (black) to the fully horizontal orientation of 0°-5°.

Similar to the analysis for shear microscopy experiments, the relative numbers of counts resulting from the SOAX analysis in % are binned in 5° steps and shown in figure 42. For the relaxed sample (green), the relative number of counts is minimally

elevated for orientations between −45° to +45°. In contrast to shear deformation, a rapid increase in orientation between −45° to +45° can already be observed for small tensile strains of 5.6 % (orange).The orientation further increases for strains of 19 % (blue), 61 % (red) and 80 % (black). When comparing the plots representing 61 % tensile strain (red) and 80 % tensile strain (black), one finds that the fibers become more ordered while the relative number of counts stays constant. The maximum relative number of counts is also shifting from +5° to +10° into 0° to +5°. It can be concluded, that at 80 % tensile strain, a substantial number of fibers within the fibrin network are orientated in the direction of applied strain.

The value in the relative number of counts at angles of −70° to −90 ° and +70° to +90° can be determined as the baseline amount of fibers that never become aligned with increasing strain. The percentage of fibers oriented at these angles does not change with applied tensile strain, and these values stay relatively stable. On the contrary, the amount of counts for the orientation of −65° to −30° and +30° to +60° is decreasing. This can be interpreted as only fibers that are somewhat pre-aligned in the direction of strain eventually align in the direction of applied tensile strain, while fibers of orthogonal orientation to the strain do not perceive preferential alignment in the direction of strain.

Gaussian fits on all data sets were calculated and the FWHM and the maximum peak amplitude for the relative number of count binned in 5° steps of fiber orientation. The resulting values are plotted in figure 43.

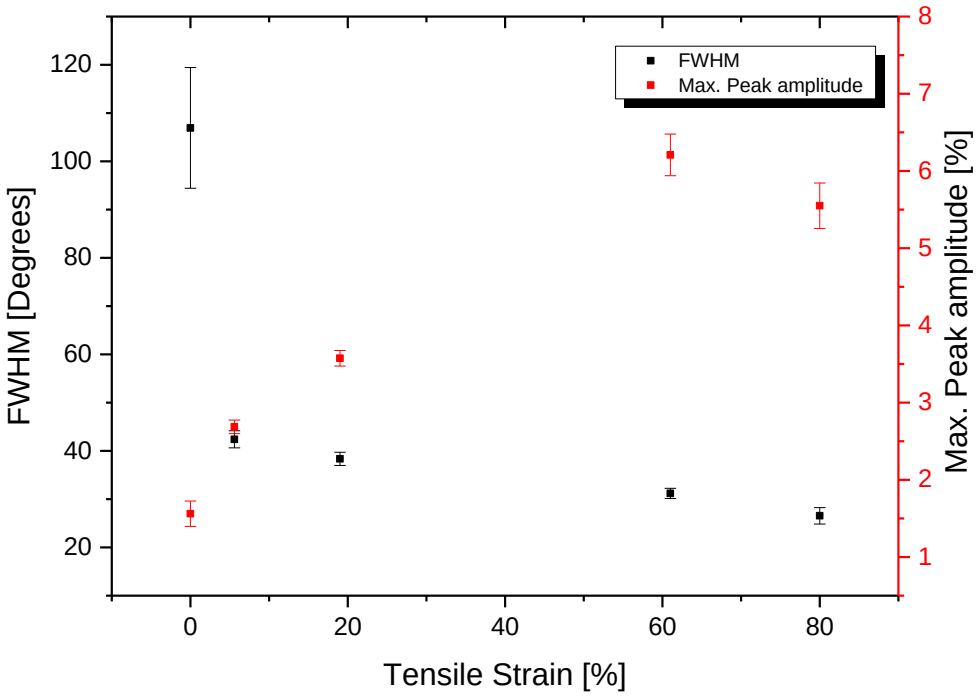


Figure 43 FWHM and the maximum peak amplitude of confocal tensile strain measurements. FWHM represented by the black data points and the left y axis is showing an descending trend, contary to the increasing trend of the maximum peak amplitude represented by the red data point and the right y axis. Error bars represent the standard error of the mean.

The FWHM of the Gaussian distributions of fibers in the fibrin network at different tensile strains is shown by the black squares and the left y axis in Figure 43. With its maximum for the relaxed gel, it is quickly descends from 0 % to 5.6 % of tensile strain followed by a much weaker linear downtrend with increasing tension. The trend for the maximum peak amplitude represented in figure 43 by the red squares with its y axis at the right side, is contrasting the trend of the FWHM. The values increased apparently linear for tensile strains up to 61 %. The values in the maximum peak amplitude for 61 % and 80 % tensile strain are comparable within the related standard error of mean. Therefore the amount of fibers being affected by the alignment already reaches its maximum at ~ 60 % of tensile strain, with an increasing alignment in the direction of strain from +5° to +10° for 61 % tensile strain to +0°to +5° for 80 % tensile strain.

As the fiber orientation of fibrin networks is influenced in the direction of strain, an analysis of the XY plane for tensile strains is conclusive. Compared with the analysis for shear strain measurements where the stacked images were acquired with a resolution of 250 nm along the z-axis and the re-slicing of the z-stacks results in a lower image quality in the analyzed section view, the analysis of the tensile strain measurements has a higher accuracy. This can be verified by the good image quality shown in figure 41 and the fiber orientation related to the predicted behavior of fibrin networks under tensile strain.

Below we show the comparison for the degree of alignment (FWHM) of shear and tensile in figure 44 (A) and for the amount of fibers being affected by the alignment (maximum peak amplitude) in figure 44 (B), normalized to the FWHM/maximum peak amplitude of the relaxed gel.

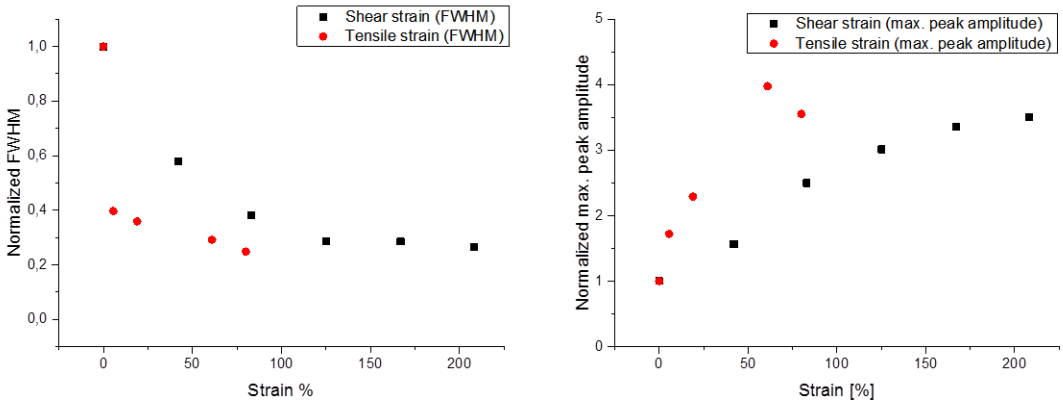


Figure 44 Normalized FWHM of shear (black) and tensile (red) measurements (A) and normalized maximum peak amplitude of shear (black) and tensile (red) measurements (B). Normalized to the FWHM/maximum peak amplitude of the relaxed gel.

The FWHM for tensile strains is rapidly decreasing from 0 % strains to strains of only 5.6 %. This level of fiber alignment is reached in shear strains measurements at strains of around 83 % shear strain. The level of fiber alignment for 80 % tensile strain is comparable with the level of 208 % shear strain. The maximum peak amplitude shows that next to the higher degree of alignment of fibers for tensile strain, the amount of fibers being affected is acting on a more sensitive way then for shear strains. While the maximum is reached for tensile strains of 60 % to 80 % the increasing trend for shear strains last for strains up to 208 %.

Taken together, these measurements demonstrate that while for tensile strain fiber orientation along the direction of load occurs already for small deformation, a much larger shear strain is required for a similar network alignment. It is known that the initial, linear network stiffness at low shear strains reflects thermal fluctuations of the fibers. While it is predicted, that the elasticity at higher stress is dominated by changes at molecular level. The resulting fiber orientations under shear and tensile strains indicate that the network morphology at the mechanics on the single fiber level differ, for shear and tensile deformations. These results emphasize the nature of the two different kinds of strains.

In the study from Onck and coworkers, two-dimensional network simulations have been used to explain the strain stiffening of filamentous protein networks under shear strain. The basic idea of these models, shown schematically in figure 45, is that stiff fibers are easier to bend than to stretch. As strain increases and the filaments align more and more in the strain direction, a transition occurs from bending to stretching, which leads to increased stiffness at increased strains. This model predicts that at strains where the samples stiffen, changes in the protein structure can be expected.[70]

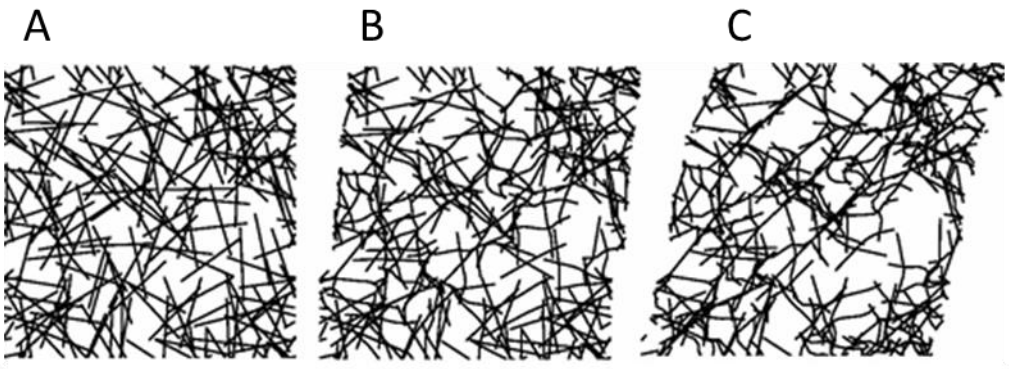


Figure 45 Network configuration for an initial network (A). Stiff filaments deform initially by bending at small strains (B) and then by stretching at larger strains (C) when the fibers align in shear.[70]

Taken together, it can be assumed that a substantially higher shear strain is required to cause molecular unfolding of protein structure compared to tensile strain.

# 5. BCARS measurements of fibrin under shear strain

In previous research on fibrin under tensile deformation, the Parekh lab BCARS measurements have been used to quantify mechanically induced secondary structural changes of fibrin gels under tensile strain. It was shown that the amount of α-helical structure decreased with increasing deformation and increasing contribution from β-sheet structure. Consistent with Litvinov et al., it was shown that the amount of β-sheet increases when the samples are stretched to 90 % tensile strain.[16] Figure 46 (reprinted from ref. 16) shows the secondary structure content of fibrin samples under increasing tensional strains.

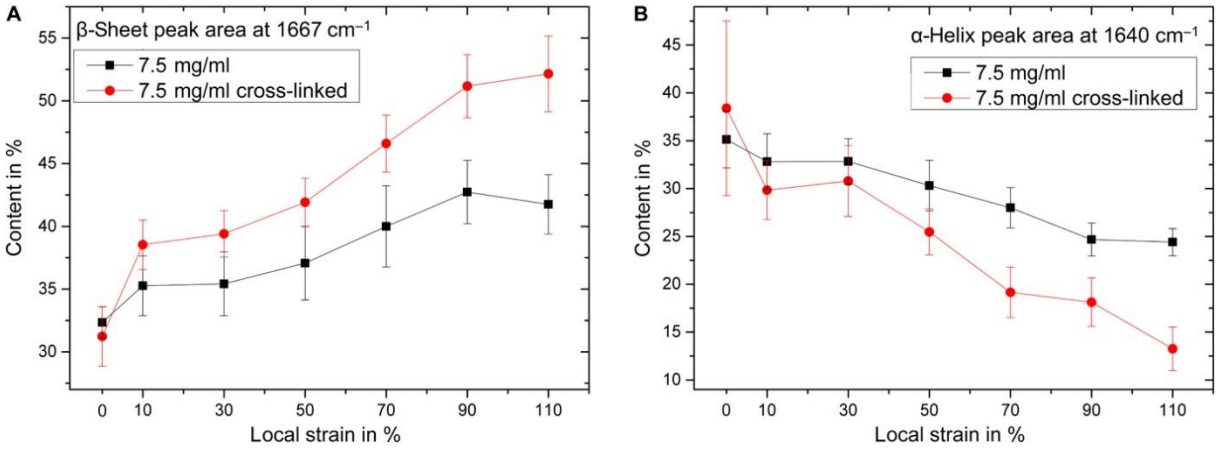


Figure 46 Secondary structure content of fibrin samples under increasing tensional strains. Increasing β-sheet content (A) for strains up to 90 % for partially cross linked gels (black) and cross-linked gels (red). Decreasing α-helical content (B) for strains up to 90 % for partially cross linked gels (black) and cross-linked gels (red).[16]

To identify the molecular changes under shear strains and further quantification, complementary to the secondary structural changes of fibrin gels under tensile strain, the need of high shear strains is presumable. Therefore the development of a method that makes BCARS spectroscopy of fibrin gels under high shear strain possible is mandatory.

In the following chapter, broadband CARS measurements are used to investigate the secondary structure of fibrin gels under shear strain. The most prominent vibrational band of a protein Raman spectrum is the $CH_3$-peak. It therefore acts as a criterion on the overall CARS intensity during alignment and without a sufficient intensity the many-fold weaker amide I region will be hard to analyze. Figure 47

shows a typical raw BCARS spectrum of an fibrin sample (black) with the $CH_3$ vibrational band located at 2935 $cm^{-1}$and the vibrational band of water at 3100 $cm^{-1}$. The CARS spectrum as acquired by the spectrograph consists of a nonresonant and a resonant contribution resulting in a highly distorted spectrum. As only the resonant part depends on the nonlinear susceptibility of the sample, and thereby contains the chemical information of interest, both need to be separated by employing the modified Kramer-Kronig relation.[71] After phase-retrieval and background subtraction, the Raman-like spectrum (blue) can be further analyzed. The fingerprint region (800 to 1800 $cm^{-1}$) contains information about molecular vibrations present in biological specimens including the amide I band (1570 to 1700 $cm^{-1}$) which is sensitive to the secondary structure.[72]

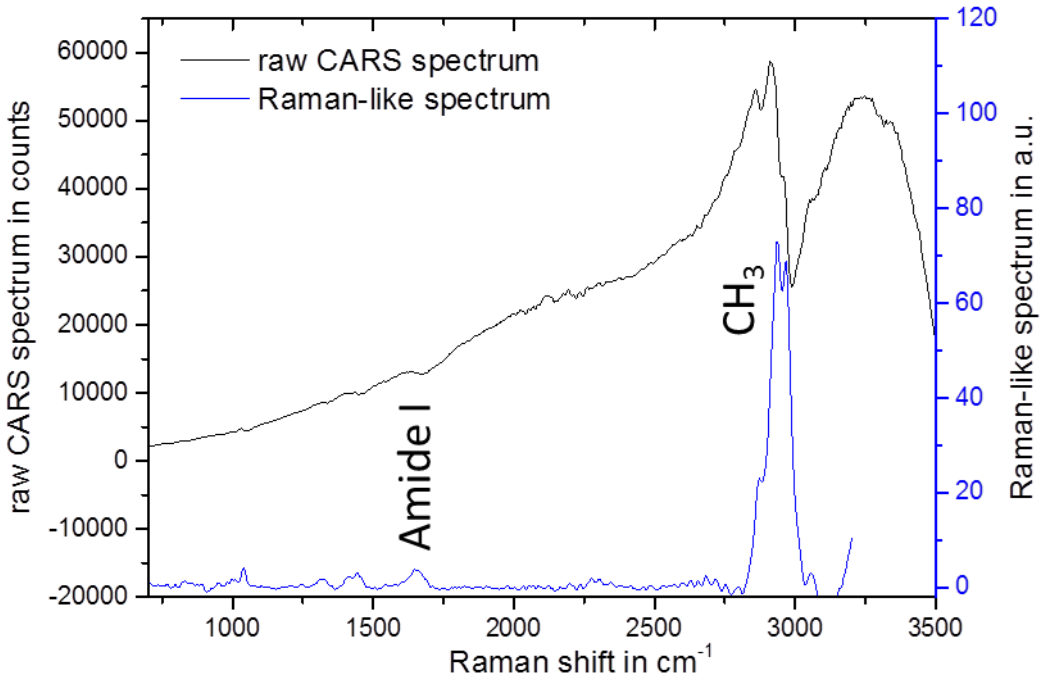


Figure 47 Raw BCARS spectrum (black) and Raman-like spectrum after phase retrieval and background processing (blue) of a fibrin sample. In the Raman-like spectrum, the amide I region (1570 to 1700 $cm^{-1}$) can be analyzed according to the contribution of secondary structure in the protein. The $CH_3$ vibrational band (2935 $cm^{-1}$) is visible in both the raw CARS spectrum (shifted towards lower wavenumbers) and in the Raman-like spectrum after phase retrieval (correct peak positions).

A detailed Raman-like spectrum of the fingerprint region after phase retrieval is plotted in figure 48. Next to the amide I region (1570 to 1700 $cm^{-1}$) the vibrational

modes for phenylalanine at 1000 $cm^{-1}$, aromatic C-O and C-N at 1200 $cm^{-1}$, the amide III region from 1200 to 1300 $cm^{-1}$, CH bending at 1342 $cm^{-1}$, $CH_2$ scissoring at 1441 $cm^{-1}$, the amide II region from 1480 to 1575 $cm^{-1}$ , and the amide I region from 1570 to 1700 $cm^{-1}$can be assigned for proteins.[56]

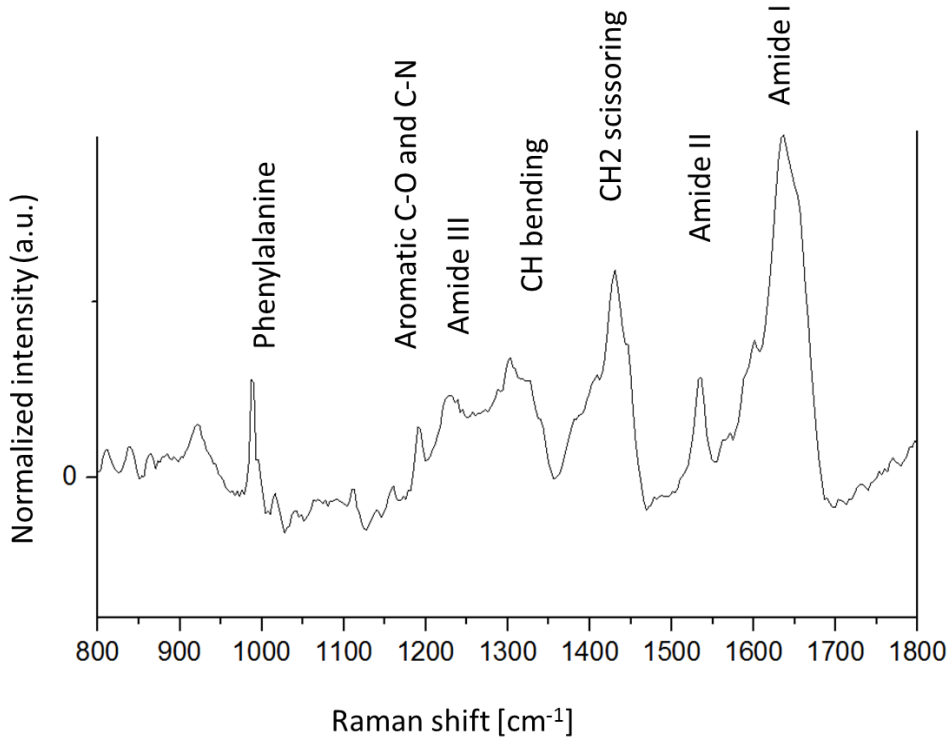


Figure 48 Raman-like spectrum of fibrin showing the fingerprint region. The amide I band (1570 to 1700 $cm^{-1}$) consists of several peaks that are asigned to secondary structural motifs.[56]

The amide I vibration corrsponds to the NH-coupled C=O vibration and because of local hydrogen bonding that stabalizes α-helices and β-sheets, the amide I vibrational resonance shape is distingt for each secondary structure. α-helices have a peak at 1640 $cm^{-1}$ and β-sheets at 1667 $cm^{-1}$. The amide II vibration is a weak band and the correlation between the secondary structure and frequency is more complicated than for the amide I vibration. The amide III vibration is correlated to the amide I vibration and can be only used to give complementary information. Therefore the amide I vibriation, as the strongest of all amide vibrations, is used to analyze the contend of secondary structure of fibrin samples under shear strain. [57, 71]

Many fibrin samples did not show a sufficient CARS signal when being imaged as a bulk material. To solve this problem, different methods of preparation and conditions were tested as depicted in figure 49.

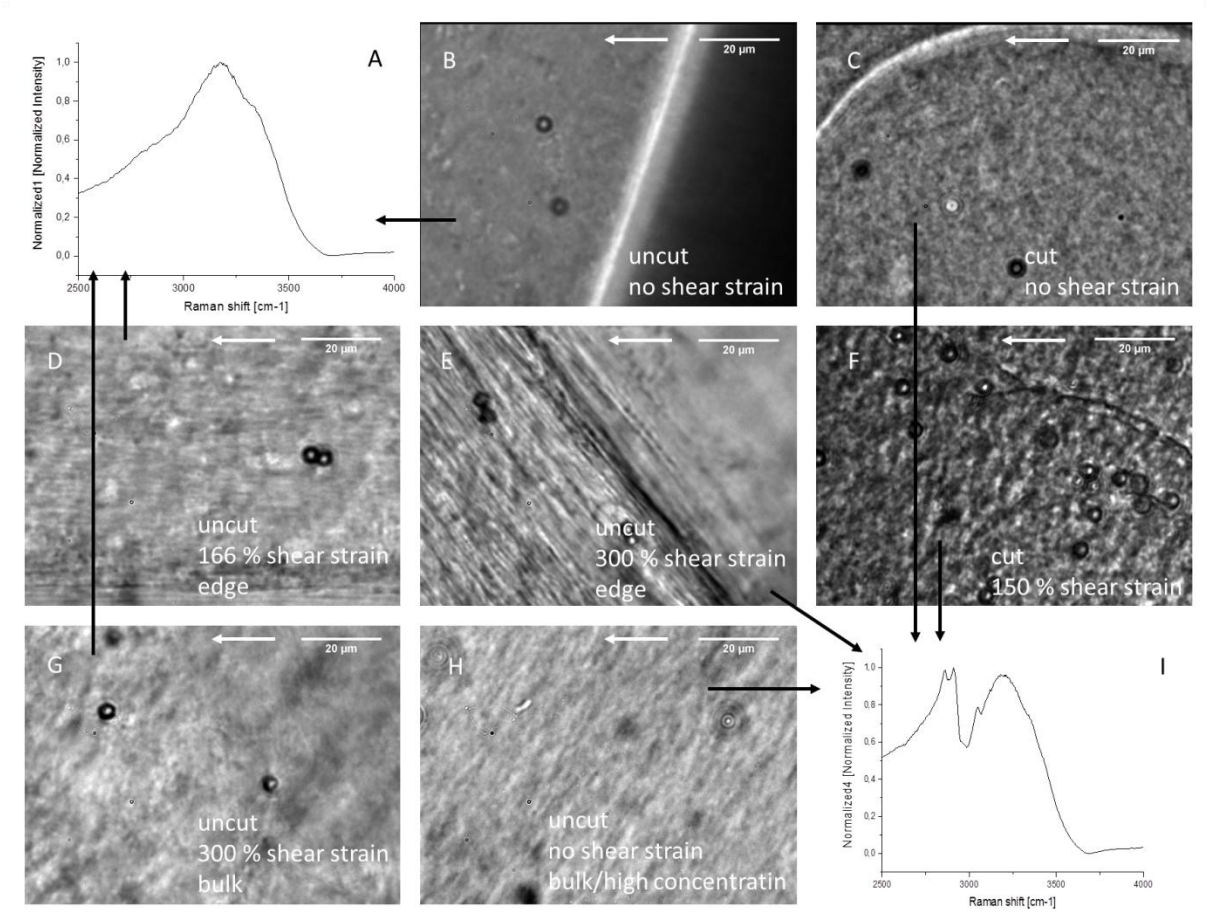


Figure 49 Representative raw CARS spectra from fibrin samples without (A) and with visible $CH_3$ vibrational band (I). Bright field microscopy images of fibrin samples of different preparation protocols containing styrene beads (B)-(H). The direction of shear strain is indicated by white arrows besides the scale bars of 20 µm.

The raw BCARS spectrum (A) does not show a $CH_3$ vibrational band at 2935 $cm^{-1}$ and only the vibrational band for water at 3100 $cm^{-1}$ is visible. The Raman-like spectrum of these samples has a too low signal-to-noise ratio in the fingerprint region for a meaningful analysis. Uncut samples with fibrinogen concentrations of 7.5 mg/mL without applied shear strains (B), under shear strains of 166 % (D), and in bulk for samples under 300 % (G) do not show a $CH_3$ peak. Only at the fringe of fibrin samples under large shear strains of 300 % (E) fiber alignment in the direction of applied shear strain is visible and a $CH_3$ peak appears in the raw BCARS spectrum (I). By increasing the concentration of fibrinogen to 18.75 mg/mL, a

sufficiently strong $CH_3$ signal can be found in some areas of the sample. These regions can be analyzed to determine the contribution of secondary structure in the protein.

Besides an increased fibrinogen concentration it was found that by cutting the fibrin samples into macroscopic pieces (see Appendix) a reliable CARS signal can be measured. Bright field images of cut samples show no microscopic visible disturbance when relaxed (C) and under shear strains (F).
The BCARS setup described in section 3.6 was used for all measurements. Different methods of preparation and conditions were specified for different fibrin samples. The spectra were analyzed in the amide I region to reveal the contribution of different secondary structures and the transition of α-helix into β-sheet under large shear strains.

## 5.1. BCARS measurements – Manual shear cell with flexure part

In this measurement the Fibrin sample was prepared according to section 3.2 with a final fibrinogen concentration of 7.5 mg/mL. The design for the shear cell as described in section 3.7.4. was used. The gel was cut with a scalpel and attached to chemically modified coverslips (section 3.7.2.). BCARS data sets for unloaded and for a shear strain of 180 % were measured covering a region of 20 µm x 20 µm (40 pixels x 40 pixels). The hyperspectral maps for the unloaded sample and for high strains were analyzed according to the amount of α-helix and β-sheet. The averaged spectra after filtering for polystyrene beads are plotted in figure 50.

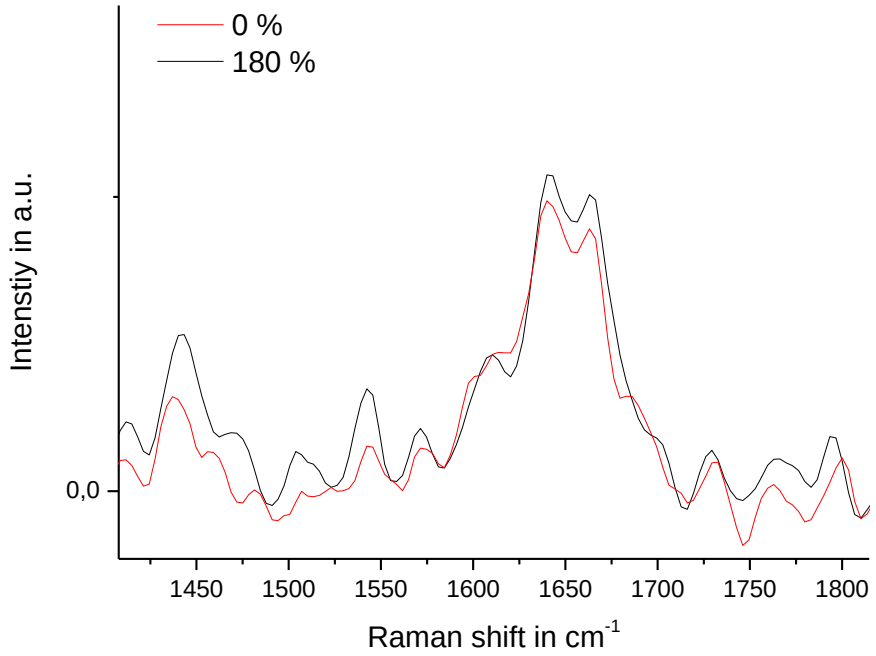


Figure 50 Averaged spectrum of a fibrin sample without strain (black) and under shear strain (red). Both spectra are the average from a 40 pixel x 40 pixel data.

The cutting of the fibrin sample leads to an appropriate BCARS signal. The red plot in figure 50 shows the averaged spectrum of a 40 pixel x 40 pixel data set for an unloaded sample. A high shear strain of 180 % was applied on the fibrin gel. The averaged spectrum of a 40 pixel x 40 pixel data does not show any visible shift in the amide l region (black). Therefore, mechanically induced secondary structural changes of fibrin gel under shear strain are not observable for the manual shear cell with flexure part up to 180 % shear strain.

## 5.2. BCARS measurements – Manual shear cell with flexure part and increased fibrinogen concentration

In this measurement the Fibrin sample was prepared according to section 3.2 with a final fibrinogen concentration of 18.75 mg/mL. The design for the shear cell described in section 3.7.4. was used. The gel was polymerized directly in the setup between the two coverslips and the use of chemically modified glass plates (section 3.7.2.) was not necessary. As analyzed in section 3.7.3., the direct polymerization

between the coverslips allows loading the sample to average strains of 293.33 ± 56.52 %.

Fibrin samples of low concentration (7.5 mg / mL) and without cutting of the sample did not show a sufficient CARS signal when being imaged as a bulk material. Using higher concentration of fibrinogen, in this case 18.75 mg/mL, resulted in a sufficient CARS signal in the fingerprint region, without cutting of the fibrin sample. The Raman-like spectrum plotted in figure 51 shows the amide I region with sufficient intensity to be analyzed.

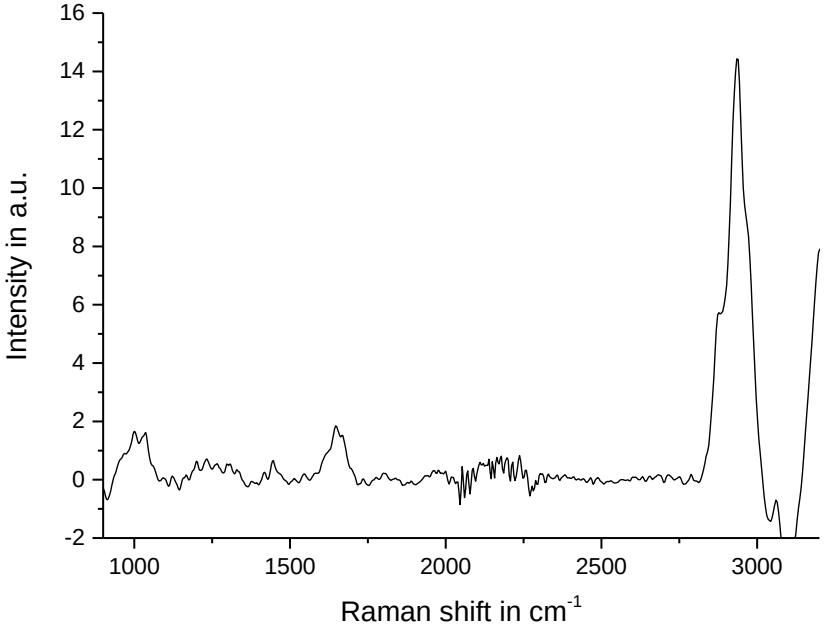


Figure 51 Raman-like spectrum of an uncut fibrin sample with high concentration of fibrinogen. The amide l region is of sufficient intensity for further analysis.

BCARS hyperspectral maps (40 pixels x 40 pixels) for unloaded and different shear strains were acquired. The CARS data for the unloaded sample and for the different strains were analyzed according to the amount of α-helix and β-sheet. The averaged spectra are plotted in figure 52.

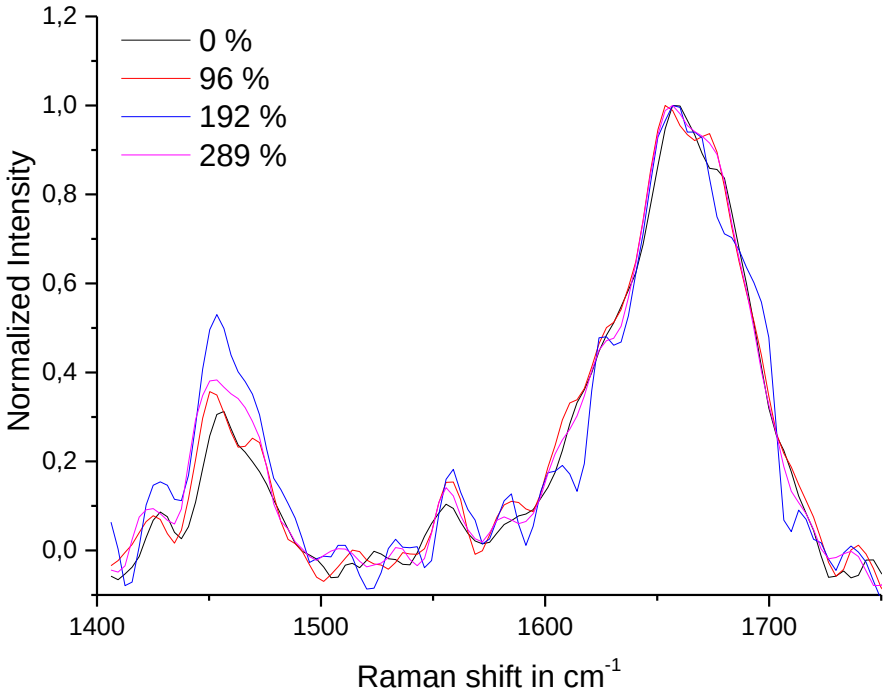


Figure 52 Raman spectra of uncut fibrin samples with high concentration of fibrinogen for different shear strains. The black blot shows the averaged spectrum of an unloaded fibrin sample. Arising shear strains of 96 % (red). 192 % (blue) and 289 % (pink) do not lead to a shift of the amide I region (1570 $cm^{-1}$ to 1700 $cm^{-1}$).

Applying large shear strains to the fibrin gel does not show any obvious change in the secondary structure. From 0 % to 289 % shear strain there is no visible shift of the amide I region observable.

Two separated sample areas of 20 x 20 µm were imaged for a shear strain of 289 %. The averaged spectra (see figure 53) were normalized to the $CH_3$-intensity and then analyzed per the amount of α-helix and β-sheet as defined by the peak intensity at 1650 $cm^{-1}$ and 1670 $cm^{-1}$.

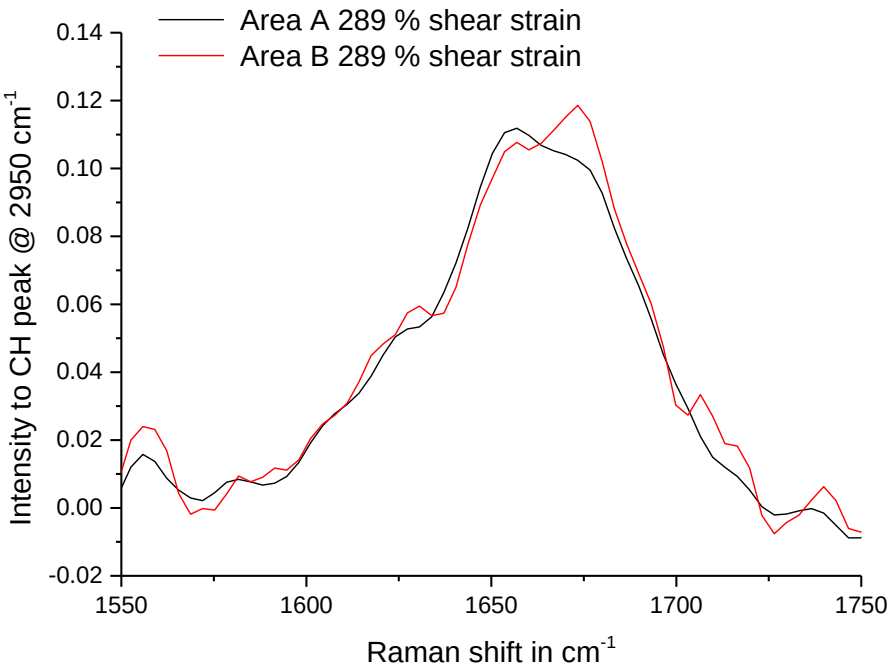


Figure 53 Averaged spectra of two areas in the same fibrin sample at 289 % shear strain. The black plot shows the average spectrum for area A without a shift in the amide I region while the red plot representing the average from a different area B is shifted towards higher wavenumbers.

Analyzing different positions within the same sample shows that for an area A, representing the same spectra for 289 % shear strain plotted in figure 53, does not show any shift in the amide I region, while the spectra measured in a different area B shows a minimal shift. The normalized intensity ratio of the β-sheet peak at 1675 $cm^{-1}$ to the α-helical part at 1650 $cm^{-1}$ changes from 0.997 for area A to 1.185 for Area B.

Polymerizing the fibrin sample directly in the shear cell setup made it possible to shear the sample to higher rates. A sufficient BCARS signal was obtained when the fibrinogen concentration was increased to a value almost ten times higher than physiological concentrations. The large shear strains of 289 % showed only a minor shift in the amide l band with reduced intensity from the α-helical part at 1650 $cm^{-1}$ and increased signal from the β-sheet peak at 1675 $cm^{-1}$. This indicates that to some degree a transition from α-helical to β-sheet secondary structure has occurred.

It was assumed that for high shear strains unfolding should take place to a much higher amount resulting in a more pronounced shift in the amide I band. However, experiments showed that fibrin spectra do not change sufficiently compared to relaxed samples. Therefore, the shear deformation did not change the secondary structure of the fibrin samples sufficiently. A possible explanation might be in the special design of the shear cell containing a flexure part holding the top coverslip and circumventing any normal force acting on the network when deformed. As depicted in the simplified scheme in figure 54 the top plate does not keep the gap size constant but allows sample contraction under shear.

The problem becomes clear when assuming fibrin fibers with the initial length of $l_{fib}\_A$ in a relaxed state between two glass plates with a gap size of $l_1$ as shown figure 54 (A). The shear strain applied by an offset Δx to the top coverslip with a *fixed* gap size (B) is stretching the fibrin fibers to the length. $l_{fib}\_B$, which is larger the initial length $l_{fib}\_A$. Applying the same offset Δx, but allowing top coverslip to move (C) leads to an decrease in the gap size (see section 3.7.5.) Therefore, the fiber length $l_{fib}\_C$ is smaller than the fiber length $l_{fib}\_B$ for fibers strained with fixed gap size.

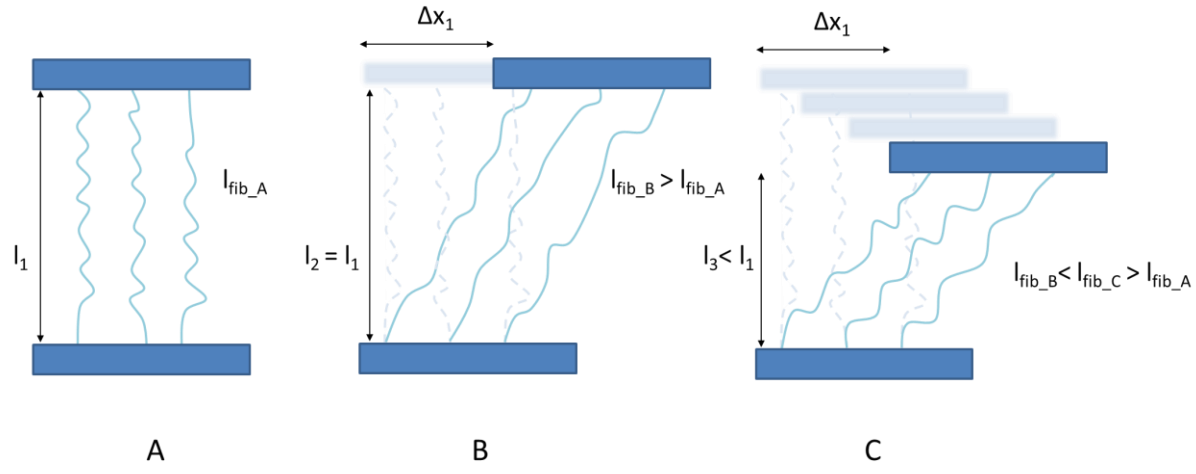


Figure 54 Schematic representation of unloaded fibrin fibers (A) with a theoretical fiber length $l_{fib}\_A$ and a gap size $l_1$. The offset $\Delta x_1$ leads to fiber stretching resulting in an increasing fiber length. With a fix gap size $l_2 = l_1$ (B) the stretched fibers do have a lager fiber length compared to the fibers in the setup with decreasing gap size (C) $l_3 < l_1$.

Using the correlation for the decreasing height during shear strain from section 3.7.5 shows that a shear strain of 100 % results in a gap size of only ~ 72 % of the initial height. Consider a lateral displacement (offset) of the 100 µm with fixed gap size of

100 µm, this results in a ~ 141 µm fiber length by the Pythagorean theorem (figure 54(B)). Compare this with the same lateral displacement having a flexible gap size, one only obtains 72 % of the fiber length (figure 54(C)). Even though this calculation only represents a simplified principle it suggests that the maximum offset of the coverslip applicable on a fibrin network before detachment is too low to stretch the fiber to a value when unfolding of α-helix into β-sheet occurs.

## 5.3. BCARS measurements – Manual shear cell with a fix gap size

To prevent the previous mentioned issue of changing gap size the top glass plate was kept at a fixed gap size for the following experiments. Fibrin samples were prepared according to section 3.2 with a final fibrinogen concentration of 7.5 mg/mL. The hydrogels were polymerized in the minimal loading mold (section 3.7.1.), cut with the help of a scalpel and attached to modified glass plates (section 3.7.2). The shear cell setup was mounted with a fixed height of 300 µm as set by two aluminum spacer (figure 14 and 15).

Next, BCARS data sets of unloaded and at high hear strain were acquired. The hyperspectral map for 500 % shear strain (the validly of this value will be discussed below) was analyzed according to the local amount of α-helix and β-sheet. All spectra were normalized to the $CH_3$-intenstiy at 2935 $cm^{-1}$. Representative spectra for a relaxed gel (blue), for a high an amount of α-helix (single pixel A) as well a high amount of β-sheet (single pixel B) are plotted in figure 55.

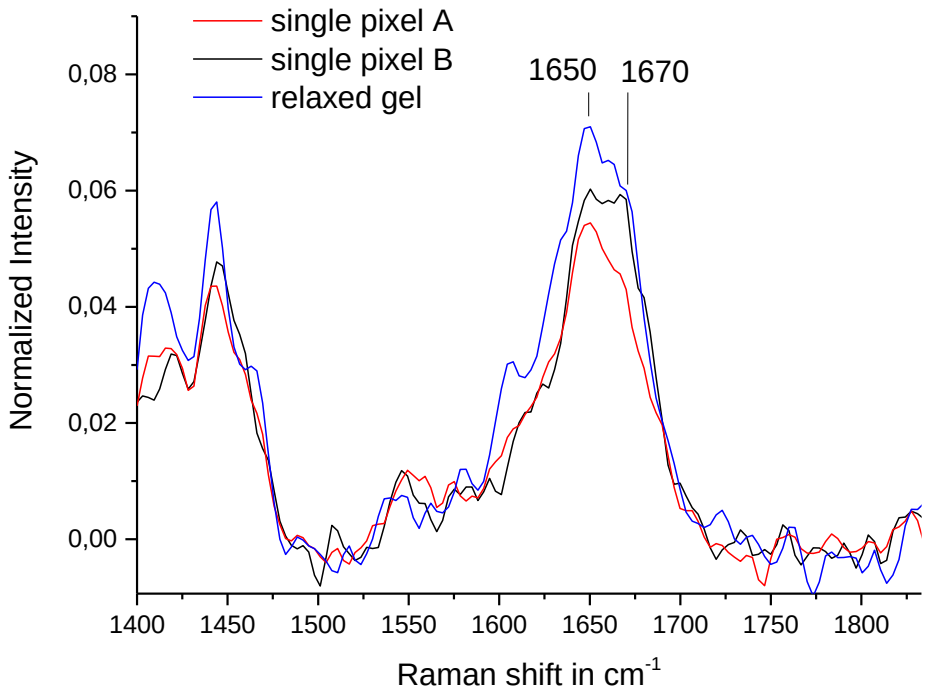


Figure 55 Raman spectra of a cut fibrin sample that was sheared to 500 % (in theory) with a fix gap size. The red plot is representing the amide I region of a single pixel A with no shift compared to a relaxed spectrum (blue) and the black blot is representing a single pixel spectrum B with a shift of the amide I region.

The spectrum from position A does not show any shift of the amide I region when compared to the spectrum of a relaxed gel. The ratio of the two peak intensities at 1670 $cm^{-1}$ and 1650 $cm^{-1}$ in spectrum A is 0.79, while the spectrum from position B shows a peak ratio of 0.97, indicating an increased amount of β-beta sheet structure relative to the α-helix structure.

The local ratio of β-sheet structure to α-helical structure for a fibrin gel under large shear strains is depicted in figure 56. The intensity of the amide I region at 1670 $cm^{-1}$ was divided by intensity of 1650 $cm^{-1}$. The unfolding from α-helical structure into β-sheet under large shear strains is clearly heterogeneously distributed within the sample.

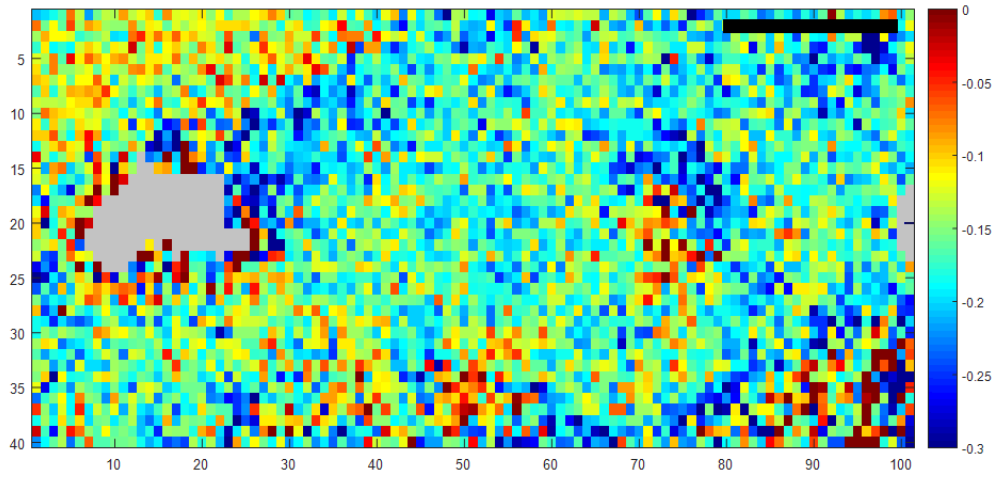


Figure 56 Spectral map showing the intensity ratio from β-sheet to α-helix secondary structure of fibrin under large shear strain. Polymerized under free conditions, cut and attached in a fixed geometry. Intensities at 1670 $cm^{-1}$ are divided by intensities at 1650 $cm^{-1}$. Red pixels are representing a high β-sheet amount while blue pixels indicate a predominant α-helical structure. The scale bar represents 10 µm and excluded pixels from polystyrene filtering are colored in gray.

A final offset of 1500 µm was set to the top coverslip. The shear strain resulting from this offset and the sample height of 300 µm leads to a theoretical shear strain of 500 %. Further investigations according to the maximum strain applicable to a fibrin gel attached to chemically modified glass plates (section 3.7.3) showed that strains of 500 % are not applicable as gels detach on average at 157.83 ± 38.26 %. Furthermore previous studies have shown that fibrin gels outlasts shear and tensile strains only up to 300 % prior to rupture.[7, 8] It is reasonable that the fibrin gel temporally detached from the cover slips during deforming, but since the complete coverslip was chemically modified the gel could immediately have react again with the coverslip. Likely the value of the actual applied shear strain is not 500 % but shear strains were stepwise applied, from attachment until detachment and again. The measurements of the maximum strain applicable to a fibrin gel attached to chemically modified glass of (section 3.7.3.) showed that the minimum strain before the gel detaches from the glass coverslips is 105 % while the maximum was found at shear strains of 193.33 %, therefore it is presumable that at least shear strains of 100 % were applied on the fibrin network.

In summary, it can be said that CARS measurements of fibrin hydrogels under shear strain require the cutting preparation of the sample. In addition, a sufficiently strong CARS signal could be acquired for gels of high fibrinogen concentrations as well as in samples under large shear strains. It has to be mentioned that not every fibrin sample with high concentration and not all samples under large shear strains gave reliable CARS signal. The benefit of using higher concentrations, next to getting any CARS signal at all, was that shear strains up to 293 % were applicable. Nevertheless, a transition of α-helix into β-sheet at a shear strain of 289 % was only observable in one area of a fibrin sample. So far, cutting the fibrin gel is the only way to guarantee reliable signal intensity to make analysis of the secondary structure possible. The area of the sample to be analyzed can be freely chosen. On the other hand attachment to the glass slides of these samples can only be done by a chemical reaction, which results in lower applicable shear strains. Using the cutting methodology (described in the appendix) and setup (see section 3.7.) did not show any shift in the amide l region at shear strains of 180 %. To increase the stretching of fibrin fibers within the range of shear strain that can be applied to post attached gels prior detachment, spacer have been used for a fix gap size.

# 6. Conclusion and Outlook

The acquired images from confocal microscopy of fluorescent labeled fibrin networks during deformation (section 4) indicate, that the contribution of the mechanics on the single fiber level differ, for shear and tensile deformations. The comparison of the FWHM, and therefore how parallel the fibers within a sample are aligned for shear and tensile deformations, shows that the FWHM for tensile strains is rapidly decreasing from 0 % strains to strains of only 5.6 %. This level of fiber alignment is reached in shear strains measurements at strains of around 83 % shear strain. The level of fiber alignment for 80 % tensile strain is comparable with the level of 208 % shear strain. The maximum peak amplitude shows that, next to the higher degree of alignment of fibers for tensile strain, the amount of fibers being affected by tension is more than for shear strains. While the maximum is reached for tensile strains of 61 % to 80 % the increasing trend for shear strains last for strains up to 208 %. Taken together, the determining of fiber orientation in strained fibrin gels by confocal microscopy demonstrate that while for tensile strain fiber orientation along the direction of load occurs already for small deformation a much larger shear strain is required for a similar network alignment.

It is known that the initial, linear network stiffness at low shear strains reflects thermal fluctuations of the fibers.[11] While it is predicted, that the elasticity at higher stress is dominated by changes at molecular level, the different nature of the fiber response to shear and tension leads to the anticipation of larger shear strains being necessary to unfold α-helical structures to β-sheets compared to tension.[16] This presumption is supported by the complete absence of α-helical unfolding into β-sheets at large strains of 180 % (section 5.1) and for some areas at around 300 % shear strains (section 5.2.). Since for some conditions like fibrin gels with high concentrations and under strains of ~300 % a minimal shift in the amide I region was determined (section 5.2), it could be possible that the force distribution was non-uniform. The measured hyperspectral map of 20 µm x 20 µm (section 5.1. and 5.2.) are big enough to represent the structure of an isotropic material. But it was already shown that the secondary structure becomes inhomogeneous with increasing tensile load, which indicates a non-uniform force distribution. [16] The

force-distribution of shear strains within the fibrin network seems to be even more non-uniform. Indication for that is the only partly unfolding of α-helical structure into β-sheet structure for high shear strains (section 5.3). The bright field microscopy pictures (figure 49) further show obvious fiber alignment for strains of 300 %, but since this was only observable on the fringe of the sample and not in the bulk material, it is reasonable that the force does not act uniform within the network. Confocal imaging of fibrin networks during deformation indicated that some areas experience more strain then others, representing by three out of four measurement sets that did not show any alignment at large strains (section 4.2.).

Nevertheless, molecular unfolding under high shear strains was proven (section 5.3.), the results of the confocal rheology of the fibrin fibers, and the results of confocal imaging of fibrin gels under tensile strain matches the investigation of the manifold higher shear strains be needed to unfold the fibrin fibers on the molecular level compared to tensile strains. While the first indications of molecular unfolding in shear have been seen, several pieces like the macroscopic distribution α-helical structures and β-sheets of fibrin sample under high shear strains and quantitative information about when molecular unfolding truly begins to dominate the mechanical response of fibrin under shear deformation, are still missing for a more satisfying understanding of the mechanical properties of fibrin networks with their large extensibility.

# 7. List of figures

# 8. References


1. Shah J., and Janmey P. "Strain hardening of fibrin gels and plasma clots." *Rheol. Acta.*, **36**, 262–268 (1997).

2. Wen Q., Basu A., Winer J. P., Yodh A. and Janmey P. "Local and global deformations in a strain-stiffening fibrin gel." *N. J. Phys.*, **9**, (2007).

3. Kang H., Wen Q., and MacKintosh F. C. "Nonlinear elasticity of stiff filament networks: strain stiffening, negative normal stress, and filament alignment in fibrin gels." *J. Phys. Chem. B.*,: **113**, 3799–3805 (2009).

4. Roberts W. W., Lorand L., and Mockros L. F. "Viscoelastic properties of fibrin clots." *Biorheology.*, **10**, 29–42 (1973).

5. Yao N., Larsen R. J., and Weitz D. "Probing nonlinear rheology with inertio-elastic oscillations." *J. Rheol. (N. Y. N. Y.).*, **52**, 1013–1025 (2008).

6. Janmey P., Amis E., and Ferry J. "Rheology of fibrin clots. VI.Stress relaxation, creep, and differential dynamic modulus of fine clots in large shearing deformations." *J. Rheol. (N. Y. N. Y.).*, **27**, 135–153 (1983).

7. Liu W., Jawerth L. M.,and Guthold M. "Fibrin fibers have extraordinary extensibility and elasticity." *Science.*, **313**, 634–638 (2006).

8. Brown A. E., Litvinov R. I., Weisel J. W. "Multiscale mechanics of fibrin polymer: gel stretching with protein unfolding and loss of water." *Science.*, **325**, 741–744 (2009).

9. Boulpaep E. L., and Boron W. F. *Medical Physiology.* Elsevier Saunders, 2nd edition, (2012).

10. Hvas A. M., Sørensen H. T., Norengaard L., Christiansen K., Ingerslev J., and Sørensen B. "Tranexamic acid combined with recombinant factor VIII increases clot resistance to accelerated fibrinolysis in severe hemophilia A." *Journal of Thrombosis and Haemostasis.*, **5**(12), 2408-2414, (2007).

11. Piechocka I. K., Bacabac R. G., Potters M., MacKintosh F. C., and Koenderink G. H. "Structural hierarchy governs fibrin gel mechanics." *Biophys. J.*, **98**, 2281–2289 (2010).

12. Hudson N. E., Houser J. R., Timothy O'Brien E., Taylor R. M., Superfine R., Lord S. T., and Falvo M. R. "Stiffening of individual fibrin fibers equitably distributes strain and strengthens networks." *Biophysical Journal.*, **98**(8), 1632-1640 (2010).

13. Liu W., Carlisle C. R., Sparks E. A., and Guthold M.. "The mechanical properties of single fibrin fibers." *Journal of thrombosis and haemostasis.*, **8**(5),1030-1036 (2010).

14. Terhune P. D., and Maker R.W. "Study of optical effects due to an induced polarization third order in the electric field strength." *Phys. Rev.*, **137**(3A), (1965).

15. Zumbusch A., Holtom G. R., and Xie X. S. "Three-dimensional vibrational imaging by coherent anti-stokes raman scattering." *Physical Review Letters.*, **82**(20), 4142-4145 (1999).

16. Fleissner F., Bonn M., and Parekh S. H. "Microscale spatial heterogeneity of protein structural transitions in fibrin matrices." *Biophysics.*, **2**(7), (2016).

17. Reinhard M. F. *Blood Coagulation Disorders Hemorrhagic Diatheses and Thromboembolic Diseases.* Berlin, Springer, (1987).

18. Litvinov R. I., Gorkun O. V., Owen S. F., Shuman H., and Weisel J. W. "Plenary paper Polymerizationof fbrin: specifcity, strength, and stability of knob-hole interactions studied at the single-molecule level." *Blood J.*, **106**(9), 2944-2951 (2005).

19. Mosesson M. W. "Fibrinogen and fibrin structure and functions." *J Thromb Haemost.,* **3,** 1894–1904 (2005).

20. Fowler W. E., Hantgan R. R., Hermans J., and Erickson H. P. "Structure of the fibrin protofibril." *Proc. Natl. Acad. Sci. U.S.A.*, **78**, 4872–4876 (1981).

21. Ryan E. A., Mockros L. F., Weisel J. W., and Lorand L.. "Structural origins of fibrin clot rheology." *Biophys. J.*, **77**, 2813–2826 (1999).

22. Pisano J. J., Finlayson J. S., Peyton M. P. "Cross-link in fibrin polymerized by factor 13: epsilon-(gamma-glutamyl)lysine." *Science.*, **160**(3830), 892–893 (1968).

23. Bagoly Z., Koncz Z., Hársfalvi J., and Muszbek L. "Factor XIII, clot structure, thrombosis." *Thrombosis Research.*, **129**(3), 382-387(2012).

24. Weisel J. W.,"The mechanical properties of fibrin for basic scientists and clinicians." *Biophys.*, **112**, 267–276 (2004).

25. Mosesson M. W., Siebenlist K. R., and Meh,. "The structure and biological features of fibrinogen." *Ann. N. Y. Acad. Sci.*, **936**, 11–30 (2001).

26. Guthold M. and Cho S. S.. "Fibrinogen unfolding mechanisms are not too much of a stretch." *Structure*, **19**(11), 1536-1538 (2011).

27. Broedersz C. P., Mao X., Lubensky T. C., and Mackintosh F. C.. "Criticality and isostaticity in fibre networks." *Nature Physics.*, **7,** 983-988 (2011).

28. Storm C., Pastore J. J., MacKintosh F. C., Lubensky T. C., and Janmey P. A. "Nonlinear elasticity in biological gels." *Nature.*, **435**(7039), 191-194 (2005).

29. Brown A.E., Litvinov R.I., Discher D.E., and Weisel J.W. "Forced unfolding of coiled-coils in fibrinogen by single-molecule AFM." *Biophys. J.*, **92** (2007).

30. Averett L. E., Geer C. B., and Fuierer R. R.," Complexity of "A–a" Knob–Hole Fibrin Interaction Revealed by Atomic Force Spectroscopy*" Langmuir*., **24**, 4979–4988 (2008).

31. Houser . J. R., Hudson N. E., Ping L., and O'Brien E. T., " Evidence that αC region is origin of low modulus, high extansability, and strain stiffening in fibrin fibers" *Biophys. J.*, **99**, 3038–3047 (2010).

32. Lim B. B. C., Lee E. H., Sotomayor M., and Schulten K.. "Molecular basis of fibrin clot elasticity." *Structure*, **16**, 449–459 (2008).

33. Litvinov R. I., Faizullin D. A., Zuev Y. F, and Weisel J. W. "The a-helix to b-sheet transition in stretched and compressed hydrated fibrin clots." *Biophys. J.*, **103**, 1020–1027 (2012).

34. Bramanti E., Benedetti E., Sagripanti A., and Papineschi F. "Determination of secondary structure of normal fibrin from human peripheral blood." *Biopolymers*, **41**, 545–553 (1997).

35. Kim O. V., Litvinov R. I., Weisel J. W., and Alber M. S. "Structural basis for the nonlinear mechanics of fibrin networks under compression." *Biomaterials*, **35**(25), 6739-3749 (2014).

36. Dutta S. K., Arevalo R. C., and Blair D. L. "Development of a confocal rheometer for soft and biological materials. " *The Review of scientiifc instruments*, **84**(6), (2013).

37. Boitte J.-B., Vizcaïno C., Benyahia L., Herry J.-M., Michon C., and Hayert M. "A novel rheo-optical device for studying complex fluids in a double shear plate geometry." *The Review of scientific instruments*, **84**(1), (2013).

38. Kim E., Kim O. V., Machlus K. R., Liu X, Kupaev T, Lioi J., Wolberg A. S., Chen D. Z., Rosen E. D., Xu Z., and Alber M. S. "Correlation between fibrin network structure and mechanical properties: an experimental and computational analysis." *Soft Matter*, **7**, 4983-4992 (2011).

39. Mermet-Guyennet M. R. B. et al. "Size-dependent reinforcement of composite rubbers" *Polymer*, **73,** 170-173 (2015).

40. Tadros T. F., *Rheology of Dispersions.* Weinheim, Wiley-VCH, (2010).

41. Goodwin J. W., and Hughes V, *Rheology for Chemists.* Royal Society of Chemistry, (2000).

42. Rosser R. W., Roberts W. W., and Ferry J. D. "Rheology of Fibrin Clots IV. Darcy Constants and Fiber Thickness ." **7**(2), 153-157 (1977).

43. E. Abbe, *Die Lehre von der Bildentstehung im Mikroskop.* Berlin: F. Vieweg und Sohn, (1910).

44. E. Hecht. *Optik.* Oldenbourg Verlag, 4. Auflage (2005).

45. Wang E., Babbey C. M., and Dunn K. W. "Performance comparison between the high-speed spinning disc confocal system and single-point scanning." *Journal of Microscopy*, **218**(2), 148-159 (2005).

46. Nelson M., Ledoux J., Taylor M., Bonev A., Hannah R., "Spinning Disk Confocal Microscopy of Calcium Signalling in Blood Vessel Walls." *Microsc Anal (Am Ed)*, **24**(2), 5-8 (2010).

47. Tsien R. Y., and Bacskai. *Handbook oc Biological Confocal Microscopy (ed. by J.B. Pawley),* New York; Plenum, (1995).

48. Ichihara A. et al. "High speed confocal fluoresence microscopy using a Nipkow scanner with microlenses dor 3-D imaging of single fluoresecent milecule in real time." *Bioimages*, **4**(2), 57-62 (1996).

49. Derrick M. R., Stulik D., and Landry. J. M. *Infrared Spectroscopy in Conservation Science,* The Getty Conservation Institute, (1999).

50. Hellerer T, *CARS-Mikroskopie: Entwicklung und Anwendung.* Dissertation; Ludwig-Maximilians-Universität München, Fakultät für Chemie und Pharmazie, (2004).

51. Schrader B. *Infrared and Spectroscopy, Methods and Applications.* Weinheim; Wiley-VCH, (1995).

52. Bright W. E. Jr., Decius J.C., and Cross McGraw-Hill P.C. *Molecular Vibrations.* Dover books on Chemistry, (1955).

53. Rago G., *Looking at life through molecular vibrations Biomedical applications of CARS spectro-microscopy.* Academisch Profschrift; Universiteit van Amsterdam, Faculteit der Natuurwetenschappen, Wiskunde en Informatica, (2012).

54. Bernath, P. F. *Spectra of Atoms and Molecules (2nd ed.),* Oxford University Press, (2005).

55. Hollas J. M., *Modern Spectroscopy (4th ed.).* John Wiley & Sons., (2004).

56. Talari A. C. S. , Movasaghi Z., Rehman S., and Rehman I. U. "Raman Spectroscopy of Biological Tissues." *Applied Spectroscopy Reviews*, **42**(5)**,** 493-541 (2014).

57. Duraipandian, S.,Zheng, W., Ng, J., Low, J. J. H., Ilancheran, A.” In vivo diagnosis of cervical precancer using Raman spectroscopy and genetic algorithm techniques“ *Analyst*, **136**, 4328–4336 (2011).

58. Teh, S. K.,Zheng, W., Ho, K. Y., Teh, M., Yeoh, K. G., Huang, Z. " Fiber-optic Raman spectroscopy probes gastric carcinogenesis in vivo at endoscopy" *J. Raman Spectrosc*. **40**, 908-914 (2009).

59. Huang, Z., McWilliams A , Lui H , McLean D. I , Lam S., and Zeng. "Near-infrared Raman spectroscopy for optical diagnosis of lung cancer" *H. Int. J. Cancer.* **107**, 1047-1052 (2003).

60. Davidson B, Murray AA, Elfick A, Spears N. "Raman Micro-Spectroscopy Can Be Used to Investigate the Developmental Stage of the Mouse Oocyte." *PLoS ONE*, **8**(7): e67972. doi:10.1371/journal.pone.0067972 (2013).

61. Day J.P.R, Domke K.F., G Rago, Kano H., Hamaguchi H., Vartiainen E.M., "Quantitative coherent anti-Stokes Raman scattering (CARS) microscopy." *The Journal of Physical Chemistry*,: **115**(24), 7713-7725 (2011).

62. Camp, C. H., Lee, Y. J., Heddleston, J. M., Hartshorn, C. M., … Cicerone, M. T. “High-Speed Coherent Raman Fingerprint Imaging of Biological Tissues”. *Nature Photonics*, **8**, 627–634 (2014).

63. Xu T., Vavylonis D., Tsai F. C,, Koenderink G. H. , Nie W., Yusuf E., "SOAX: A software for quantification of 3D biopolymer networks." *Scientific reports*, **5**, 9081 (2015).

64. Piechocka, I. K.. "Biopolymers: from structural hierarchy to nonlinear rheology." PhD thesis, VU-University (2013).

65. Boeckhoff, M. "The morphological response of a fibrin network to mechanical deformation." University of Amsterdam: Master Tesis (2016).

66. http://deben.co.uk/tensile-testing/optical/mini-tensile-tester-200n-compression-horizontal-bending-stage/

67. Janmey P. A., McCormick M. E., Rammensee S., Leight J. L., Georges P. C., and Fred C. “Negative normal stress in semiflexible biopolymer gels “ *Nature materials*, **6**(1), 48-51 (2007).

68. Mackintosh E. C., and Fred C. “Cross-Linked Networks of Stiff Filaments Exhibit Negative Normal Stress“ *Physical Review Letters*, **102**(8), (2009).

69. Maohong Y., Guowei M., Jianchun L. *Structural Plasticity.* Berlin, Heidelberg, New York, Springer, (2009).

70. Onck P. R., Koeman T., van Dillen T., and van der Giessen E. "Alternative Explanation of Stiffening in Cross-Linked Semiflexible Networks." *Physical review letter,* **95**(17), (2005).

71. Liu Y., Lee Y. J., and Cicerone M. T., "Broadband CARS spectral phase retrieval using a time-domain Kramers–Kronig transform." *Opt. Lett.,* **34**, 1363-1365 (2009).

72. Berjot, M., Marx, J. and Alix, A. J. P. "Determination of the secondary structure of proteins from the Raman amide I band: The reference intensity profiles method." *J. Raman Spectrosc.*, 18(4), 289–300 (1987) .

73. Guthold M. and Cho S. S. "Fibrinogen unfolding mechanisms are not too much of a stretch. Structure." *Structure*, **19** (11), 1615-1624 (2011).

# 9. Acknowledgement

First of all I would like to thank Prof. Mischa Bonn for the opportunity to write my Diploma thesis at the Molecular Spectroscopy department at the Max Planck Institute for Polymer Research in Mainz. I further want to thank my project leader Dr. Sapun Parekh for offering me this interesting and challenging topic as well as for all his advice and help.

Especially I want to thank Frederik Fleissner for all his amazing help. To describe all the different fields you supported me would double the size of this thesis. If I asked you hundreds of questions or needed your help almost at midnight, there was not even a single second during nine months were you lost patience. Without your comments on my presentations, data analysis, and on my thesis this work would never have been possible.

Further I want to kindly thank Prof. Gijsje Koenderink to offer me the possibility to do confocal rheology at the great FOM Institute AMOLF in the beautiful city Amsterdam. I also want to thank Bart Vos to introduce me to the confocal shear cell, helping me with confocal microscopy and giving me an introduction into Rheology.

I also want to thank Mischa Schwendy to help me with the confocal microscopy measurements at the Max-Planck Institute. For the shear cell design and the discussions according to it, I would like to thanks Marc-Jan van Zadel.

To all the awesome people at the Bonn department I want to give big thanks, hoping to be lucky enough to meet you all again one day. In particular I want to thanks the CARS group, you guys gave me the feeling of being welcomed since the day I joined the group, I truly appreciate that.

Finally I would like to thank my family, especially I want to thank my four amazing sisters for their never ending love, support and encouragement.

# 10. Appendix

Many fibrin samples did not show a detectable protein signal when imaged in the CARS microscope. Different methods of preparation and conditions to change the network structure (e.g. increasing fibrinogen concentration or changes in fiber diameter) could note solve this problem. However, previous work on fibrin under tensile deformation by Fleissner and coworkers showed that similar samples, when cut into stripes, resulted in strong CARS signals both in the fingerprint region and $CH_3$. [15] The $CH_3$-peak is typically the strongest vibrational band of a protein in a Raman spectrum. If the $CH_3$ vibration is undetectable, it is certain that the amide I region cannot be analyzed. Contrary to the sample preparation for BCARS tensile strain measurements, the fibrin samples used in shear strain measurements were initially Uncut and showed no detectable $CH_3$ resonance. Based on a number of trials, it appears that the crucial difference in sample preparation for both measurements is cutting of the fibrin gel (figure 57).

To demonstrate the influence of cutting the fibrin gel, hyperspectral maps of 5 µm x 5 µm (11 pixels x 11 pixels) of a sample in the original uncut state and of the sample cut to stripes with different width were acquired. The width of the stripes was estimated by taking photos of the sample together with a reference of known dimension and analyzing those via Image J.

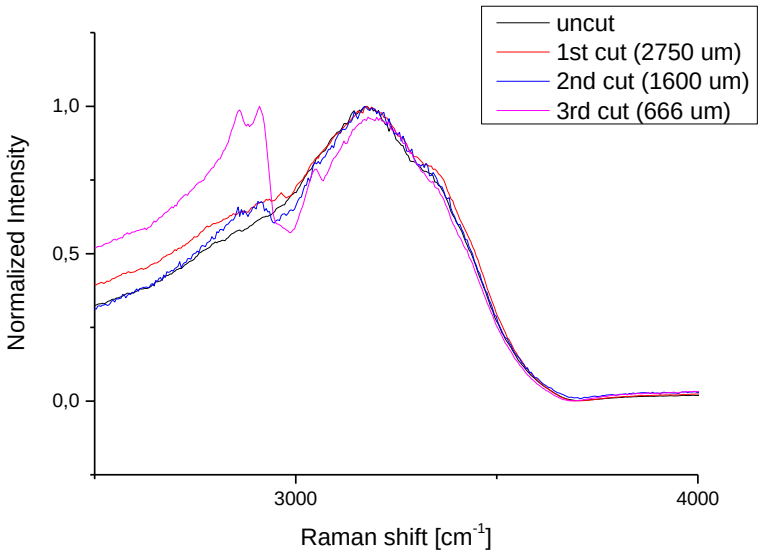


Figure 57 Normalized Raman spectra of fibrin showing the influence of cutting the gel to the increasing $CH_3$-Peak (2800-2950 $cm^{-1}$) of the protein. The spectrum of the uncut fibrin gel (black) does not show a $CH_3$-Peak and only the water peak (3100 $cm^{-1}$) is visible. Cutting the sample from both sides into a stripe with a width of 2750 µm (1st cut, red) is still showing no difference to the uncut sample while a 2nd cut of 1600 µm (blue) shows the appearance of a $CH_3$-Peak. Further cutting to a width of 666 µm (pink) shows an even more pronounced $CH_3$-Peak.

The change in intensity resulting by cutting the fibrin gel as shown in Figure 57 is quite strong, suggesting that cutting the gel leads to a potential density increase of the fibrin via stress relaxation.

To further investigate this effect, confocal microscopy was used to image the fibrin gel before and after cutting. Fluorescently labelled fibrin was prepared as described in 3.2 and images were acquired with a Zeiss LSM 510 microscope with laser excitation at 488 nm (Alexa488) and a 63x, 1.2 NA oil objective lens. The images were processed in ImageJ as described below. Confocal images of a representative example of a cut fibrin gel are shown in figure 58.

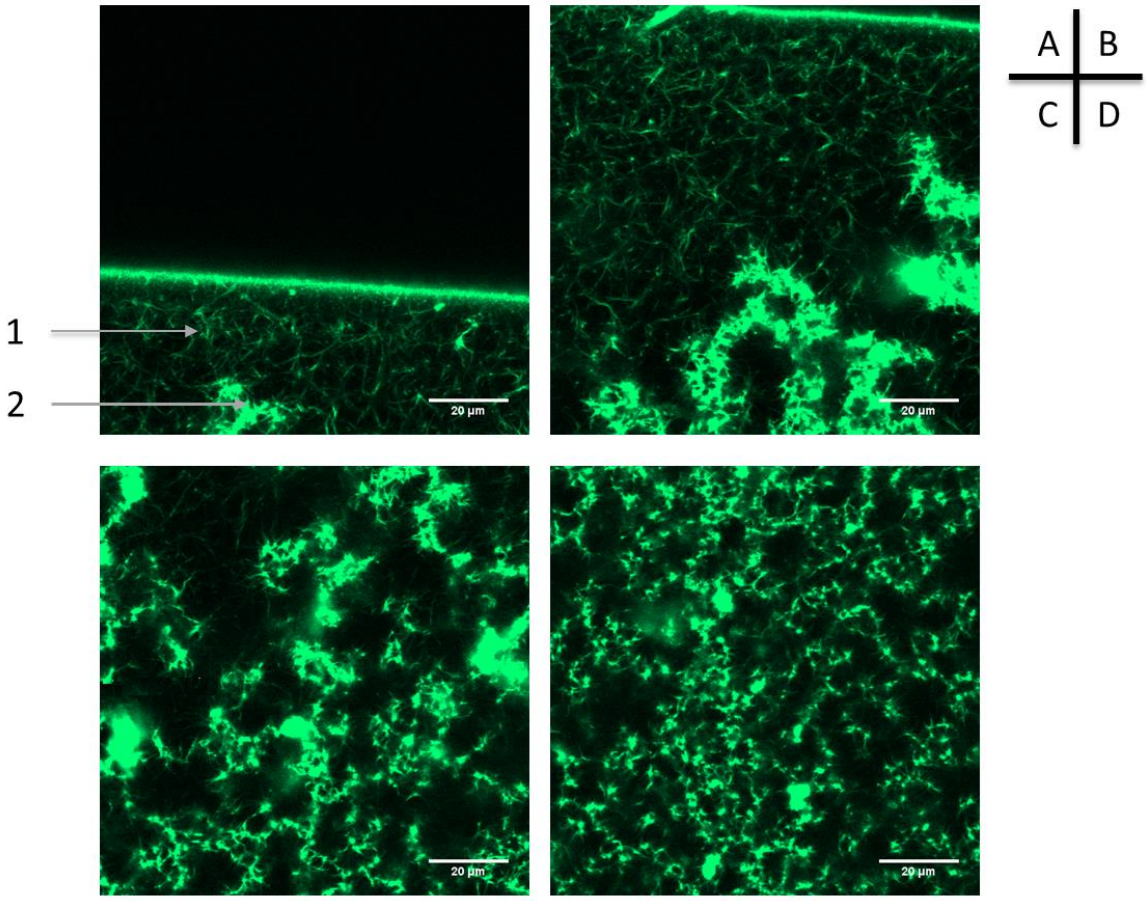


Figure 58 Confocal microscopy pictures of a cut fibrin sample. Pictures' showing the four slices of a z-stack with a step size of 50 µm, starting at (A) on the surface and ends 150 µm deeper in the bulk (D). Two different network structures are visible. Picture (A) showing the cutting edge and a homogeneous pattern (1) is present, as it can be found in uncut fibrin gels and aggregated network pattern (2). 50 µm deeper in the bulk (B) an aggregated network pattern (2) next to the original pattern (1) is visible. The images of the bulk 100 and 150 µm deeper (C,D) shows almost exclusively aggregated network pattern (2).

After cutting the fibrin gel, the homogeneous network architecture was changed to an inhomogeneous network of two distinct domains. The original fiber pattern is partially present in the cut fibrin gel but a second type of aggregated fibers appears. Figure 58 shows a z-stack with a step size of 50 µm of a cut fibrin gel. Figure 58 A shows the cutting edge as a bright ribbon of high fluorescence, indicating a high local density while the gel in some distance seems not to be affected. Homogeneous fiber pattern (1) is identifiable while a dense fibrin aggregation pattern is also seen (2). Figure 58 B, C, and D show images at deeper depths into the sample where more aggregated domains are seen in bulk of the gel.

Considering the strongly increased BCARS $CH_3$-peak and the obvious change in the network structure for cut fibrin gels, the aggregated network structure needs to be quantified in more detail, but that is beyond scope of this thesis. As two simple metrics to quantify the overall density of fibrin in the field-of-view, the porosity and the mean intensity of confocal images was analyzed in the two different patterns and an uncut fibrin reference sample. To ensure that the change in intensity is only related to the change in the network structure and not in the change of any other parameter, as for example photobleaching or detector sensitivity, the two types of network were analyzed within one z-stack. And three z-stacks at different positions of one sample have been used for analysis via the ImageJ plugin called DiameterJ.

Three different z-stacks at different positions of a cut fibrin sample showing, clearly both network structures, have been used as well as an uncut fibrin sample. Representative regions of interest (200 x 200 pixels corresponding to a field-of-view of 48.15 µm x 41.85 µm) of pattern (1) in the cut sample and of the uncut sample were analyzed according their porosity defined as the (Total number of black pixels) / (Total pixels in an image). For both samples, three regions have been analyzed in Diameter J. The averaged percent porosity $\overline{PP}$ for the homogeneous pattern (1) in an uncut fibrin sample was found as $\overline{PP}_{uncut} = 0.516 \pm 0.030$ and for the cut sample as $\overline{PP}_{cut} = 0.511 \pm 0.051$. The network porosity in pattern (1) in the cut sampleis therefore identical and the pattern can be assumed to represent the as-polymerized network state.

In addition to porosity, the mean fluorescence intensity of every z-stack for structure (1) and (2) was analyzed by Image J in three regions of interest (200 x 200 pixels corresponding to a field-of-view of 48.15 µm x 41.85 µm). The intensities of uncut fibrin were normalized to 100% and the averages intensities of the cut sample $\bar{I}_{cut}$ was measured as $\bar{I}_{cut} = 218.04\ \% \pm 5.33\ \%$. We note that the aggregated fibrin regions often saturated the confocal microscope detector due to the limited dynamic range, so this is a lower bound on the density increase.

The increase in fluorescence signal from 100 % to 218.04 % underlines the idea that the network intensity of the fibrin network is increasing thru the cutting process. This could possibly result in an increased $CH_3$-peak in the BCARS spectrum as seen in figure 57. However, several additional changes in microscopic properties such as presence of fibrin aggregates and propagation of the cutting effect into the bulk gel are still unclear, and they are necessary in order to fully understand how cutting modifies fibrin structure and morphology.